

Understanding the Mechanical Behaviors of Lithium-Based Battery Anodes

—Silicon and Lithium Metal

by

Xu Wang

A Dissertation Presented in Partial Fulfillment
of the Requirements for the Degree
Doctor of Philosophy

Approved February 2018 by the
Graduate Supervisory Committee:

Hanqing Jiang, Co-Chair
Hongbin Yu, Co-Chair
Candace Chan
Liping Wang
Qiong Nian

ARIZONA STATE UNIVERSITY

March 2018

ABSTRACT

This dissertation will investigate two of the most promising high-capacity anode materials for lithium-based batteries: silicon (Si) and metal lithium (Li). It will focus on studying the mechanical behaviors of the two materials during charge and discharge and understanding how these mechanical behaviors may affect their electrochemical performance.

In the first part, amorphous Si anode will be studied. Despite many existing studies on silicon (Si) anodes for lithium ion batteries (LIBs), many essential questions still exist on compound formation, composition, and properties. Here it is shown that some previously accepted findings do not truthfully reflect the actual lithiation mechanisms in realistic battery configurations. Furthermore the correlation between structure and mechanical properties in these materials has not been properly established. Here, a rigorous and thorough study is performed to comprehensively understand the electrochemical reaction mechanisms of amorphous-Si (a-Si) in a realistic LIB configuration. In-depth microstructural characterization was performed and correlations were established between Li-Si composition, volumetric expansion, and modulus/hardness. It is found that the lithiation process of a-Si in a real battery setup is a single-phase reaction rather than the accepted two-phase reaction obtained from in-situ TEM experiments. The findings in this dissertation establish a reference to quantitatively explain many key metrics for lithiated a-Si as anodes in real LIBs, and can be used to rationally design a-Si based high-performance LIBs guided by high-fidelity modeling and simulations.

In the second part, Li metal anode will be investigated. Problems related to dendrite growth on lithium metal anodes such as capacity loss and short circuit present major

barriers to the next-generation high-energy-density batteries. The development of successful mitigation strategies is impeded by the incomplete understanding of the Li dendrite growth mechanisms. Here the enabling role of plating residual stress in dendrite initiation through novel experiments of Li electrodeposition on soft substrates is confirmed, and the observations is explained with a stress-driven dendrite growth model. Dendrite growth is mitigated on such soft substrates through surface-wrinkling-induced stress relaxation in deposited Li film. It is demonstrated that this new dendrite mitigation mechanism can be utilized synergistically with other existing approaches in the form of three-dimensional (3D) soft scaffolds for Li plating, which achieves superior coulombic efficiency over conventional hard copper current collectors under large current density.

DEDICATION

To my Grandpa in heaven

and

Grandma

ACKNOWLEDGMENTS

I would like to express my deepest gratitude to my supervisor, Prof. Hanqing Jiang, who recruited me to his team five years ago when I was in a very low point of my life. He always has fantastic ideas and more importantly has a very brave heart to implement them, which has been constantly inspiring me in my research. Also, I guess I will never forget in my entire rest lifetime, many times watching him deriving piles of equations in a few seconds while I usually get lost after the first one or two lines in his office. It has been a truly enjoyable journey to be his student in the past five years.

I would also like to deeply thank my co-supervisor, Prof. Hongbin Yu, who has been so supportive to my research work and offered so many invaluable suggestions to my projects. It has also been a great pleasure to work with him and learn from him in the past few years.

I would also like to thank Prof. Candace Chan, Prof. Liping Wang and Prof. Qiong Nian for taking their precious time to serve on my committee and giving me important research advice.

I would like to thank my colleagues, Dr. Teng Ma, Dr. Cheng Lv, Dr. Zeming Song, Dr. Prithwish Chatterjee, Dr. Yonghao An, Dr. Wei Zeng, Wenwen Xu, Haokai Yang, Yiling Fan, Deepakshyam Krishnaraju, Jinshan Lin, Tianwei Sun, Binhe Liu, Todd Houghton, Dr. Sudhanshu Singh, Dr. Rui Tang, Dr. Mengbing Liang and professors, Prof. Hongyu Yu, Prof. Nikhilesh Chawla, Prof. Ming Tang, Prof. Huigao Duan, and ASU research professionals, David Wright, Tim Karcher and Jerry Eller.

Finally, I wish to thank my family. My grandparents who raised me up and gave me all their love, my uncle and aunts who bought me toys and showed me the world in old

days, and my brother and cousin who played with me and accompanied my entire childhood. Without them, I could not have grown up in such a warm environment and I could not have been so physically and mentally strong. At last, I want to thank my beautiful and foxy wife for drifting with me across the Pacific Ocean, and for always support me in my life. It's my biggest fortune to have you!

TABLE OF CONTENTS

	Page
LIST OF TABLES.....	vii
LIST OF FIGURES	viii
CHAPTER	
1 INTRODUCTION	1
2 QUANTIFYING ELECTROCHEMICAL REACTIONS OF AMORPHOUS SILICON-BASED LITHIUM-ION BATTERY.....	4
Introduction	4
Experiment	7
Results and Discussion.....	16
3 STRESS-DRIVEN LITHIUM DENDRITE GROWTH MECHANISM AND DENDRITE MITIGATION BY SOFT SUBSTRATES	31
Introduction	31
Experiment	33
Results and Discussion.....	38
4 CONCLUSIONS	66
5 FUTURE WORK	68
REFERENCES	69
APPENDIX	
A ABAQUS SUBROUTINE FOR SI THIN FILM LITHIATION MODELING	81
B COPYRIGHT AND CO-AUTHOR APPROVAL.....	104

LIST OF TABLES

Table	Page
1. Parameters Used in Simulation	16

LIST OF FIGURES

Figure	Page
1. Diffusion-induced Stress Fails Si During Cyclic Charge/Discharge.....	2
2. Li Dendrite Growth During Electrochemical Plating	3
3. Si Thin Film Electrode Fabrication and Characterization.....	9
4. SEM Images after Indentation images after indentation.....	12
5. Determination of Lithiation Mechanism of a-Si	18
6. Simulation Results of the Li Concentration for Different SOC's	21
7. AES, FIB and Nanoindentation Measurement.....	26
8. The Properties Variation of a-Si During Lithiation.....	30
9. Schematic Illustration of Cu Thin Film Wrinkling	33
10. Cell Design for Optical Observation	36
11. Fabrication of 3d Cu/PDMS Substrate	37
12. Optical Observation of Cu Current Collectors.....	40
13. Profilometer Observation of Cu Current Collectors	42
14. SEM Observation of Li Morphology	44
15. Stress-driven Li Whisker Growth Model	48
16. Cycling Experiments of Cu/PDMS and Cu.....	52
17. Characterization of 3D Cu@PDMS Substrates	55
18. Voltage Profiles and SEM Images of 3D Cu@PDMS Substrates.....	57
19. SEM Images of the Two Generation 3D Cu@PDMS Substrates	58
20. Cycling Test of the Second-generation 3D Cu@PDMS Substrate	59
21. Morphology of the Thin 3d Cu@PDMS and Cu Foil after 100 Cycles.....	61

Figure	Page
22. Thickness Changes of the Thin 3D Cu@PDMS Electrode upon Cycling	62
23. Projected Capacities of the 3D Cu@PDMS Electrode	65

CHAPTER 1

INTRODUCTION

Lithium-based batteries have been widely used in applications such as portable electronic devices and satellites because of their high energy density, no memory effect, reasonable life cycle, and one of the best energy-to-weight ratios¹. According to the charge storage mechanism, lithium-based batteries are classified into two types: lithium-ion (Li-ion) batteries that consist of intercalated Li compound as the cathode providing Li^+ in the electrochemical reaction and lithium (Li) batteries which use Li metal as the anode.

For conventional graphitic anode materials, the specific theoretical reversible capacity is 372 mAh g^{-1} based on a final composition of Li_xC_6 ($0 < x \leq 1$), which obviously limits the possibility of constructing a high-energy density battery system. Silicon (Si) is an attractive anode material being closely scrutinized for use in Li-ion batteries because of its very high theoretical charge capacity of $3,795 \text{ mAh g}^{-1}$. The development of Si-anode Li-ion batteries, however, has lagged behind because of the large volumetric change (380%) of Si-anodes upon insertion and extraction of Li (each Si atom can accommodate 3.75 Li atoms leading to the formation of $\text{Li}_{15}\text{Si}_4$ alloy), resulting in fracture (Fig. 1.1), pulverization and early capacity fading². In other words, this coupled mechanics (e.g., volumetric change) and electrochemistry problem is the bottleneck on the development of Si anode Li-ion batteries. To resolve this issue, many novel methods have been proposed. For example, thus far, it was evidenced that Si nanostructures such as three-dimensional porous Si particles³, Si nanocomposites⁴⁻⁸, nest-like Si nanospheres⁹, Si nanotubes¹⁰, Si core-shell nanowires¹¹⁻¹³ and amorphous or crystalline Si thin films¹⁴⁻¹⁹ on rough surfaces obtained via different synthesis routes, have shown improved electrochemical performance

and are considered to be excellent candidates for high performance electrode materials in Li-ion batteries than bulk Si. The nanostructured Si can provide the hosting sites for storing large amounts of Li-ions and a short diffusion distance (compared to bulk Si), which may bring about a high discharging rate (high-power density). Despite of the improved performance of Si anodes, the decay of the performance still presents when it comes to commercialize the aforementioned conceptions. Therefore, a fundamental understanding of this coupled behavior of mechanics and electrochemistry will not only advance our knowledge on the failure of Si under lithiation, but also provide a means to control or even optimize the electrochemical performance of Li-ion batteries from a unique way of mechanics.

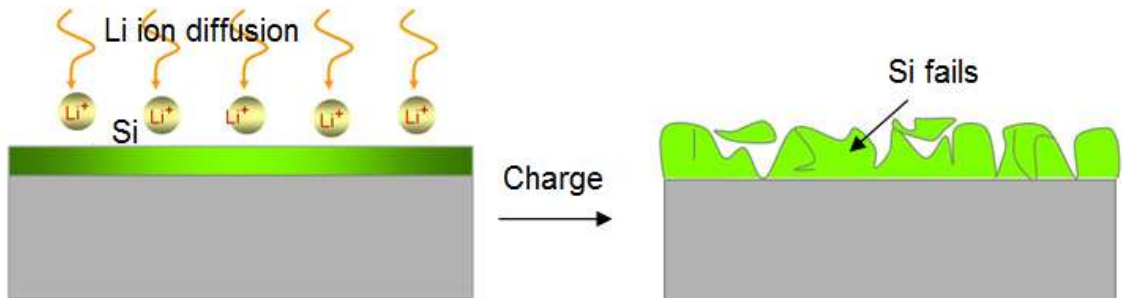


Fig. 1.1 Diffusion-induced stress fails Si during cyclic charge/discharge.

On the other hand, Li metal based batteries (Li-S, and lithium-air batteries) are also among the most promising electrochemical energy storage solutions to enable dramatic energy density increase and cost reduction over the currently dominant lithium-ion (Li-ion) battery technology. However, the long-standing issue of dendrite formation on Li metal electrode upon electrochemical cycling presents a major hurdle to the applications of Li metal-based batteries^{20,21} (Fig. 1.2). Needlelike Li crystals grow on the anode upon charge and discharge, become electrically isolated from the substrate due to non-uniform

dissolution rates at different sites of the dendrite. The direct victim of such Li loss is energy density, because excessive Li has to be used in the cell to make up for the loss. More seriously, a hazard could be caused by such “dead Li” crystal, which is electrochemically inactive but chemically hyper-reactive due to their high surface area. When dendrite growth pierces the separator and results in an internal short, thermal runaway and explosion occurs. Current research on resolving this critical problem mainly focuses on using new electrolytes and additives²²⁻²⁶ to form protective layer on Li surface, developing solid electrolytes^{27,28} to block dendrite growth, and employing 3D conducting scaffold with high surface area to reduce electroplating flux²⁹⁻³¹. While these efforts have resulted in appreciable progress, complete control of Li dendritic growth has not yet been achieved.

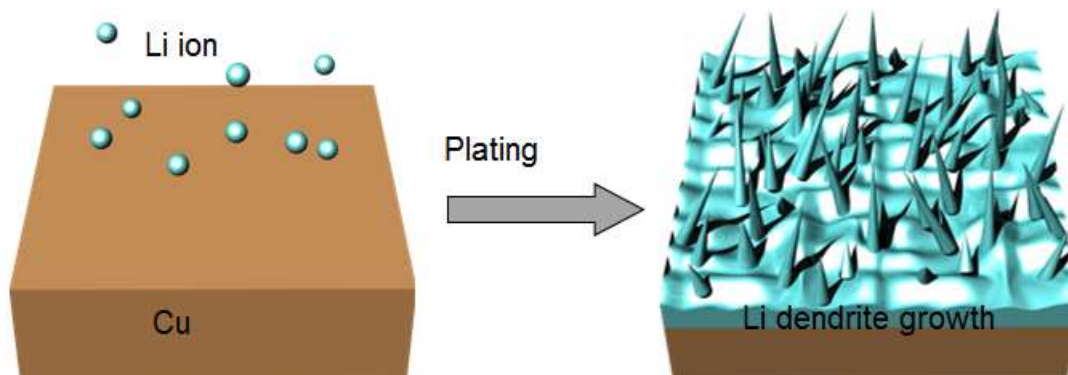


Fig. 1.2 Li dendrite growth during electrochemical plating.

CHAPTER 2

QUANTIFYING ELECTROCHEMICAL REACTIONS OF AMORPHOUS SILICON-BASED LITHIUM-ION BATTERY

Introduction

It is fortunate that many studies have been conducted to understand the material properties of lithiated silicon (Si), such as morphology, phase transformation, composition, volume expansion, and modulus, motivated by the highest known theoretical capacity of Si as a promising anode material for lithium-ion batteries (LIBs). Unfortunately, many fundamentally important issues have not yet been satisfactorily investigated. Some of the observations in the literature are contradictory and some approaches used are inaccurate or even incorrect. For example, based on in-situ transmission electron microscopy (TEM) experiments³²⁻³⁹, recent in-situ micro-Raman, in-situ X-ray diffraction (XRD) and in-situ X-ray reflectivity (XRR) experiments⁴⁰⁻⁴³, and some ex-situ characterizations (e.g., AES, XPS, SIMS)^{44,45}, one well-known finding is that the electrochemical process of crystalline Si (c-Si) is a two-phase transformation with a sharp interface between the amorphous Li-Si phase and the intact c-Si phase moving towards the remaining intact Si until it is completely consumed. The same conclusion of a two-phase reaction was made for nanoscale amorphous Si (a-Si), based on in-situ TEM observations^{46,47}. However, many early reports state that the reaction is a one-phase reaction^{48,49}.

Putting these controversies aside, one may note that many of the observations in the literature, to-date, are based on in-situ TEM experiments. In TEM observations, Si (either c-Si or a-Si) is charged by large potential bias that leads to large current density (up to 30 C in average) which is not feasible in a realistic conventional LIB configuration.

Therefore, the existing efforts of determining the lithiation process for Si may not fully uncover the mechanism for realistic conventional LIB configurations which usually use much smaller charging rates (e.g. C/3 and C/10).

The reported physical properties of lithiated Si also have some issues. High-energy capacity of Si is associated with high volumetric change. Based on atomistic simulations⁵⁰ or nanoscale electrochemical observations, such as using atomic force microscope (AFM) and in-operando neutron reflectometry^{48,51}, volumetric changes in the range of 375% or 400% have been widely reported and used in many theoretical modeling and simulations (for example⁵²⁻⁵⁷). However, the dependence of volumetric change on Li composition as Si is lithiated has not been satisfactorily explored because the composition of Li itself has not been thoroughly and quantitatively measured. One of the assumptions that is often made in determining the Li composition (i.e., Li_xSi where $x = 0$ for unlithiated Si) is to simply calculate the number of moles of Li as a counterpart of the electrons that have been pumped, based on applied current and time. In other words, the charging time was used to determine the Li fraction in a Li-Si alloy^{48,51}. This assumption is not valid for lithiated Si because of the formation of solid electrolyte interface (SEI) and parasite reactions that actually consume large amounts of Li. Another assumption is to use the cutoff voltages to determine the Li fractions^{58,59}. However, different cutoff voltages are only related to different Li fractions near the electrolyte/Li-Si interface. The potential inside the Li-Si alloy is in fact heavily dependent on the kinetics of the reaction⁶⁰.

It is important to note that the observed two-phase process from the in-situ TEM experiments does not support the above assumptions since in a two-phase reaction, a certain Li-Si ratio (e. g. $\text{Li}_{3.4}\text{Si}$) will always form first and then move toward unlithiated Si

until Si is consumed. That is to say, no matter what charging time or cutoff voltages are used, there will only be one Li-Si ratio for most of the charging period. Also, as pointed out by Li and Dahn in the Li-Si phase diagram obtained from the in-situ XRD c-Si experiment, during the initial lithiation, Si and Li_xSi form a “mixture” ($\text{Si} + \text{Li}_x\text{Si}$); while in the 2nd lithiation where c-Si has been amorphized, an individual x value in Li_xSi correlates to a specific capacity⁶¹. As the Li composition is a fundamental baseline of many related characterizations, its inaccuracy has influenced other measurements, such as modulus and hardness of lithiated Si. Limited comparisons between experiments (such as using curvature measurements⁶² and nanoindentation^{58,59,63,64}) and modeling (such as with density functional theory (DFT), ab initio, and molecular dynamics (MD) simulations⁶⁵⁻⁶⁷) have been conducted. The fact that the actual compositions have not been accurately measured hinders the relationship between structure and mechanical properties in these materials.

Because of the importance of the Si anode in LIBs and the lack of consensus on the precise metrics in this area, it is important to fundamentally understand phase transformation mechanisms and correlate these important quantities, such as Li-Si composition, volumetric expansion, moduli and hardness, with realistic conventional current density. Here a rigorous and thorough study is reported to identify the phase formation and Li-Si composition using auger electron spectroscopy (AES), volumetric expansion using focused ion beam (FIB), and the Young’s modulus and hardness by nanoindentation on the same lithiated a-Si thin films in different state of charges (SOCs). In order to fairly compare with the in-situ TEM experiments, 100 nm-thick a-Si thin film is used as the anode, which has the same dimension in the in-situ TEM experiments, to

identify the reaction mechanisms. Furthermore, explicit relationships between Li-Si composition, volumetric expansion, and modulus of lithiated a-Si is established. It is found that with standard charging rate of $C/3$, the lithiation of a-Si appears to be a single-phase process with no sharp phase interface, which is different from previously reported in-situ TEM observations. The direct measurement of Li composition provides more meaningful characterization on volumetric expansion and modulus. The present study resolves long-standing controversies and inaccuracies in the important area of Si anode and establishes databases for theoretical modeling and simulations, and thus references to rationally design Si anodes for high-performance LIBs.

Experiment

Si thin film anode preparation and Li-ion Battery assembly. For Si lithiation mechanism study, Chromium (10 nm), Copper (400 nm), Chromium (5 nm) and Silicon (100 nm) layers were deposited in sequence on the surface of Si wafer substrate using sputter PVD method. For lithiated Si expansion and nanoindentation study, Chromium (30 nm), Copper (800 nm), Chromium (30 nm) and Silicon (1 μm) layers were deposited in sequence on the Si wafer substrate using the same method (Fig. 2.1a). Because of the large thickness of Cu and Si, to ensure the quality of the films, the deposition of Cu and Si were carried out in multiple sessions. For Cu deposition, two sessions with 400 nm in each session were used. Three sessions were used for Si deposition with each session depositing 350 nm, 350 nm and 300 nm. The deposited Si was confirmed to be amorphous by Raman spectroscopy (Fig. 2.1b). Excluding the undesired area, the deposited Si film and Si wafer were covered with photoresist (AZ 4330) and then patterned by XeF_2 etching to expose the

Cu layer. Finally, the electrode was rinsed by acetone, methanol and isopropyl alcohol to remove the photoresist. The battery consisted of Si thin film as anode with Li metal (0.75 mm, Sigma-Aldrich) as reference and counter electrode in 1 M LiPF_6 in EC:DMC:DEC (1:1:1) (MTI Corp.) electrolyte. The two electrodes were laminated with an ion-permeable polymer (polypropylene Celgard 2500), which functioned as a separator. The electrodes, separator and electrolyte were sealed and vacuumed in an aluminized polyethylene (PE) pouch (Sigma-Aldrich). All assembly manipulations were performed in an argon-filled glovebox. For the lithiation mechanism experiment, only constant current of $C/3$ was used. For the expansion, modulus and hardness measurement experiment, the lithiation of Si thin film was performed using a lower constant current of $C/10$ rate until the potential reached a cutoff value, which was set to determine the approximate SOC, then switching to constant potential until the current dropped to 1-5% of $C/10$. In this dissertation, Si thin film was adopted as electrode to show the lithiation mechanism. One should note that in conventional battery, electrode is usually composed of active materials particles, binders and conductive carbon. A proper selection of elastic binder is very important for Si electrode because it not only provides binding force between particles but also confines the expansion and controls the stress during the expansion to avoid pulverization of Si.

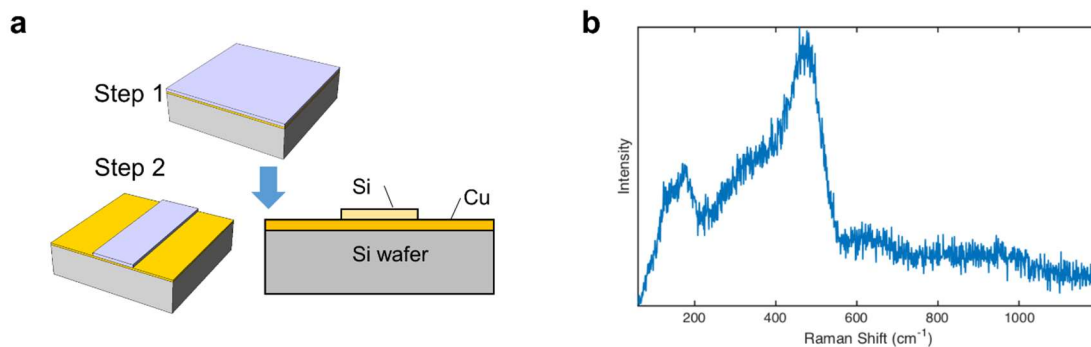


Fig. 2.1 Si thin film electrode fabrication and characterization. (a) Schematic illustration of the fabrication of Si thin film electrode. (b) Amorphous Si confirmed by Raman spectroscopy.

For AES, FIB and nanoindentation measurements, the lithiated Si electrode was taken out from the cell and immersed in an anhydrous dimethyl carbonate (DMC) filled vial for two hours to remove the solid electrolyte interface (SEI) layer on the surface of the electrode⁶⁸. After the removal of SEI, the electrode was cut into three pieces for AES, FIB and nanoindentation, respectively. All these procedures took place in the glovebox. During transfer of the samples, special care was taken to minimize the oxidation of the samples. The first piece was transferred to AES facility inside a sealed glass jar. For FIB operation, the second piece was first mounted on a SEM stub and then sealed inside a glass jar in the glove box. The third piece was mounted on a stainless steel disk, attached to the localized high-temperature stage, using a mounting adhesive (Crystalbond™, West Chester, PA) and then the whole assembly was transferred to the nanoindenter inside an aluminized polyethylene (PE) packaging bag.

Auger electron spectroscopy (AES) Li-Si composition measurements. The sample was mounted on the AES sample holder in glovebox and transferred to the chamber which was then vacuumed to a base pressure is 5×10^{-10} Torr. The pressure in the system during

the profile was 5×10^{-9} Torr. The primary electron beam energy was 3 keV and the beam current was 1 μ A. The energy regions for the desired elements were scanned and then ion etching was switched on for 2 minutes per cycle. The ion gun beam energy was 4 keV. Atomic concentration percentage was calculated by differentiating the data and measuring peak height vs baseline.

Measurements of Young's modulus and hardness of lithiated Si. Nanoindentation was performed using a commercial nanoindenter (Nanoindenter XP-II, Agilent) equipped with a localized high-temperature stage (also referred as hot stage). Although tests were performed at room temperature, the provision of continuous supply of argon gas with hot stage was required to prevent the oxidation of lithiated Si sample during nanoindentation. Before transferring the lithiated Si sample from glove box to the nanoindenter, the Berkovich tip was calibrated by measuring Young's modulus and hardness of a silica standard, using the same condition as used in the actual tests. Nanoindentation on lithiated Si was conducted in strain rate control with a strain rate target of 0.05 s^{-1} . At least 15 indentations were made on each sample and the maximum depth of indentation was maintained at 700 nm. To minimize the effect of thermal drift, the tests were conducted only when the thermal drift value was lower than 0.07 nm/s. A continuous stiffness measurement (CSM) technique was used during indentation, where a load is applied to the indenter tip to drive the indenter into the specimen surface while concurrently superimposing an oscillating force with a small amplitude (significantly smaller than the nominal load)⁶⁹. By using CSM technique, the hardness and modulus can be measured continuously with indentation depth which is useful to know substrate effect. Young's modulus and hardness for an individual indentation were measured as the average value

over a depth range where both modulus and hardness were independent of depth (plateau region). The contact stiffness (S) in CSM is calculated using the following equation:

$$S = \left[\frac{1}{\frac{F_0}{Z_0} \cos \phi - (K_s - m\omega^2)} - \frac{1}{K_f} \right]^{-1} \quad (2-1)$$

where F_0 is the force amplitude, Z_0 is the displacement amplitude, ω is the frequency of oscillation, ϕ is the phase angle between displacement and the force, K_f is the frame stiffness, K_s is the spring constant of leaf springs supporting the indenter, and m is the mass of the indenter. The values of the force amplitude, displacement amplitude, and the phase angle are continuously measured and allow calculating the contact stiffness. From the contact stiffness values, the reduced modulus E_r and the Young's modulus can be calculated using the following equations:

$$E_r = \frac{\sqrt{\pi}}{2\beta} \frac{S}{\sqrt{A}} \quad (2-2)$$

$$\frac{1}{E_r} = \frac{1-\nu^2}{E} + \frac{1-\nu_i^2}{E_i} \quad (2-3)$$

where E and ν are Young's modulus and Poisson's ratio of the material, and E_i and ν_i are that for the indenter; A is the contact area and β is the indenter geometry factor. Poisson's ratios for unlithiated Si and for lithiated Si were taken as 0.22⁵⁹ and 0.26, respectively. The first-principal calculations showed that Poisson ratio varies from 0.24 to 0.30 for lithiated silicon alloys⁶⁵. A Poisson ratio value of 0.26 which is an approximate average value of all those values is chosen. It should also be noted that there is not much impact of Poisson ratio since changing the Poisson ratio from 0.24 to 0.30 changes the modulus by only 3%.

Hardness (H) is given by the ratio of applied load to the area, i.e., $H = P/A$ and is independent of Poisson ratio. Fig. 2.2 show SEM images of sample after indentation.

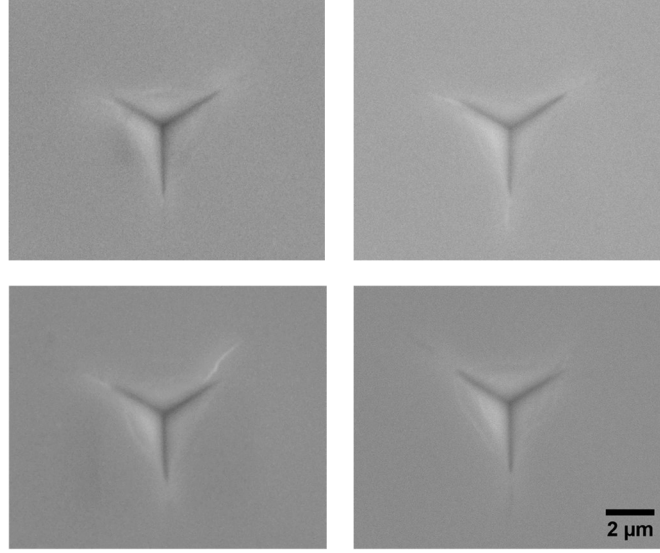


Fig. 2.2 SEM images after indentation

Simulation of a-Si thin film and sphere charged at extremely high rate (30C) and normal rate (C/3). The chemical potential per mole is given in a simple form as

$$\mu = RT \ln \frac{\bar{C}}{1-\bar{C}} \quad (2-4)$$

where \bar{C} is the normalized nominal Li concentration in Si which will be discussed in later paragraph, RT is the product of gas constant R and absolute temperature T . The kinetic law describing the mass flux of Li in to Si is also given in nominal quantities as

$$J_K = -\frac{CD}{RT} \frac{\partial \mu}{\partial X_K} \quad (2-5)$$

where C is the nominal Li concentration, D is the diffusivity of Li in Li-Si alloy.

The governing equation for the coupled large deformation and mass diffusion is the mass conservation law as

$$\frac{\partial C}{\partial t} + \frac{\partial J_K}{\partial X_K} = 0 \quad (2-6)$$

expressed in the reference coordinates X_K at time t .

A dimensionless formulation is used. The energy per mole is normalized by RT (unit: $J \cdot mole^{-1}$); mole density is normalized by C_{\max} (unit: $mole \cdot m^{-3}$); length is normalized by the characteristic height H for Si film, and characteristic radius R for Si sphere (unit: m); and time is normalized by H^2 / D . Dimensionless quantities are defined as follow: coordinates $\bar{X}_K = X_K / H$, $\bar{x}_j = x_j / H$ Li concentration $\bar{C} = C / C_{\max}$, time $\tau = Dt / H^2$, chemical potential $\bar{\mu} = \mu / RT$ and flux $\bar{J} = J (L / C_{\max} D)$.

Based on equations (1)-(2), the dimensionless nominal flux becomes

$$\bar{J}_K = - \left(\frac{1}{1 - \bar{C}} \right) \frac{\partial \bar{C}}{\partial \bar{X}_K} \quad (2-7)$$

and the dimensionless mass conservation law becomes

$$\frac{\partial \bar{C}}{\partial \tau} + \frac{\partial \bar{J}_K}{\partial \bar{X}_K} = 0. \quad (2-8)$$

The governing equation for heat transfer in ABAQUS is

$$\rho \frac{dU}{dT} \frac{\partial T}{\partial t} + \frac{\partial f_i}{\partial x_i} = r \quad (2-9)$$

where ρ is the density, U is the heat energy, T is the temperature, t is the time, f_i is the true heat flux and r is heat source. Rather than Eulerian description, it is an updated Lagrangian description which uses the converged coordinates from the last time step as the

new reference state. The mass conservation law in total Lagrangian description is expressed in current configuration as

$$\frac{1}{\det \mathbf{F}} \frac{\partial \bar{C}}{\partial \tau} + \frac{\partial}{\partial x_i} \left(\frac{F_{iK} \bar{J}_K}{\det \mathbf{F}} \right) = 0. \quad (2-10)$$

by comparing equation (6) for heat transfer and equation (7) for mass diffusion, an analogy between them can be established by the following equivalence,

$$\begin{aligned} \bar{C} &= T, \\ \tau &= t, \\ \frac{F_{iK} \bar{J}_K}{\det \mathbf{F}} &= f_i, \\ \frac{1}{\det \mathbf{F}} &= \rho \frac{dU}{dT}, \\ r &= 0. \end{aligned} \quad (2-11)$$

the deformation gradient \mathbf{F} is extracted from ABAQUS subroutine UMAT and the above process is implemented using UMATHT.

Finally, the thermal (compositional) expansion for large deformation is given by

$$\varepsilon^{(N)} = \frac{\beta (T^{(N)} - T^{(N-1)})}{1 + \beta T^{(N-1)}} \quad (2-12)$$

which is implemented using subroutine UEXPAN. And the deformation dependent flux for the current state is given by Nanson's formula

$$\bar{j} = \frac{\bar{J}}{\det \mathbf{F} \sqrt{(N_K F_{Ki}^{-1})(N_L F_{Li}^{-1})}} \quad (2-13)$$

which is implemented using DFLUX. A more detailed derivation and explanation can be found in reference^{53,55}.

To model the Si thin film, A thin pillar with the dimension of $25 \text{ nm} \times 25 \text{ nm} \times 100 \text{ nm}$ with x_1 - x_2 plane constrained was used to simulate 1D expansion of Si nano film. The principle stretch is only decided by the Li concentration change $\lambda_i(\bar{C}) = 1 + \beta\bar{C}$, where \bar{C} is the normalized nominal Li concentration in Si and β is the non-dimensional coefficient of compositional expansion. It must be point out here that even the linear dimensional change is assumed to be linearly dependent on Li concentration, which has been shown incorrect in this study (Fig. 2.6d), the constrained expansion (or 1D case) in the present simulation equates linear dimensional change to volumetric change. Thus this linear assumption is valid. The molar volume of Si is $\nu_{Si} = M_{Si} / \rho_{Si} = 1.2 \times 10^{-6} \text{ m}^3 \text{ mole}^{-1}$, where M_{Si} and ρ_{Si} are molar mass and density of Si. For the maximum lithiation product $\text{Li}_{3.75}\text{Si}$, the nominal Li concentration C_{\max} is $C_{\max} = 3.75 / \nu_{Si}$ and hence the normalized nominal Li concentration \bar{C} is $\bar{C} = C / C_{\max}$. β can be determined by the maximum volumetric change, which is equal to 282%. The diffusivity D of Li in Li-Si alloy varies from $1 \times 10^{-17} \text{ m}^2 \text{ s}^{-1}$ to $1 \times 10^{-16} \text{ m}^2 \text{ s}^{-1}$ with different Li concentrations⁴⁶. Here, a median D value of $5 \times 10^{-17} \text{ m}^2 \text{ s}^{-1}$ was chosen to represent its overall effect. The only variable in the simulation is nominal mass flux J . For charging rate of 30 C and C/3, fully charge a $25 \text{ nm} \times 25 \text{ nm} \times 100 \text{ nm}$ Si pillar to $\text{Li}_{3.75}\text{Si}$ takes a total time of $t_{\text{total}}^{30C} = 3600 / 30 = 120 \text{ s}$ and $t_{\text{total}}^{C3} = 3600 \times 3 = 10800 \text{ s}$. J is determined by $JAt_{\text{total}} = C_{\max}AH$, where A is the cross-sectional area of in the reference state and H is the height of the pillar. Hence, the nominal flux J_{30C} and J_{C3} for 30 C and C/3 are $J_{30C} = 2.59 \times 10^{-4} \text{ mole} \cdot \text{m}^{-2} \text{ s}^{-1}$ and $J_{C3} = 2.88 \times 10^{-6} \text{ mole} \cdot \text{m}^{-2} \text{ s}^{-1}$. The simulation was performed in ABAQUS via its user-

defined subroutines. Similar methods are adopted in the modeling of Si nanosphere. The parameters used in simulations are given in Table 2.1.

Table 2.1 Parameters used in simulation.

Parameters	Values
v_{Li} , molar volume of Li	$13 \times 10^{-6} m^3 mole^{-1}$
v_{Si} , molar volume of Si	$12 \times 10^{-6} m^3 mole^{-1}$
η , rate of change of elastic modulus	-0.1464
C_{max} , maximum nominal Li concentration	$0.3667 \times 10^6 mole \cdot m^{-3}$
R , gas constant	$8.314 J \cdot K^{-1} mole^{-1}$
T , room temperature	300 K
β , compositional expansion coefficient	0.5646
D , diffusivity of Li	$5 \times 10^{-17} m^2 s^{-1}$

Results and discussion

To characterize the composition evolution in the lithiation process, Auger electron spectroscopy (AES) was employed to obtain depth profiles of the composition of Li and Si in the Li-Si alloys. Unlike other widely employed surface analysis techniques such as X-ray photoelectron spectroscopy (XPS), which is relatively slow and has poor spatial resolution, and secondary ion mass spectrometry (SIMS), which is difficult for quantitative studies, when combined with argon sputtering gun, AES is very efficient in the quantitative depth profiling of metallic or semi-metallic alloy with high spatial resolution⁷⁰. The etching speed of the Auger system on the Li-Si sample was approximately 2.5 nm per cycle depending on the composition. Oxygen was detected to reflect the oxidation level during transfer of the sample from the glove box to the AES chamber. Cu was used to determine

if the AES depth profiling touches the current collector. If lithiation of Si is a two-phase process as observed in the *in-situ* TEM observations, one can expect a sharp dip in Li composition (Fig. 2.3a). On the contrary, a single-phase process suggests a relatively uniform Li concentration across the depth direction (Fig. 2.3a). Moreover, this assumption is valid even for lightly lithiated Si. Figs. 2.3b and 2.3c show the depth profiling of lithiated a-Si thin films under two cutoff voltages (0.2 V and 0.15 V) using AES. The cross-sections of the Si film under these two cutoff voltages were captured by focused ion beam (FIB) milling and are shown in Fig. 2.3d, along with the unlithiated a-Si for reference. It is observed that Si films expanded by 40% and 110%, respectively, as calculated from the images. From Figs. 2.3b and 2.3c, the sudden appearance of Cu marks the end of Li-Si alloy. In the region near Cu, there was an obvious increase in both Li and O. The higher O level is due to the surface oxidation of Cu after the deposited Cu was exposed to air. The increase of Li can be partially ascribed to Li aggregation near the Si/Cu interface which has been discussed before⁷¹. However, it's most likely due to signal interference by the appearance of Cu, because the Li peaks at 43 eV and 58 eV are close to the low energy Cu peaks at 58 eV and 60 eV. The observations in Figs. 2.3b and 2.3c show that even for high cutoff voltages, meaning lightly lithiated Si, Li appears throughout the lithiated Si and no sharp dips were found for both cases, which is consistent with the assumption of the single-phase reaction (Fig. 2.3a). Therefore, it is clear that lithiating a-Si is a single-phase process in realistic conventional current density, not a two-phase reaction as observed in *in-situ* TEM. This is consistent with the indirect experiment about the lithiation of a-Si (not via *in-situ* TEM)^{48,49}, in which the appearance of a continuous change of voltage profile is believed to be the evidence of a single-phase reaction⁷².

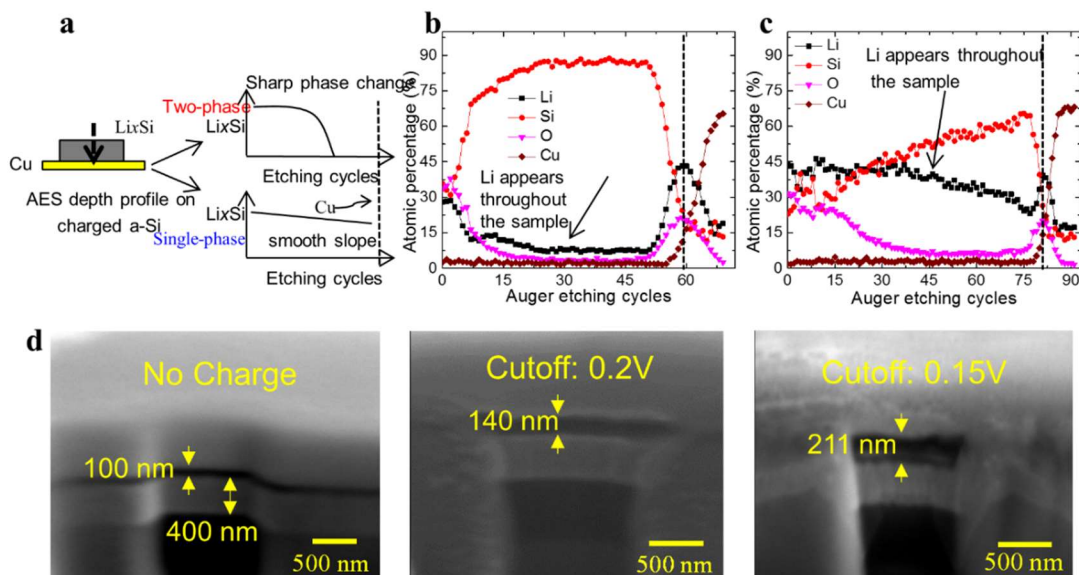


Fig. 2.3 Determination of lithiation mechanism of a-Si. (a) Schematic explanation of single-phase and two-phase lithiation processes. (b)-(c) The Li, Si, O and Cu concentration profiles using 0.2 V and 0.15 V cutoff voltage, obtained by auger electron spectroscopy (AES). Here the relatively high cutoff voltage provides slightly lithiated a-Si. Li's appearance throughout the sample shows the single-phase reaction mechanism. (d) The scanning electron microscope (SEM) images showing the cross-sectional view of un lithiated a-Si, lithiated a-Si with 0.2 V and 0.15 V cutoff voltages. The expansions are 40% and 110%, respectively.

The following explanation is offered. In the TEM setup, there is no conventional electrolyte or separator and Si is charged by direct contact of Li to Si using either an ionic liquid or solid Li oxide (Li_2O) electrolyte as a separation. Moreover, the high potential bias between the two electrodes will induce extremely large current density up to 30 C in average on Si anode. In the conventional battery configuration, the charging rate is usually no greater than 1 C due to the limitation of Li diffusivity in electrolyte and the permeability of separator⁷³⁻⁷⁵. Therefore, the appearance of a sharp interface can be simply ascribed to the large current density that is feasible due to the high diffusion rate of Li atoms through ultrathin ionic liquid or Li_2O and thus pumps Li atoms into Si anode at a high rate. However, the high-rate pumping is restrained by the limited diffusivity of Li in Si anode. Thus,

interface and interface movement appears. Under conventional charging rate ($C/3$, for example), Li atoms have sufficient time to diffuse and react with the Si anode. Therefore, the lithiation process in the conventional charging rate is a single-phase process. Also, the conventional definition of “phase” in materials science is followed, and two systems belong to the same phase if they share the same type of structure with given crystal symmetry. For our system, Li_xSi alloy distributes thorough out the electrode with varied Li concentration, but structure-wise it has the similar disordered structure. Therefore it is proper to regard the whole electrode as in a single phase. This is in clear contrast to the two-phase reaction mechanism of lithiation of a-Si, in which the electrode can be separated into two regions with lithiated and unlithiated Si.

Continuum simulations have been conducted to study the effect of charging rate using the finite element package ABAQUS and its user defined subroutines to couple large deformation and diffusion. The Si thin film is modeled as a Si pillar with lateral (x_1, x_2) directions constrained and x_3 as the only meaningful spatial coordinate. Fig. 2.4a shows the evolution of the normalized Li concentration (considering $\text{Li}_{3.75}\text{Si}$ as the fully charged state) for different SOC's at the charging rates of 30 C and $C/3$. It is clearly observed that there is an interface and interface movement between the high and low Li containing domains for 30 C charging rate; while Li concentration is very uniform under $C/3$ charging rate. From the normalized Li concentration in the thickness direction for different SOC's at charging rates of 30 C and $C/3$, and shows a rapid change in Li concentration for high charge rate (30C) but not for low charge rate ($C/3$). A similar phenomenon occurs in a-Si nanoscale sphere with a radius of 100 nm (Fig. 2.4b). One should note that if other aspects (e.g., stress and chemical reaction) are considered in the modeling, a relatively uniform but

sloping profile rather than a perfectly uniform profile would be observed at low charge rate; and a much sharper profile would present at higher charge rate. Without considering these aspects, it won't qualitatively change the conclusion though. More complicated models that couple finite deformation kinematics, stress-diffusion interaction and chemical reaction also point out that for a given ratio between the rate of interfacial reaction and that of Li diffusion in Si, a higher charging rate is likely to cause a two-phase process, while lower rates may result in continuous phase lithiation^{54,76}, which in our case is in fact called single-phase lithiation.

Identifying the reaction mechanism being a single-phase process in the conventional charging rate is extremely important as it provides a rational to characterize Li composition in Li-Si alloy throughout the depth direction. Otherwise it will be just one composition for lithiated Si if it is a two-phase reaction. By applying different SOC's (i.e., charging with small constant current (CC) and followed by constant voltage charge (CV) using different cutoff voltages), various compositions can be just achieved. To establish explicit relationships between Li-Si composition, volumetric expansion, and modulus and hardness, the charged Si samples were cut into three pieces to measure the composition, expansion, modulus and hardness in parallel using different tools. For accurate measurement of modulus and hardness, a much thicker ($\sim 1\ \mu\text{m}$) a-Si was sputtered on 800 nm-thick Cu on a Si wafer substrate. AES was again employed to quantify the composition of Li and Si in Li-Si alloy. In addition to Li and Si, C and O were chosen during depth profiling to characterize SEI residue and oxidation in the sample. FIB was used concurrently to measure the volumetric expansion and nanoindentation was used for modulus and hardness measurement.

Fig. 2.5 shows the results of AES for composition, FIB for volumetric expansion, nanoindentation for modulus and hardness, using unlithiated a-Si as a reference and lithiated a-Si with different cutoff voltages (e.g., from 0.25 V to 0.01 V). Each panel shows the parallel measurements for the same sample with identical SOC. Fig. 2.5a is for unlithiated a-Si where the AES result clearly and neatly shows a vanishing presence of Li, C, and O and the dominating presence of Si. FIB cross-sectional view shows the thickness of unlithiated Si (930 nm) along with other layers. The nanoindentation results show that for the uncharged sample, modulus and hardness were observed to be constant between about 60-100 nm down the surface, and therefore the Young's modulus and hardness values were taken as the average value in this range (i.e., the regions between dashed lines in Fig. 2.5a). Young's modulus and hardness of the uncharged sample was measure to be 124 GPa and 10.6 GPa, respectively. At very low depth, the values were affected by the roughness and surface oxides. At higher depth, the gradual increase in modulus and decrease in hardness values are due to the presence of Cu and Si wafer as substrates. The Young's modulus and hardness of Si wafer were measured to be 175 GPa and 12.3 GPa, respectively. The measured Young's modulus and hardness of Cu layer were 108-135 GPa⁷⁷, and 3-3.5 GPa⁷⁸, respectively. During indentation, since the size of the elastic zone beneath the indenter tip is much larger than that of the plastic zone, the effect of substrate on the Young's modulus is larger than that on hardness⁷⁹. The gradual increase in modulus values is due to the penetration of elastic zone into the Si wafer, which has a higher modulus than the unlithiated Si. The decrease of the hardness curve with depth might be attributed to the smaller plastic zone size which has not yet reached to the Si wafer but has penetrated Cu, which has a much lower hardness.

For lithiated a-Si using high cutoff voltage (0.25 V), the AES results in Fig. 2.5b shows that apparently, C and O were only observed from 0 nm to approximate 50 nm (or equivalently 17 AES etching cycles assuming 2.5-nm etching depth per cycle), from the surface and their atomic percentages dropped to less than 5% quickly after 40 nm, which shows that SEI and oxidation were successfully controlled. The atomic fractions of Li and Si varied from 0 nm to 70 nm from the surface and became fairly stable after 70 nm (i.e., approximately 35 AES etching cycles) which indicates the formation of a stable Li-Si alloy. The composition of Li-Si was then extracted from the stable region as $\text{Li}_{0.23}\text{Si}_{0.71}$. From the FIB measurement, a-Si expands from the original 930 nm (Fig. 2.5a) to 1.25 μm . Because of the thin film geometry of a-Si, the lateral dimension is much larger than the thickness dimension and the a-Si film is constrained laterally by the substrate. Thus the thickness expansion is considered as the volumetric expansion and the expansion in lateral direction is neglected. 34% volumetric expansion is observed here. The nanoindentation results show that modulus and hardness values for the $\text{Li}_{0.23}\text{Si}_{0.71}$ alloy have decreased to 73 GPa and 2.4 GPa, respectively. The Young's modulus curve gradually increases with depth of indentation because of the same argument of the penetration of elastic zone into the Si wafer. The hardness curves show more interesting behaviors. For the pristine Si sample, the hardness decreases with increased indentation depth because of the substrate effect of Cu that has lower hardness than Si. For the slightly charged sample (Figure 2.5b), the increase trend of hardness curve is also due to the substrate effect of Cu that has higher hardness than the lithiated Si. Also, with further lithiation, hardness curves show less increase trend because as Si becomes much thicker, the influence of Cu becomes less significant (Figs. 2.5c-f).

Figs. 2.5c-f show the results for cutoff voltages of 0.15 V, 0.1 V, 0.05 V, and 0.01 V. Here, fully lithiated a-Si is achieved for the 0.01 V cutoff voltage is considered here. Similar trends as that in Fig. 2.5a have been repeatedly observed. The composition ratios were extracted from the stable regime of the AES curves. The fraction of Li gradually increases and Li-Si compositions evolve from $\text{Li}_{0.34}\text{Si}_{0.58}$, $\text{Li}_{0.46}\text{Si}_{0.42}$, $\text{Li}_{0.49}\text{Si}_{0.34}$, to $\text{Li}_{0.55}\text{Si}_{0.33}$. The gradual increase of Li fractions is another piece of evidence that the lithiation of a-Si in conventional LIB configuration is a single-phase process. The volumetric expansion increases from 85%, 159%, 230%, to 282%. The maximum volumetric expansion 282% when Si is fully lithiated verifies previous results that Si expands about 280%^{39,47,48,51}, which in return show that a-Si has been fully charged under 0.01 V cutoff voltage. The modulus and hardness continue decreasing. For example, the Young's modulus and hardness of fully lithiated a-Si drop to 46 GPa, and 1.71 GPa, respectively. The curves for fully lithiated sample also show the same trend: the Young's moduli gradually increase with depth of indentation because of the effect of Si substrates. The hardness curves remain almost constant, which might be attributed to the dramatic increase in volume due to lithiation. For example, the thickness of fully lithiated a-Si was about 3.56 μm and it may be argued that the plastic zone remained inside this thick film. The modulus and hardness values for fully charged sample were taken from 100-200 nm and 150-250 nm depth, respectively. Similarly, for other cutoff voltages, the modulus and hardness of the lithiated a-Si films were averaged in the depth range where the curves exhibited a plateau, i.e., the results in this range have a negligible influence of the substrate.

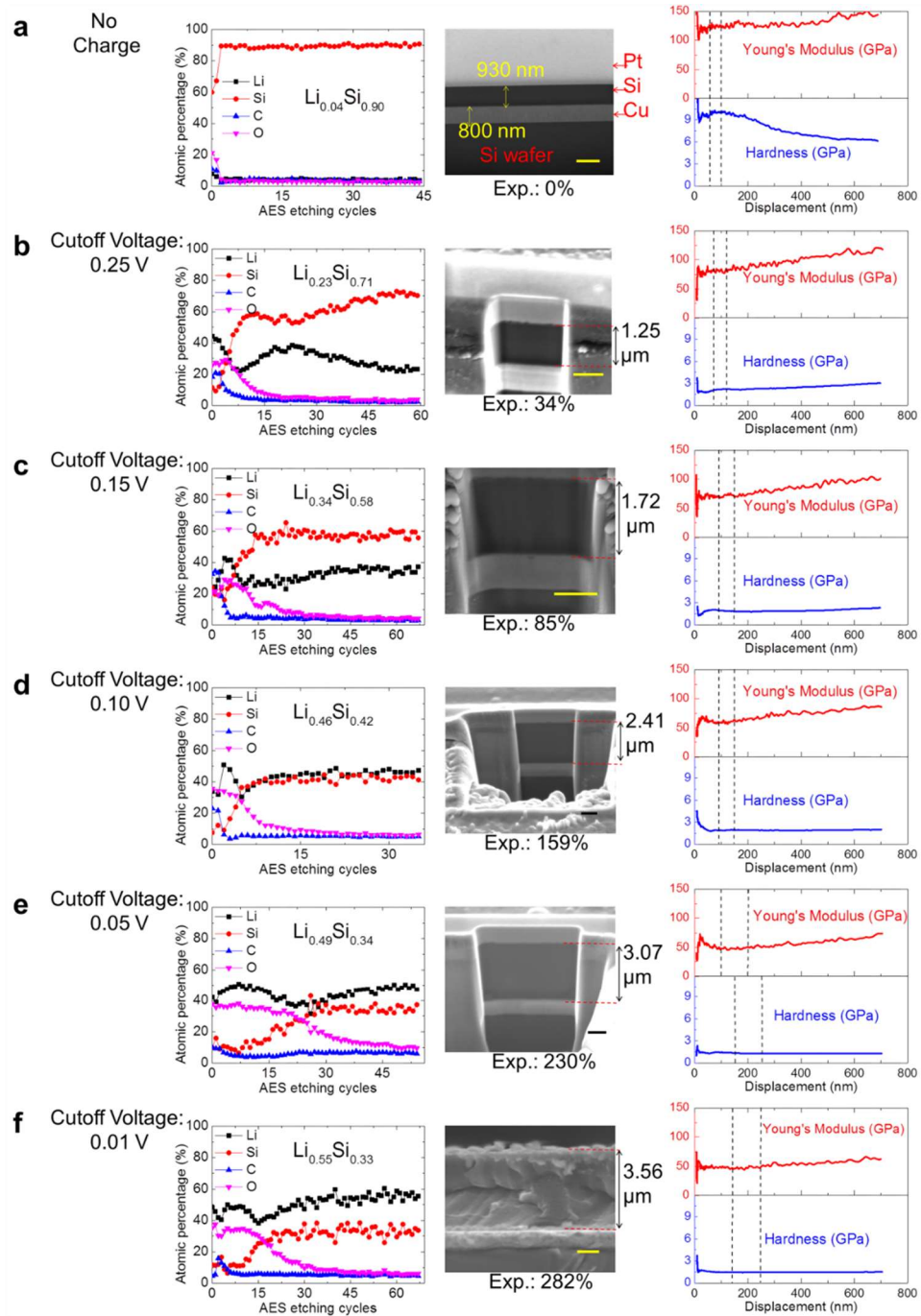


Fig. 2.5 AES, FIB and Nanoindentation measurement. (a) For un lithiated a-Si, the AES profile shows no presence of Li. FIB-SEM shows the thickness of Si layer to be 930 nm. Nanoindentation measures the modulus and hardness of deposited a-Si film to be 124 GPa and 10.6 GPa, respectively. (b) For lithiated a-Si using 0.25 V cutoff voltage, the composition, expansion, modulus and hardness were measured to be $\text{Li}_{0.73}\text{Si}$, 34%, 73GPa, and 2.4GPa, respectively. (c)-(f) Characterizations of lithiated a-Si under 0.15 V, 0.1 V, 0.05 V, and 0.01 V cutoff voltages. Increase of Li composition and expansion and

decrease of modulus and hardness have been observed as lithiation evolves. The length of scale bar in the FIB image is 1 μm .

Figs 2.6a and 2.6b show the Auger spectra of Li and Si after the 30th etching cycle for different cutoff voltages. A clear trend is observed: the intensities of Li peaks are gradually increasing while those of Si peaks are gradually decreasing as Si is lithiated. As AES only measures the relative compositions rather than the absolute values, a widely used absolute ratio is adopted to scale the relative values. Fortunately, in recent years, it has been well studied that Li-Si crystallizes to form metastable crystal $\text{Li}_{3.75}\text{Si}$ when fully lithiated in room temperature rather than the once believed $\text{Li}_{4.4}\text{Si}$ which is alloyed at high temperature^{32,35,36,39,61,80,81}. Using this as a reference ($\text{Li}_{0.55}\text{Si}_{0.33}$ corresponding to $\text{Li}_{3.75}\text{Si}$), all other AES results were scaled accordingly. Fig. 2.6c gives the scaled Li_xSi composition as a function of the cutoff voltage. As this is a direct measurement rather than estimation as in many papers^{48,51,58,59}, the effects of SEI and other parasitic aspects have been ruled out. the estimated Li_xSi composition based on capacity and from many other papers^{58,82} is also plotted. The Li percentage directly calculated from the relationship of $\text{capacity} = \text{current} \times \text{time} / \text{mass}$ is significantly larger than those found by AES. The extra consumption of Li can be attributed to the formation of SEI layer and other parasitic reactions for the battery system using 1 μm Si thin film. One of other papers adopted an assumed relationship between different thermodynamic equilibrium states and cutoff voltages under C/40 constant current charge followed by constant voltage charge⁵⁸. Another one determined three thermodynamic equilibrium states at three cutoff voltages using pair distribution function (PDF) and nuclear magnetic resonance (NMR) under C/100 constant voltage charge⁸². It can be seen that under low current density ($\leq \text{C}/10$), though

both aforementioned methods (ref 27 and 52) use c-Si, the assumption and results determined by PDF and NMR are similar to ours at high lithiated state region. Measured low lithiated state relationship is also provided here while they don't. The directly measured Li_xSi can thus provide a baseline to correlate cutoff voltage to Li-Si composition with similar charging current density. Fig. 2.6d shows the volumetric expansion with normalized Li concentration that is defined as unity for fully charged Si and vanishing for uncharged Si. It is a clearly linear trend. It is important to note that this linear trend is between the volumetric expansion and Li concentration. However, in the majority of theoretical studies, a linear relation has been assumed between linear dimension change to Li concentration, which actually gives a cubic relationship between Si expansion and Li concentration. Again, to show the discrepancy, one typical Si expansion versus Li concentration from existing modeling work is provided^{52,54,56,57}. Therefore, the present direct measurement of volumetric expansion establishes a reference that can be used for high-fidelity modeling and simulations.

Fig. 2.6e and 2.6f show Young's modulus and hardness values as a function of Li fraction. It can be seen that insertion of Li decreases the moduli from 124 GPa (unlithiated) to 46 GPa (fully lithiated) and hardness from 10.6 GPa to 1.71 GPa. The similar trends of decreases in moduli and hardness have been observed in previous studies^{58,59,62-65}. For comparison purposes, the calculated Young's modulus and hardness values using rule of mixtures have also been included. Young's modulus and hardness values of pure Li were taken as 8 GPa and 0.01 GPa^{58,59}, respectively. It is interesting to note that Young's modulus follows the rule of mixture until a Li volume fraction of 0.42, but at higher Li fraction the Young's modulus increases. The same observations have been made in

previous studies^{58,65}. To our knowledge, there are the only two studies to date have been performed where electrochemical route was used to prepare the samples and then nanoindentation was used to obtain mechanical properties^{58,59}. Figs. 2.6g and 2.6h show the comparison with these two studies. Though overall trends are the same, due to the use of a-Si, our results are more consistent with Berla et al⁵⁹. It is also noticed that our results corroborate very well with the results obtained by Berla et al. at higher Li fractions but not at lower concentration of Li. The explanation is that they didn't measure the composition of Li-Si as it is done in this work their samples with Li composition of 52% ($X_{Li}=0.52$) might actually be having much lower concentration of Li, which might have led to high modulus and hardness value.

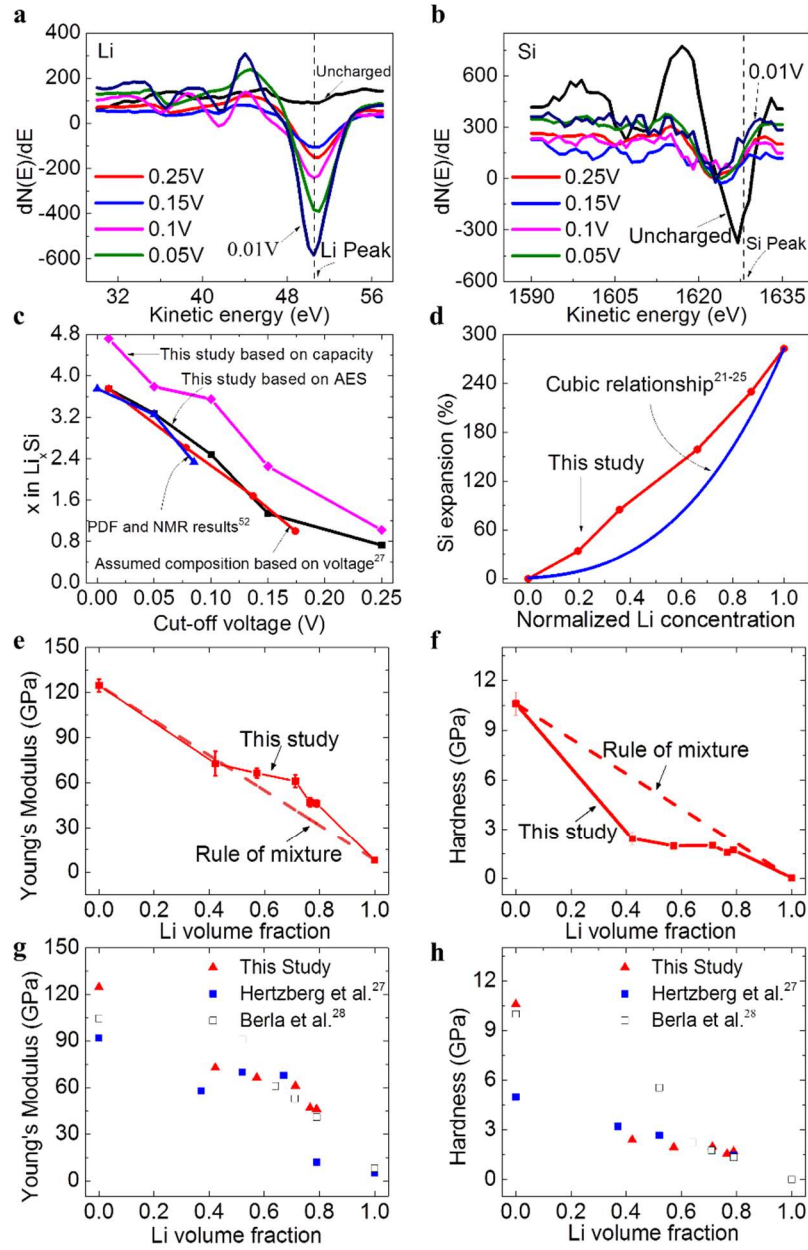


Fig. 2.6 The properties variation of a-Si during lithiation. (a)-(b) Auger spectra of Li and Si after 30th etching cycle. (c) The relationship between cutoff voltages and Li-Si compositions using C/10 constant current charge followed by constant voltage charge. Comparison between the present AES based studies and existing studies based on cutoff voltage is provided. Discrepancies are observed. (d) Volumetric expansion of lithiated a-Si measured by FIB compared with widely used cubic relationship between volumetric expansion and Li concentration in modeling. (e)-(f) The lithiated a-Si modulus and hardness measured by nanoindentation compared with rule of mixture. Modulus follows the rule of mixture still Li volume fraction of 0.42. Hardness does not follow the rule of mixture. (g)-(h) The measured lithiated a-Si modulus and hardness compared with other nanoindentation results.

CHAPTER 3

STRESS-DRIVEN LITHIUM DENDRITE GROWTH MECHANISM AND DENDRITE MITIGATION BY SOFT SUBSTRATES

Introduction

In recent years, lithium (Li) metal-based rechargeable batteries including Li-sulfur (S), Li-air and Li-selenium (Se) batteries are making a strong comeback and being actively pursued for the fast development of electric vehicles and grid storage because of their much higher energy densities compared with Li-ion batteries⁸³⁻⁸⁷. For example, the energy density of Li-S batteries can reach $\sim 2,500 \text{ Wh kg}^{-1}$ or $2,800 \text{ Wh L}^{-1}$, compared to less than 420 Wh kg^{-1} or $1,400 \text{ Wh L}^{-1}$ for Li-ion batteries. While the electrochemical performance of the cathodes in these next-generation batteries are steadily improved⁸⁵⁻⁸⁷, the growth of Li dendrite during plating remains an important problem to be solved, since Li dendrite will not only penetrate separator and cause severe safety issues but also lead to serious capacity decay by consuming both Li and electrolyte. A dendrite-free and smooth deposition of Li is highly desired^{88,89}. Many efforts have been devoted to achieve that goal, such as different liquid electrolytes and additives⁹⁰⁻¹⁰¹, solid electrolytes^{102,103}, applications of mechanical pressure and modification of substrate smoothness¹⁰⁴, adoption of different charging methods¹⁰⁵, artificial SEI (solid-electrolyte-interface)¹⁰⁶⁻¹⁰⁸, and structural design of the electrodes and current collectors^{30,31,109-112}.

Despite the efforts from all these different aspects to tackle the dendrite growth problem, one critical and fundamental aspect has not been widely explored and appreciated, namely, the presence of residual stress in plated Li and its effect on Li growth morphology. Many microstructural evolution phenomena in materials are stress-driven. For example, it

is long known that whiskers can grow from tin films under compressive stress as a stress relief mechanism¹¹³. Since residual stress is ubiquitous in metal plating process^{114,115}, it is logical to ask whether significant stress exists during Li electrodeposition, whether it is the cause of filamentary Li dendrite growth that is widely observed on Li metal anodes^{24,116-118}, and if this undesirable phenomenon can be suppressed through effective control of stress in plated Li.

Here affirmative answers to the above fundamental questions for the first time are provided through novel experiments of plating Li on thin copper (Cu) current collector supported by soft substrates. It is reported that during Li plating, compressive stress in deposited Li causes the surface wrinkling of the underlying Cu current collector supported by a soft substrate, which may evolve from 1D to 2D wrinkle patterns as illustrated in Fig. 3.1a. As a stress relief mechanism, wrinkling reduces the stress in plated Li. Our observation that Li dendrites are absent on wrinkled soft substrate confirms the enabling role of stress in Li dendrite growth. As illustrated in Figs. 3.1b-c, a stress-driven dendrite growth model is proposed to explain the drastic difference of Li growth rate and morphology on hard Cu foils versus soft substrates. In addition to its significance in advancing scientific understanding, It is demonstrated that using soft substrates for Li electrodeposition provides a new way to mitigate Li dendritic growth by eliminating its driving force and hence the root cause. A 3D soft scaffold was fabricated to apply the stress relaxation mechanism on Li-metal anodes under large current density (up to 3 mA cm⁻²). Over 98% coulombic efficiency was achieved for over 200 cycles in a half-cell configuration under current density of 1 mA cm⁻², which overwhelmingly outperforms Cu current collectors. Using lithium iron phosphate (LiFePO₄) as the cathode, full-cell

characterizations exhibit superior cyclic stability with over 99.5% coulombic efficiency. It is believed that the findings in this dissertation will inspire many further studies on stress relaxation during electrochemical plating and open up an unexplored front in the extensive pursuit of Li dendrite suppression strategies with potential implications for other metallic electrode materials.

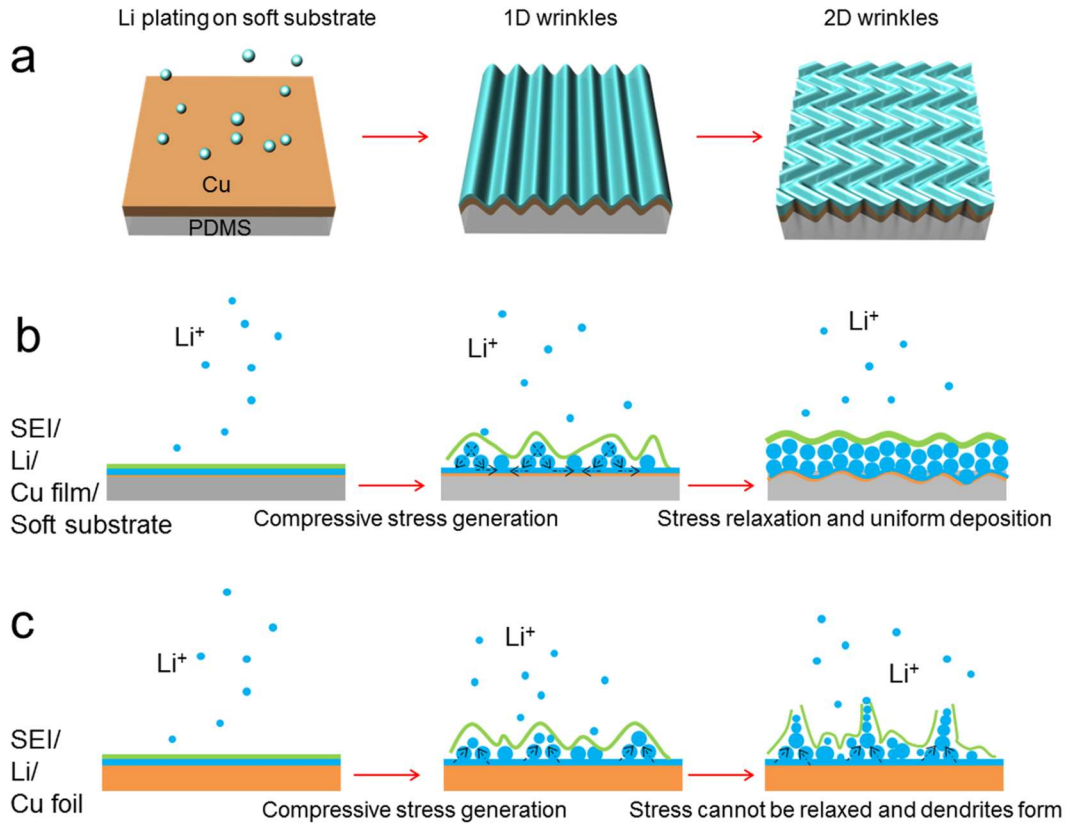


Fig. 3.1 Schematic illustration of Cu thin film wrinkling. (a) Cu thin film wrinkles due to the compressive stress generated during Li plating. (b) Soft substrate releases compressive stress, and thus mitigate Li dendrite growth. (c) Compressive stress causes the generation of Li dendrite on hard electrode during Li plating.

Experiment

PDMS (Sylgard 184, Dow Corning) was prepared by mixing the base and curing agent (10:1 by weight), debubbling, and curing at 80 °C for 2 hours to polymerize and then cutting into 1 cm by 1 cm squares. After that, Chromium (5 nm) and Copper (200 nm, 400

nm or 800 nm) were deposited in sequence on the surface of the PDMS substrate using sputter PVD method (3 mTorr, 100 Watts for both materials). The prepared soft substrate was laminated with an ion-permeable polymer (polypropylene Celgard 2500) as separator and Li metal (0.17 mm, MTI Corp.) as reference and counter electrode. Commercially widely used 1 M LiPF₆ in DEC:DMC:EC (1:1:1) (MTI Corp.) electrolyte was adopted as the electrolyte for 2D substrate test. 1 M lithium LiTFSI in DOL:DME (1:1) with 1% LiNO₃ electrolyte was used for the synergetic combination. For *in-situ* optical microscopy observation, the sandwiched structure was loaded in a customized coin cell with a transparent glass window. For electrochemical testing, the sandwiched structure was sealed and vacuumed in an aluminized polyethylene (PE) pouch (Sigma-Aldrich). For the half cell, the coulombic efficiency test begins with the cycling from 0 to 1 V at 50 μ A to remove surface contamination and stabilize the SEI for 5 cycles^{30,107,112}. Then a fixed amount of Li was plated on the electrodes at different current densities for 1 hour, followed by Li stripping to 1 V. For the full cell testing, LiFePO₄ were adopted as cathode material. LiFePO₄ electrode was prepared by mixing LiFePO₄ powder, polyvinylidene fluoride (PVDF) and conductive carbon additives (mass ratio: 8:1:1) in N-methyl-2-pyrrolidone (NMP) and then casting the mixture casted on an aluminum foil followed by drying in a vacuum oven for 12 h. The average mass loading of LiFePO₄ in the electrode is about 6.5 mg cm⁻². The electrode was first assembled into a half cell using a Li foil as counter electrode. After depositing 2 mAh cm⁻² of Li metal onto the current collector, the cell was disassembled and Li anode was further reassembled into a full cell against LiFePO₄ cathode. The electrolyte was 1 M LiTFSI in DOL:DME (1:1) with 1% LiNO₃ as additive. These

cells were galvanostatically cycled between 2.5 and 4.1 V at 1 mA cm^{-2} . All assembly manipulations were performed in an argon-filled glovebox.

In-situ optical microscopy observation was carried out using a customized coin cell with a transparent glass window at the back. Because of the transparency of the glass and PDMS, the behavior of Cu thin film was captured under an optical microscope (Nikon eclipse lv100, 10X objective). A current density of 1 mA cm^{-2} and a plating time of 1 hour were adopted for all 200 nm, 400 nm and 800 nm thick Cu samples (Fig. 3.2).

For *ex-situ* profilometer experiment, the samples were charged using 1 mA cm^{-2} for 5 minutes and 1 hour. During the experiment, because Li is highly air-sensitive and the oxidation will greatly change the morphology of the Li covered plated surface, directly profiling on the electrode is difficult. However, It was observed that after the removal of Li by DI water and dried, the wrinkled Cu film would not fully recover the initial flat state possibly because of the plastic deformation occurred for Cu during Li plating. This phenomenon was employed to observe the amplitude change of Cu wrinkle after removal of Li for different state of plating.

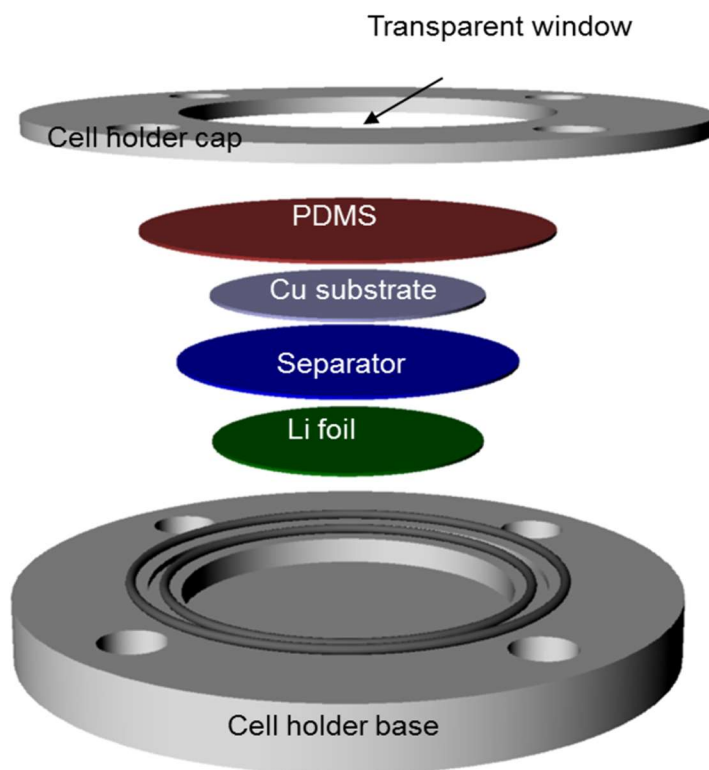


Fig. 3.2 Cell design for optical observation. Due to the transparency of the PDMS soft substrate, optical observations can be conducted to capture the surface wrinkling of the Cu current collector.

After plating of 5 minutes and 1 hour with a current density of 1 mA cm^{-2} , the samples were taken out from the cells and rinsed by an anhydrous dimethyl carbonate (DMC) for a few times to remove the residual electrolyte on the surface of the electrode. During transfer of the samples, special care was taken to minimize the oxidation of the samples. The electrodes were first mounted on a SEM stub and then sealed inside an aluminized polyethylene (PE) packaging bag. All these procedures took place in the glovebox. Finally, the PE bag with the electrode was cut open and quickly transferred to SEM chamber. The total exposure to air time was less than 5 seconds.

The fabrication of 3D soft scaffold started with pouring liquid PDMS (Sylgard 184 with 10:1 ratio) into a porous sugar cube. Silwet were added into the liquid PDMS as the surfactant to change the hydrophobicity of PDMS for the purpose of better coating of Cu on PDMS. To enhance the debubbling and infiltration of PDMS into the porous sugar cube, the PDMS were cured in vacuum oven under 10 Pa and 85 °C for two hours. By placing the PDMS filled sugar cube in hypersonic bench for 1 hour, sugar was washed away. The fabricated porous PDMS were then cut into slices with dimensions to be approximately 1.5 cm × 1.5 cm × 300 μm for latter electroless plating use. The electroless copper plating kit (PC electroless copper, Transene) contains four solutions (A, B, C & D). Solution C is designed for surface sensitizing, solution D for activation and solution A&B for plating. The plating procedures began with immersing the porous PDMS slice into solution C for 15 minutes. After DI water rinse, the sensitized slice was transferred to solution D for activation for 15 minutes. After being activated, the slice was rinsed again and transferred to the mixture solution A&B (1:1) with each volume to be 15 mL. Temperature of the mixture solution were kept to be in the range of 40 °C to 45 °C by using water bath. The plating usually finishes in 15 minutes and the coating thickness is about 0.5 μm. After being taken out, rinsed, and dried in vacuum for 12 hours, the prepared electrode with 3D scaffold can be used for other testing.

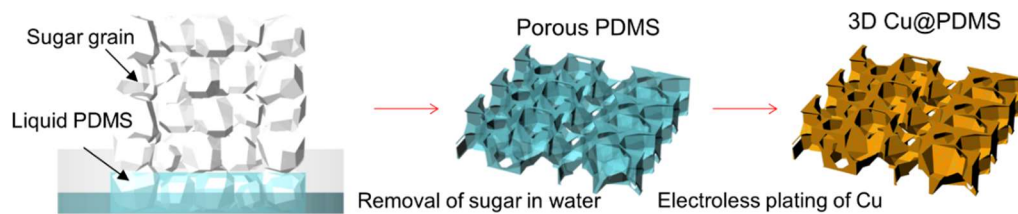


Fig. 3.3 Fabrication of 3D Cu/PDMS substrate. The fabrication begins with placing sugar cube in liquid PDMS, and then removing sugar in DI water to form 3D porous PDMS,

and finally electroless plating Cu on 3D porous PDMS to form 3D porous Cu@PDMS substrate.

Results and discussion

It is hypothesized that when compressive plating stress arises in deposited Li film, it will be transferred to the underlying Cu thin current collector on soft substrate and cause Cu to wrinkle above a threshold membrane strain. Surface wrinkling has been observed in cases where compressive stress in thin films deposited on soft substrate is generated by temperature mismatch¹¹⁹ and mechanical force¹²⁰. Theoretical analyses showed that the membrane strain is small¹²⁰⁻¹²². For 1D wrinkling pattern, the threshold membrane strain

for the onset of wrinkling is given by $\varepsilon_m = -\frac{1}{4} \left[\frac{3E_s(1-\nu_f^2)}{E_f(1-\nu_s^2)} \right]^{\frac{2}{3}}$, where E is the modulus, ν

is the Poisson's ratio, and subscripts “s” and “f” represent substrate and thin film, respectively. Polydimethylsiloxane (PDMS) is used as the soft substrate in our study. Using the typical material properties of the PDMS and Cu¹²³, $E_s = 2.6$ MPa, $\nu_s = 0.48$, $E_f = 110$ GPa, $\nu_f = 0.34$, the membrane strain ε_m in the electroplated Li is -0.047% . Consequently, the compressive stress in deposited Li upon wrinkling is estimated to be $\sigma_m = E\varepsilon_m = -2.3$ MPa by using $E = 4.9$ GPa as the elastic modulus of electroplated Li¹²⁴. This value is well below the yield strength of micro-sized Li¹²⁵ and the compressive residual stress level that has been measured in electrodeposited Sn¹¹⁵ and Cu¹¹⁴. The above estimation suggests that the Cu/PDMS soft current collector is likely to wrinkle during Li plating. This hypothesis is testified in the following.

Here PDMS is used as the soft substrate, Cu thin film as the current collector, Li foil as the counter electrode, and 1M LiPF₆ in DEC:DMC:EC (1:1:1) as the electrolyte in which severe Li dendrite growth occurs. Fig. 3.4 shows the *in-situ* optical microscope and *ex-situ* profilometer observations of the evolution of the electroplated Li on thin Cu current collectors with different thickness (200 nm, 400 nm, and 800 nm) on PDMS substrates, under a current density of 1 mA cm⁻². In order to perform the *in-situ* microscope observation (Figs. 3.4a-i), the Cu/PDMS substrates were placed in a customized coin cell with glass window on the back and thus the electroplating behavior can be observed under an optical microscope through the glass window and transparent PDMS¹²⁶ (Fig. 3.2). It can be found that, the initially flat Cu thin films (Figs. 3.4a-c) all wrinkle upon Li electroplating and the wrinkle patterns evolve from 1D patterns (Figs. 3.4d-f) to 2D patterns (Figs. 3.4g-i). These observations verify the presence of the electroplating-induced compressive stress in Li and the resulted wrinkling on soft substrates. Interestingly, the emergence of 1D wrinkle is a sudden process and it happens once the compressive force exerted from the electroplated Li to the thin Cu current collector exceeds the critical stress for wrinkling; while the evolution from the 1D to 2D wrinkle patterns is a gradual process where the 1D wrinkle patterns gradually bend upon further Li electroplating (or further compression of the thin Cu current collector). It is also found that during the wrinkle evolution as Li is continuously electroplated on Cu thin current collector, wrinkle wavelength remains almost unchanged and is linearly dependent on the Cu thickness. For example, for 200 nm, 400 nm and 800 nm-thick Cu, the average wavelengths are approximately 25 μm, 50 μm and 100 μm, respectively, which can be explained by the small deformation wrinkle theory where the wrinkle wavelength is independent of the compressive strain but linearly

depends on the thin film thickness^{120,121}. The phenomenon is apparently different from that of Si thin film lithiation on PDMS, in which Si wrinkles evolve from 1D to 2D with continuous wavelength decrease due to the large deformation (up to ~400%) during Li insertion into Si¹²⁶ and can be explained by the large deformation theory¹²⁷.

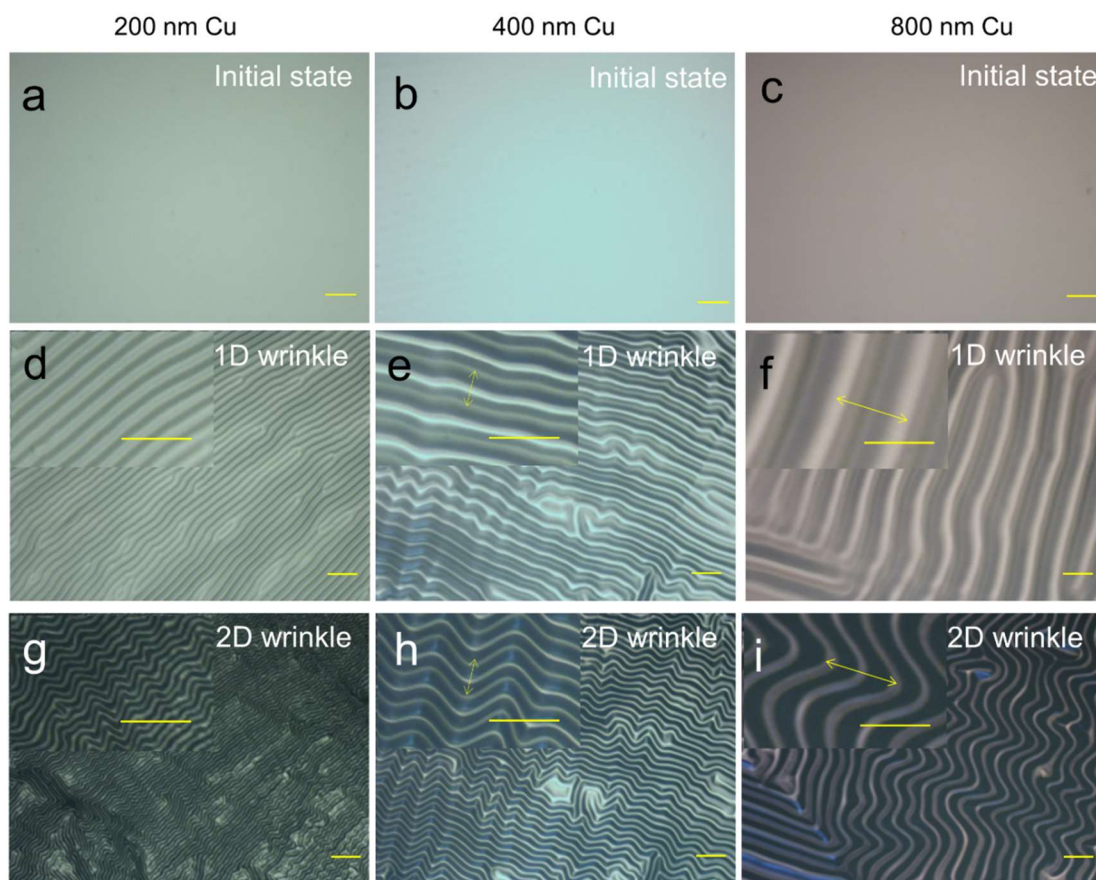


Fig. 3.4 Optical observation of Cu current collectors. (a-c) The initial flat states of the 200 nm, 400 nm and 800 nm Cu thin film current collectors. (d-f) The formation of 1D wrinkles after a short period of Li plating on 200 nm, 400 nm, and 800 nm-thick Cu current collectors. The according wrinkle wavelengths are approximately 25 μm , 50 μm and 100 μm , respectively. (g-i) 2D wrinkles with approximately the same wavelength as 1D wrinkles after 1 hour Li plating for all three Cu current collectors. All scale bars in (a-i) represent 100 μm . All experiments were carried out using a current density of 1 mA cm^{-2} .

To further investigate the electroplating behavior and wrinkle evolution, samples with different electroplating time (5 minutes and 1 hour) for all the three Cu thicknesses

(i.e., 200 nm, 400 nm, and 800 nm) were examined under *ex-situ* optical profilometer. The results (Figs. 3.5a-i) again show that the wavelength approximately does not change with the electroplating time but only depends on Cu thickness. However, the wave amplitudes become clearly larger with increased electroplating time. The wrinkling behavior can be explained by the small deformation mechanics model, where the amplitude A and

wavelength λ are given by $A = h \sqrt{4 \left[\frac{E_f (1 - \nu_s^2)}{3E_s (1 - \nu_f^2)} \right]^{\frac{2}{3}} \varepsilon_{exerted} - 1}$ and $\lambda = 2\pi h \left[\frac{E_f (1 - \nu_s^2)}{3E_s (1 - \nu_f^2)} \right]^{\frac{1}{3}}$.

Here h is the thickness of the Cu current collector and $\varepsilon_{exerted}$ is the exerted strain from electroplated Li to the Cu current collector. The model predicts that as $\varepsilon_{exerted}$ increases with increasing the electroplating time, buckling amplitude A increases and wavelength λ keeps constant, which agrees with the experiments. More quantitatively, using the material properties of the PDMS and Cu¹²³, the model gives buckling wavelength 29.0 μm , 58.0 μm and 116.0 μm for 200 nm, 400 nm, and 800 nm Cu current collectors, respectively, which agrees well with the measured mean wavelengths (25 μm , 50 μm and 100 μm).

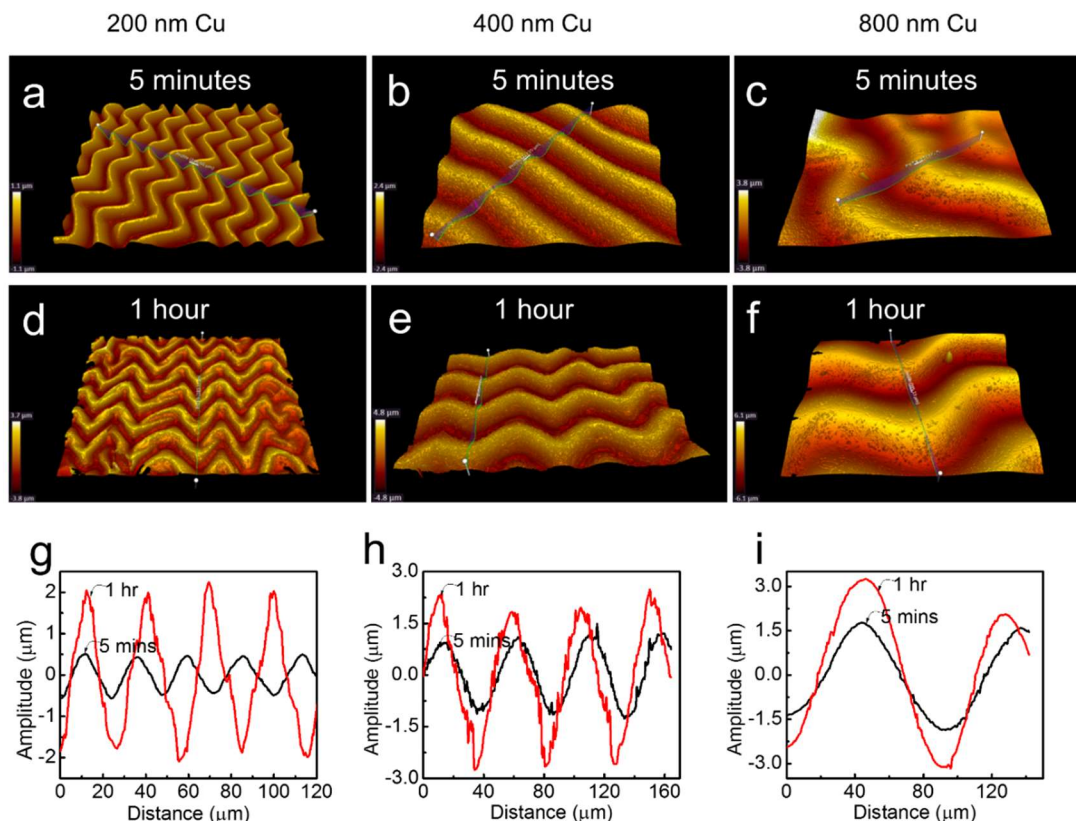


Fig. 3.5 Profilometer observation of Cu current collectors. Cu surface profiles after 5 minutes (a-c) and 1 hour Li plating (d-f). (g-i) The wavelength and amplitude values after 5 minutes and 1 hour Li plating for the three Cu current collectors with different thickness. All experiments were carried out using a current density of 1 mA cm^{-2} .

Now Li morphology is examined by electroplating on two different substrates for comparison, namely thin Cu current collectors on PDMS substrate that has stress relaxation mechanism, and thick commercial Cu foil as the hard substrate without stress relaxation¹⁰⁹. Fig. 3.6 shows the scanning electron microscopy (SEM) images of electrochemically plated Li at early plating stage (5 minutes) and after 1 hour with a current density of 1 mA cm^{-2} . Significantly different Li morphologies are observed on hard (Cu foil) and soft substrates (800 nm Cu on PDMS in Fig. 3.6). After 5 minutes of plating on Cu foil (Fig. 3.6a), it can be found that many Li protrusions have formed and the overall Li deposit is very uneven due to localized Li accumulation on these protrusions. On the contrary, Li growth on the

soft Cu/PDMS substrate (Fig. 3.6b) starts with small Li flat “pads”, which eventually grow into bigger round humps. No sharp Li tips can be found. These humps are uniformly distributed on the soft Cu/PDMS substrate, suggesting no localized Li deposition. The dash lines in Fig. 3.6b highlight the wrinkle profiles. After plating for one hour on hard Cu foil (Fig. 3.6c), large amount of Li dendrites or filaments with varied dimensions and sharp tips formed. In contrast, after 1 hour of plating on soft Cu/PDMS substrate (Fig. 3.6d), the early formed Li humps coalesced and formed a continuum and smooth coverage. Even after 100 cycles of plating and stripping, Li morphologies on hard Cu foils and soft Cu/PDMS substrates remain very different. As shown in Fig. 3.6e, dense Li dendrite-shaped “forests” formed on hard electrode while plated Li remain relatively flat on soft substrate. These results clearly indicate that stress relaxation plays a significant role on Li morphology during plating/stripping.

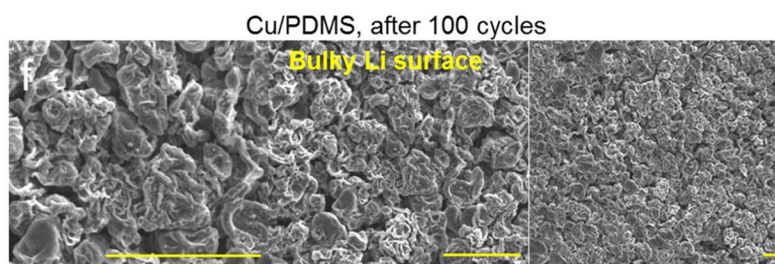
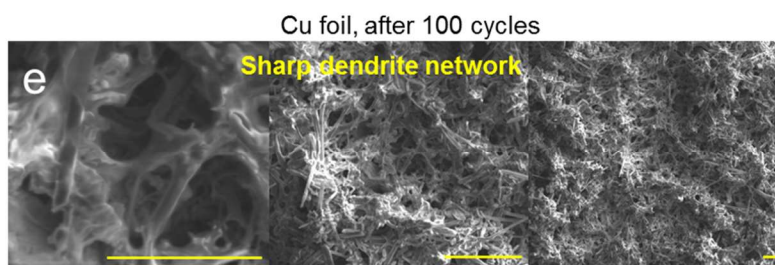
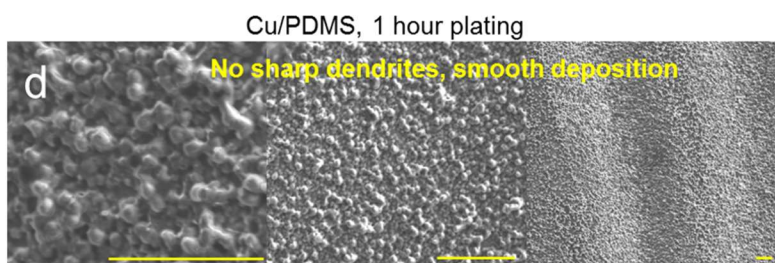
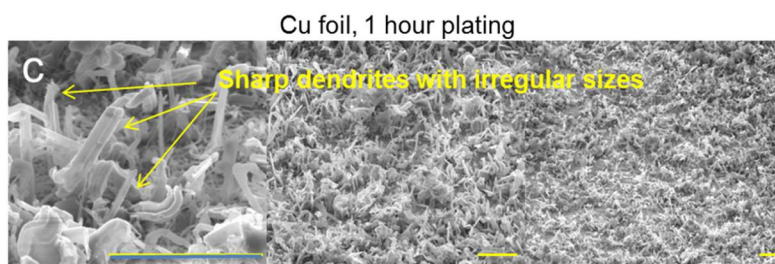
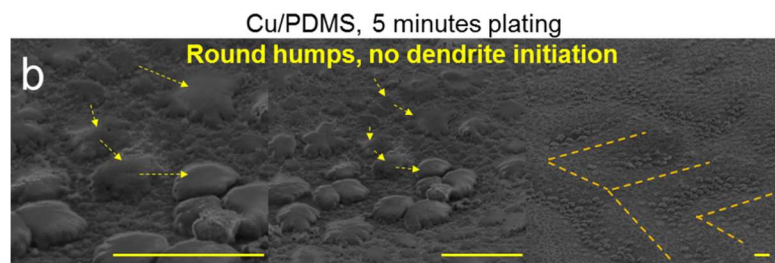
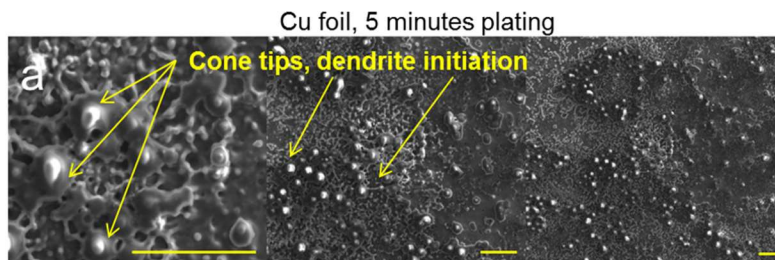


Fig. 3.6 SEM observation of Li morphology. After 5 minutes plating, (a) cone shape Li tips initiation and very uneven distribution of Li on Cu foil hard electrode and (b) the growth of Li from flat “pads” to round “humps” and even distribution of Li humps on Cu/PDMS soft substrate. After 1 hour plating, (c) Li dendrites of random dimensions and sharp tips on Cu foil hard electrode and (d) uniform and smooth Li film formed by the connection of Li humps on Cu/PDMS soft substrate. After 100 cycles plating (1 hour plating and stripping to 1 V for each cycle), (e) Li dendrite network formed on Cu foil hard electrode and (f) flat Li surface without sharp Li dendrite on soft Cu/PDMS substrate. All scale bars represent 10 μm . All experiments were carried out using a current density of 1 mA cm^{-2} .

The markedly different Li morphology on hard Cu foils and soft substrates is clear evidence that stress is an important driving force for Li dendrite growth. The growth of Li dendrites is often viewed as an analogy to the diffusion-induced interface instability phenomena in Cu and Zn electrodeposition, where dendrite formation results from ion depletion in electrolyte at growth front. However, there is notable difference between the two types of microstructures, including the filamentary morphology of individual Li protrusions and their root-growing behavior^{116,118,128} versus the tip-growing ramified fractal structures seen in Cu and Zn. Recently Bai et al.¹¹⁸ reports that Li dendrite growth transitions from the root-growing to tip-growing behavior around the Sand’s time¹²⁹, which confirms that early-stage Li dendrite growth is governed by a mechanism different from diffusion-limited interface instability. The root-growing Li filaments bear striking similarity to whisker growth in tin thin films^{113,130}, which is a stress relaxation phenomenon. In fact, Li dendrite growth as a stress relief mechanism has been suggested¹¹⁶, though it did not receive widespread recognition due to the lack of a detailed working mechanism and experimental support. With our soft substrate experiments confirming the role of stress in Li dendrite growth, a stress-driven growth model is hereby proposed based on the prevailing understanding of tin whisker growth^{113,131}, which is summarized in Fig. 3.7a.

Our model postulates that the same necessary conditions that lead to tin whisker growth should also be satisfied to enable stress-driven Li dendrite growth. They include: (1) compressive stress: the presence of compressive stress in the Li layer has been confirmed by our experiments (Figs. 3.4 and 3.5) and it is the driving force for the push-out of Li filaments through localized diffusional creeps. The estimated stress level at ~ 100 MPa without stress relaxation is in very good agreement with the recently reported yield strength of micro-sized Li¹²⁵, (2) surface passivation: it prevents stress relaxation by diffusion of atoms to the film surface. Consequently, stress relief can only be achieved by localized protrusions at defective surface sites. For Li plating, the SEI plays the role of the passivating layer. (3) subsurface planar defects: they serve as atomic sinks or vacancy sources during diffusional creep to support root-growing whiskers. As shown in Fig. 3.7a, newly nucleated surface grains during Li electrodeposition can be an important type of subsurface planar defects as for tin whisker growth^{113,131}, in addition to buried crystal impurities¹³².

To use the proposed mechanism to understand the stress effect on Li dendrite growth, the growth of Li filaments is considered from surface grains with a geometry shown in Fig. 3.7b. The criterion for dendrite initiation is set as when the filament growth rate v_{filament} is larger than the uniform Li deposition rate v_{plating} , i.e., $v_{\text{filament}} > v_{\text{plating}}$. Here v_{plating} is readily given by $v_{\text{plating}} = jV_{\text{Li}} / F$, where j is the plating current density, F is Faraday's constant, and V_{Li} is the molar volume of Li. The growth of Li filaments is assumed to result from a steady-state Li flux J [mol s⁻¹] towards its base, which is driven by the stress-induced Li chemical potential difference between the bulk and the grain boundaries beneath the filament. The filament growth rate is thus given by $v_{\text{filament}} =$

$JV_{\text{Li}}/\pi r^2$, where r is the filament radius. Details on the calculation of stress-dependent J are provided in the Methods, which shows that J depends on the compressive stress σ and the effective Li diffusivity D_{Li} in the Li layer. To predict v_{filament} on hard Cu foils, the yield strength of micro-sized Li (100 MPa)¹²⁵ is used for σ and the Li lattice self-diffusivity at room temperature ($2 \times 10^{-15} \text{ m}^2 \text{ s}^{-1}$)¹³³ for D_{Li} , and estimate an average filament size $2r = 250 \text{ nm}$ from SEM. Fig. 3.7c shows that v_{filament} varies weakly with the opening angle of the filament base θ between 8.4 and 9.8 nm s^{-1} , which is in reasonable agreement with the experimental value of $5 - 10 \text{ nm s}^{-1}$ estimated from SEM (Fig. 3.6c). The calculated v_{filament} is much larger than $v_{\text{plating}} = 1.3 \text{ nm s}^{-1}$ at $j = 1 \text{ mA cm}^{-2}$, and hence dendrite growth occurs during Li deposition on hard Cu foils. In comparison, when σ is set to the threshold stress (2.3 MPa) upon the wrinkling of the Cu/PDMD soft substrate, v_{filament} is reduced to below 0.3 nm s^{-1} and much less than v_{plating} . Therefore, the use of Cu/PDMS soft substrate can effectively prevent Li dendrite growth.

It is also found that the numerically calculated filament growth rate can be well approximated by the analytical expression $v_{\text{filament}} = D_{\text{Li}} V_{\text{Li}} \sigma / RT r$ obtained from ref.¹³¹ which is shown as the red dashed line in Fig. 3.7c. Using this expression, the critical stress is obtained below which Li dendrite will be mitigated,

$$\sigma_c = \frac{RT}{FD_{\text{Li}}} j r(j) \quad (3-4)$$

For the current density $j = 1 \text{ mA cm}^{-2}$ used in the experiment, σ_c is equal to $\sim 16 \text{ MPa}$ and well exceeds the wrinkling stress of the Cu/PDMS substrate ($\sim 2.3 \text{ MPa}$) and thus Li dendrite growth is mitigated. Eq. 3-4 can serve as a useful guidance in the selection and

design of soft substrate materials and geometry, provided that the deposited Li grain size is known.

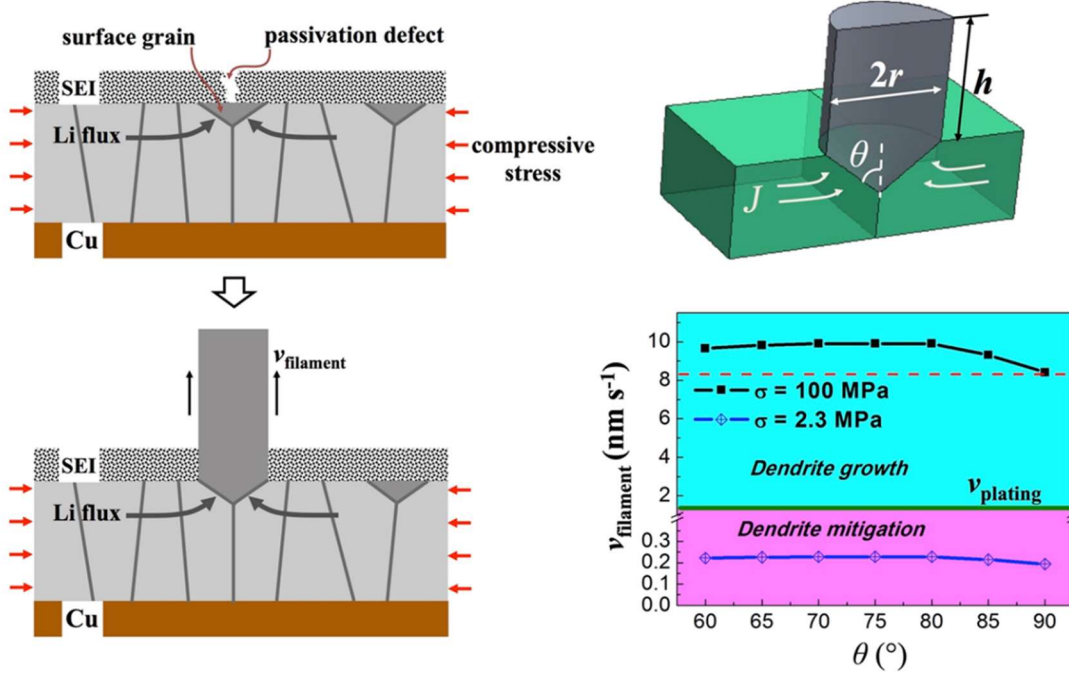


Fig. 3.7 Stress-driven Li whisker growth model. (a) Schematic of the stress-driven Li dendrite growth mechanism. (b) Geometry of a Li filament growing from a surface grain considered in the filament growth rate calculation. Only one half of the structure is shown. (c) Predicted Li filament growth rate v_{filament} as a function of θ for compressive residual stress $\sigma = 100$ MPa (black squares) and 2.3 MPa (blue diamonds). θ is limited to the range of $60^\circ - 90^\circ$ as only surface grains with $\theta > 60^\circ$ were found to grow into tin whiskers⁵². Also plotted in the figure are the uniform Li plating rate v_{plating} (solid line) and v_{filament} evaluated by the analytical expression given in the main text (red dashed line).

In the calculation, a Li whisker or filament is assumed to grow from a shallow surface grain and have a cylindrical shape of radius r as shown in Fig. 3.7b. It forms cone-shaped grain boundaries with the surrounding grains, with θ being the opening angle of filament base. The root-growing behavior of the filament results from a Li diffusion flux towards the base grain boundaries, which is driven by the Li chemical potential gradient

near the surface grain. Here Li chemical potential is defined as the free energy change upon inserting a Li atom into the system. Inside the bulk of the Li film, it is given by

$$\mu_{bulk} = \mu_0 - \sigma\Omega, \quad (3-1)$$

where μ_0 is the chemical potential in the absence of stress, σ (<0) is the compressive residual stress in the thin film and Ω is the atomic volume of Li. When the Li film is under compression, it takes less energy to insert a Li atom into the grain boundaries beneath a shallow surface grain, with the local chemical potential given by

$$\mu_{gb} = \mu_0 - \sigma_n^{gb}\Omega = \mu_0 - \sigma \cos^2 \theta \Omega, \quad (3-2)$$

where $\sigma_n^{gb} = \sigma \cos^2 \theta$ is the normal stress on the grain boundaries. For compressive stress $\sigma < 0$, $\mu_{gb} < \mu_{bulk}$ and Li atoms will flow towards the grain boundaries through localized diffusional creep. Assuming that Li diffusion is steady-state, The chemical potential distribution near the surface whisker grain is determined by solving the diffusion equation $\nabla^2 \mu = 0$ with the boundary conditions Eqs. 3-1 and 3-2 and the zero-flux boundary condition $\nabla \mu \cdot \hat{n} = 0$ at the Li film surface. The problem is numerically solved in COMSOL with axisymmetry assumed for the chemical potential with respect to the filament axis. The total Li flux [mole/sec] arriving at the base grain boundaries is then calculated as

$$J = \iint_{gb} \frac{D_{Li}}{RT} \frac{\partial \mu}{\partial n} \bigg|_{gb} dS, \quad (3-3)$$

where D_{Li} is the effective Li diffusivity in the deposited film and k is the Boltzmann's constant. Using Eq. 3-3, the Li filament growth velocity is given by $v_{filament} = JV_{Li}/\pi r^2$.

Result and discussion

The absence of Li dendrites on Cu/PDMS soft substrates suggests improved cycling performance over Li electrodeposition on hard Cu current collectors. This is confirmed by cycling experiments of half cells, which are detailed in the Fig. 3.8. To achieve a symmetrical system between Cu and Li foil, excessive amount of Li (5 mAh cm^{-2}) was plated on both Cu foil and Cu/PDMS substrate by 1 mA cm^{-2} plating and 0.5 mA stripping for 10 cycles using commercial electrolyte (1M LiPF_6 in DEC:DMC:EC (1:1:1)). After that a current density of 0.25 mA cm^{-2} was used for both plating and stripping for a total of 100 cycles. From the voltage-time profiles, it can be observed that voltage fluctuation is severe after 60 cycles for Cu foil while soft Cu/PDMS substrate exhibits stable cycling. In Fig. 3.8c, The upper panel shows that the CE of Cu foil substrate drops dramatically at around 60th cycle which can be ascribed to short circuit in the cell caused by sharp dendrites; while for the Cu/PDMS substrate, no sudden drop of CE was observed for over 100 cycles under a current density of 1 mA cm^{-2} and 1 hour plating and stripping to 1 V for each cycle. It can be also found that when using commercial electrolyte (1M LiPF_6 in DEC:DMC:EC (1:1:1)), though Cu/PDMS substrate has better CE performance than Cu foil substrate, CE is still fluctuating and the magnitude is as low as 90%. To further improve the CE performance, 1 M lithium bis(trifluoromethanesulfonyl)imide (LiTFSI) in cosolvent of 1,3-dioxolane (DOL) and 1,2-dimethoxyethane (DME) (1:1) with 1% LiNO_3 as electrolyte was examined for both substrates. From lower panel, it can be seen that both substrates have improved CE stability and CE values and Cu/PDMS substrate still outperforms Cu foil substrate. However, because of the natural disadvantages of the 2D substrate (low surface area and direct exposure to the electrolyte), even for the soft substrate, the CE becomes less stable after 50 cycles, which certainly calls for a better design. Consequently,

the 3D porous and soft scaffold was synthesized as discussed in the main text. Fig. 3.8d shows separators of Cu foil hard and Cu/PDMS soft substrates examined by SEM after 100 cycling half-cell tests using LiPF₆ as the electrolyte. It can be seen that the separator of Cu foil substrate is highly distorted with enlarged pores that may be resulted from the growth of sharp dendrites while the separator of Cu/PDMS substrate remains intact after cycling. The scale bar is 5 μm . All the results show that Cu/PDMS soft substrate significantly outperforms Cu foil under the same cycling conditions. The comparison unambiguously demonstrates the beneficial effect of stress relaxation on increasing the stability of Li metal anode even in carbonate-based electrolyte.

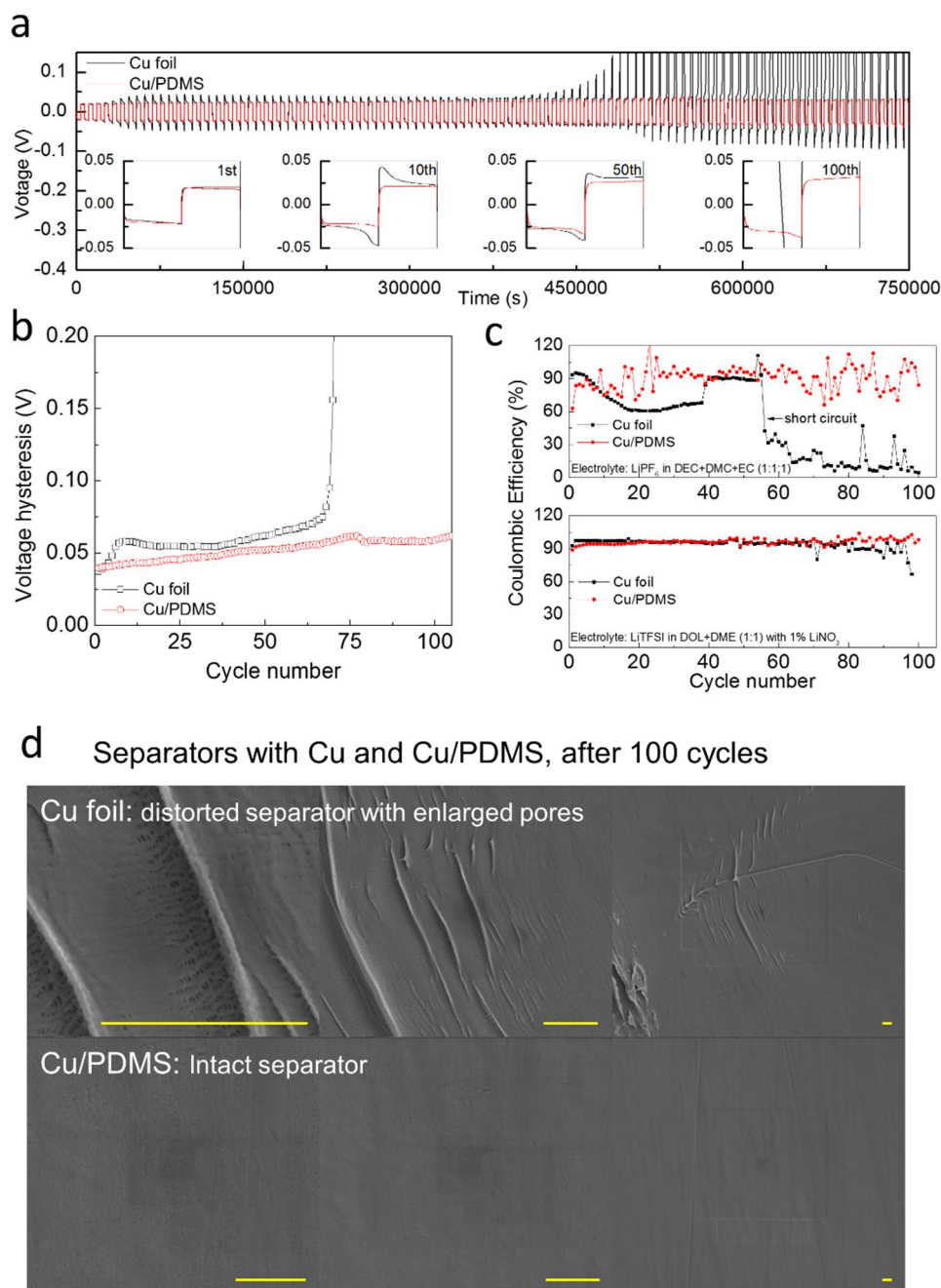


Fig. 3.8 Cycling experiments of Cu/PDMS and Cu as electrodes.

Building upon the baseline experiments of Li electrodeposition on Cu/PDMS substrates (Fig. 3.8), the synergy between stress relaxation and other existing Li dendrite mitigation approaches was further explored with focus on two aspects: (a) create 3D

substrate structures^{30,112} to increase surface area of the Cu/PDMS current collector and thus reduce the plating current and Li thickness, and (b) combine the present soft substrates with new electrolyte additives¹¹⁷. Here 3D soft scaffold was developed using 1 M lithium LiTFSI in DOL:DME (1:1) with 1% LiNO₃ as the electrolyte that has shown improved cyclic behavior¹¹⁷. Fig. 3.9a illustrates the fabrication process of the 3D soft scaffold and the details are provided in Methods. In short, sugar cubes were used as the pore generation template¹³⁴. Liquid PDMS (Sylgard 184 with 10:1 ratio) is mixed with Silwet¹³⁵ (as the surfactant to change the hydrophobicity of PDMS) and infiltrated into the porous sugar cube for the subsequent step. After curing the PDMS and washing away the sugar, a 3D, porous, and hydrophilic PDMS structure was formed. Then electroless deposition was applied to conformally and uniformly coat Cu as current collector throughout the interconnected 3D porous PDMS, which is referred as 3D Cu@PDMS substrate. Thus a 3D soft scaffold was fabricated. The SEM image shows the average pore size is in a range between 50 μm and 200 μm , and the wall thickness is around 50 μm .

The cycling coulombic efficiencies (CE) of using Cu foil, a 3D Cu@PDMS substrate, and a commercial 3D Cu foam electrode with similar pore size were tested. The CE test begins with the galvanostatically cycling of the electrodes at 50 μA from 0 to 1 V to remove surface contamination and stabilize the SEI for 5 cycles^{30,107,112}. Then Li was plated at current densities of 1 mA cm^{-2} , 2 mA cm^{-2} and 3 mA cm^{-2} for 1 hour (i.e., three different areal capacity of 1 mAh cm^{-2} , 2 mAh cm^{-2} and 3 mAh cm^{-2}), followed by Li stripping to 1 V for all the three electrodes. From Figs. 3.9a-3.9c, it can be observed that the 3D Cu@PDMS soft substrate has significantly improved performance than those of Cu foil and 3D Cu foam electrodes. Under a current density of 1 mA cm^{-2} (Fig. 3.9a), the 3D

Cu@PDMS substrate shows stable CE for more than 200 cycles with an average CE magnitude about 98%; while both Cu foil and 3D Cu foam electrodes have lower CE magnitudes close to 95% and 90%, respectively, and become unstable after 90 cycles. For higher current density of 2 mA cm^{-2} (Fig. 3.9b), the 3D Cu@PDMS soft substrate still achieves more than 180 stable cycles with CE close to 98% while Cu foil has less than 50 stable cycles and 3D Cu foam exhibits widely fluctuating CE values from the beginning. Even under large areal current density of 3 mA cm^{-2} (Fig. 3.9c), the Cu@PDMS soft substrate still has quite stable CE for about 100 cycles. On the contrary, both Cu foil and 3D Cu foam show unstable CEs from the very beginning. This result also agrees with earlier conclusion¹¹², which claims that 2D Cu foil and 3D Cu foam with pore size larger than $100 \text{ }\mu\text{m}$ do not have stable CE during cycling under 1 mA cm^{-2} with 1 mAh cm^{-2} of Li. Here by replacing the hard 3D Cu structure with soft 3D Cu scaffold, It is shown that even for pore size larger than $100 \text{ }\mu\text{m}$, the CE can still be stable for more than 200 cycles.

The voltage profiles under the current density of 1 mA cm^{-2} using Cu foil, 3D Cu foam, and 3D Cu@PDMS substrate are presented in Figs. 3.9d-5f. It is found that the 3D Cu@PDMS has the smallest increase of the Li plating plateau voltage from the 30th to 90th cycles (specifically, 3 mV from 21 mV to 24 mV as shown in Fig. 3.9f), compared with 13 mV for Cu foil electrode (Fig. 3.9d) and 200 mV for 3D Cu foam (Fig. 3.9e). Moreover, the voltage hysteresis (Fig. 3.9g) shows that the 3D Cu@PDMS substrate has the smallest and most stable hysteresis (60 mV), compared with 120 mV hysteresis for Cu foil and >300 mV hysteresis for the Cu foam. The low plateau voltage increment and small hysteresis of 3D Cu@PDMS soft substrate may be explained by the formation of a more stable SEI resulted from the relaxation of stress using the soft substrate.

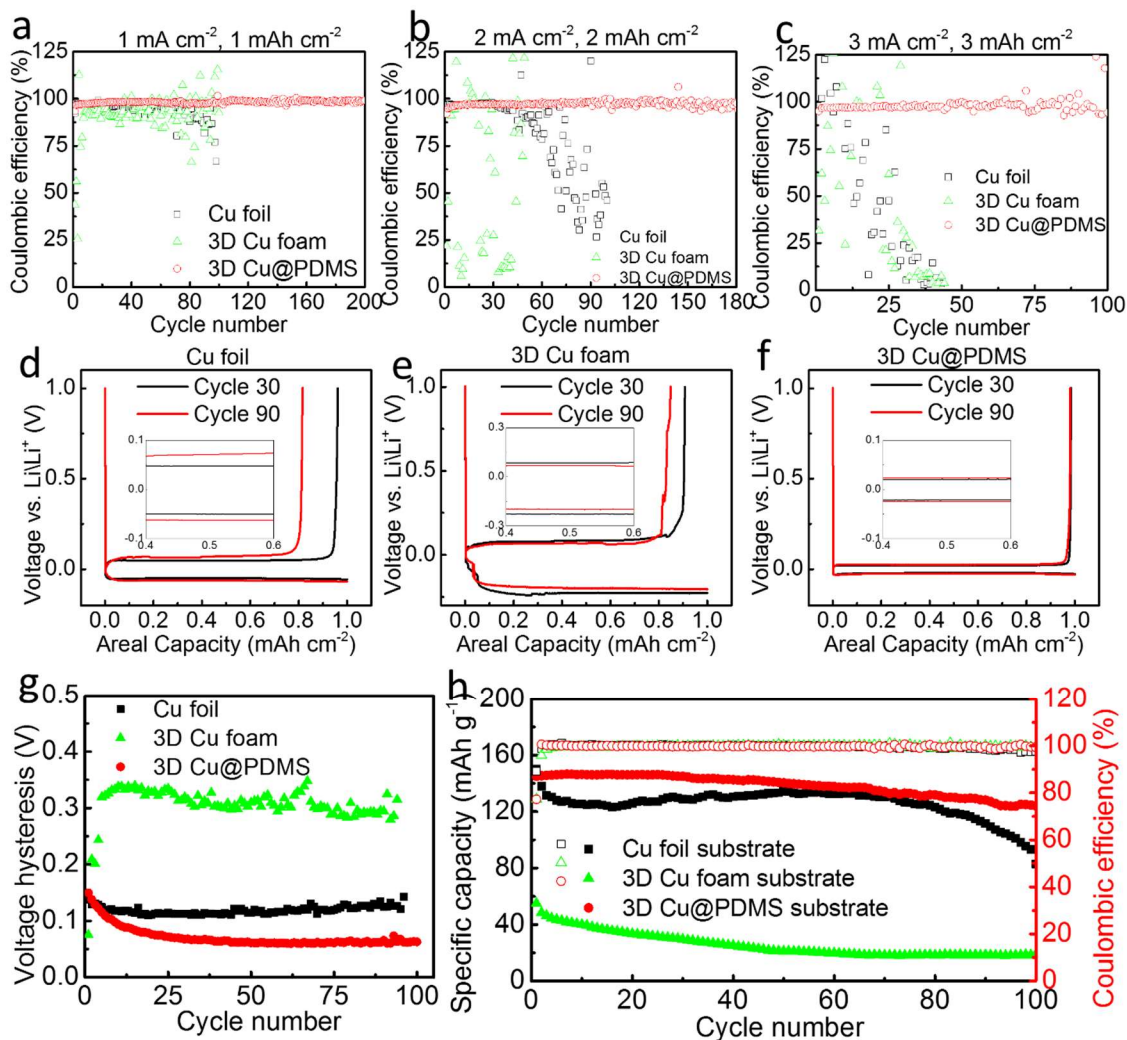


Fig.3.9 Characterization of 3D Cu@PDMS substrates. (a-c) Comparison of coulombic efficiency (CE) of Li plating/stripping on flat Cu foil, 3D Cu foam and 3D Cu@PDMS substrate under current densities of 1 mA cm⁻², 2 mA cm⁻², and 3 mA cm⁻². (d-f) Voltages profiles of (d) Cu foil, (e) 3D Cu foam and (f) 3D Cu@PDMS substrate at the 30th (black) and 90th (red) cycles under a current density of 1 mA cm⁻². (g) Comparison of the hysteresis of Li plating/stripping for Cu foil, 3D Cu foam and 3D Cu@PDMS substrate under a current density of 1 mA cm⁻². (h) Cycling performance of full cell for Cu foil, 3D Cu foam and 3D Cu@PDMS substrate under a current density of 1 mA cm⁻² using LiFePO₄ as the cathode.

Full cell was assembled to demonstrate the potential practical application of the 3D soft electrode. For comparison, three anode current collectors using Cu foil, 3D Cu foam, and 3D Cu@PDMS substrate were utilized. 2 mAh cm⁻² of Li was pre-deposited on these

three anodes. Cathode was LiFePO_4 with areal capacity of 1 mAh cm^{-2} . A galvanostatic current of 1 mA cm^{-2} was employed for the cycling test with voltage window of $2.5 \sim 4.1 \text{ V}$. From Fig. 3.9h, it can be observed that the cycling performance of the 3D Cu@PDMS substrate is much more stable than that of Cu foil and Cu foam substrates. The capacity of 3D Cu@PDMS retains 85.6% by decreasing from 145 mAh g^{-1} to 124 mAh g^{-1} with an average coulombic efficiency greater than 99.5% for 100 cycles. However, the capacity in the case of Cu foil drops from 150 mAh g^{-1} to 83 mAh g^{-1} with a retention rate of only 55.3%. The 3D Cu foam electrode has the lowest capacity and capacity retention of 34.4% by decreasing from 55 mAh g^{-1} to 19 mAh g^{-1} . The voltage profiles are provided in Fig. 3.10a. The anodes before and after the test were examined under SEM (Fig. 3.10b). It can be seen that Li has relatively smooth morphology on 3D Cu@PDMS substrate as against disrupted shapes on Cu foil and Cu foam.

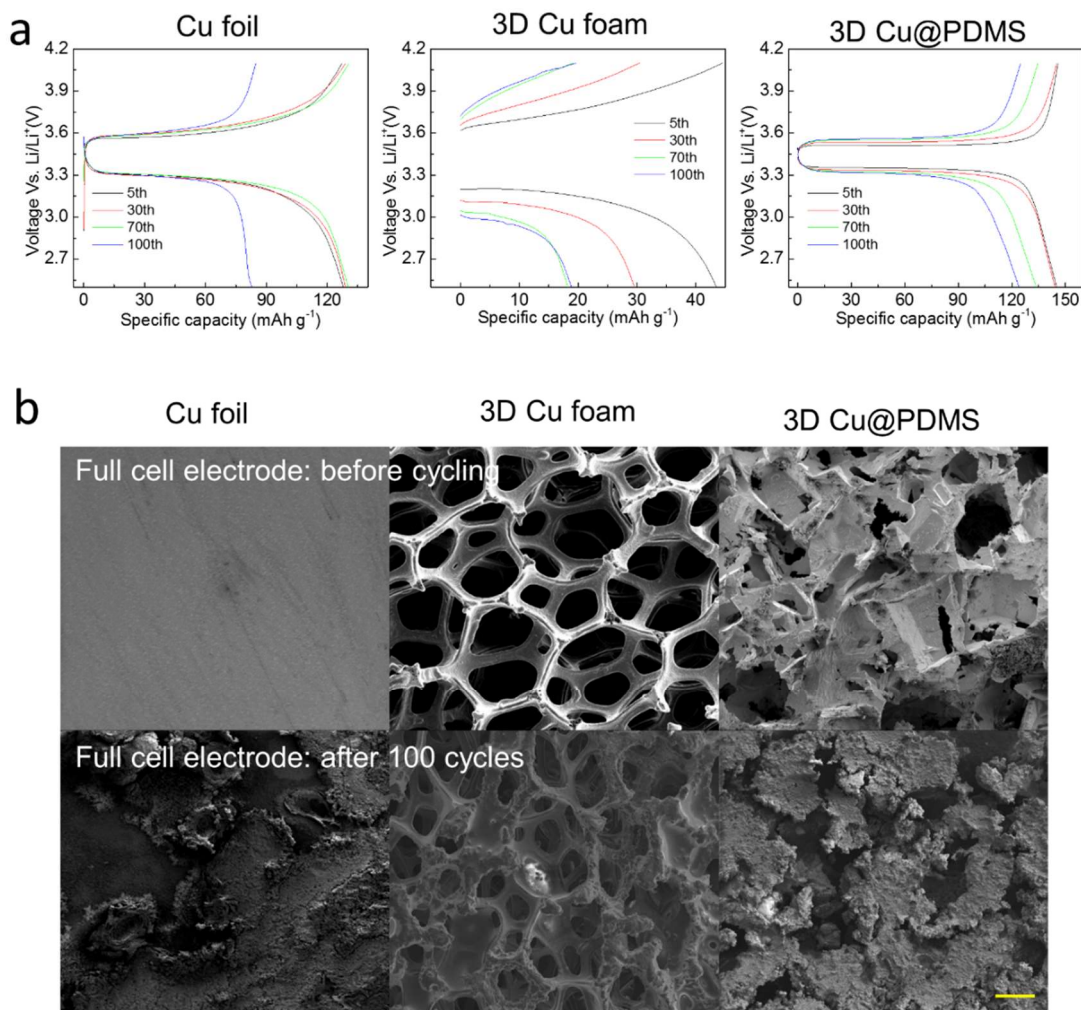


Fig. 3.10 Voltage profiles and SEM images of 3D Cu@PDMS substrates. (a) Full cell voltage-capacity profiles for Cu foil, Cu foam and 3D Cu@PDMS substrates. Voltage-capacity profiles at 5th, 30th, 70th and 100th. The electrode using 3D Cu@PDMS substrate clearly has the smallest capacity decay and voltage hysteresis. (b) SEM images of the anodes in a full-cell configuration (LiFePO₄ as the cathode) before and after 100 cycles for Cu foil, Cu foam and 3D Cu@PDMS substrates. Relatively smooth morphology can be observed for the electrode using 3D Cu@PDMS substrate, as compared with disrupted shapes using Cu foil and Cu foam.

It is noted that the large thickness ($\sim 300 \mu\text{m}$) of the PDMS scaffold inverted from cane sugar cubes results in a relatively low energy density of the battery cells. However, there exists vast potential to improve the specific and volumetric capacity offered by the 3D Cu/PDMS soft substrate through scaffold structure optimization. As a demonstration,

a modified fabrication process is described with glucose powder replacing sugar cubes as the sacrifice. As glucose has a much smaller grain size than sugar cubes, much thinner ($\sim 50\ \mu\text{m}$) PDMS scaffolds with reduced pore sizes ($10\text{--}50\ \mu\text{m}$) can be obtained.

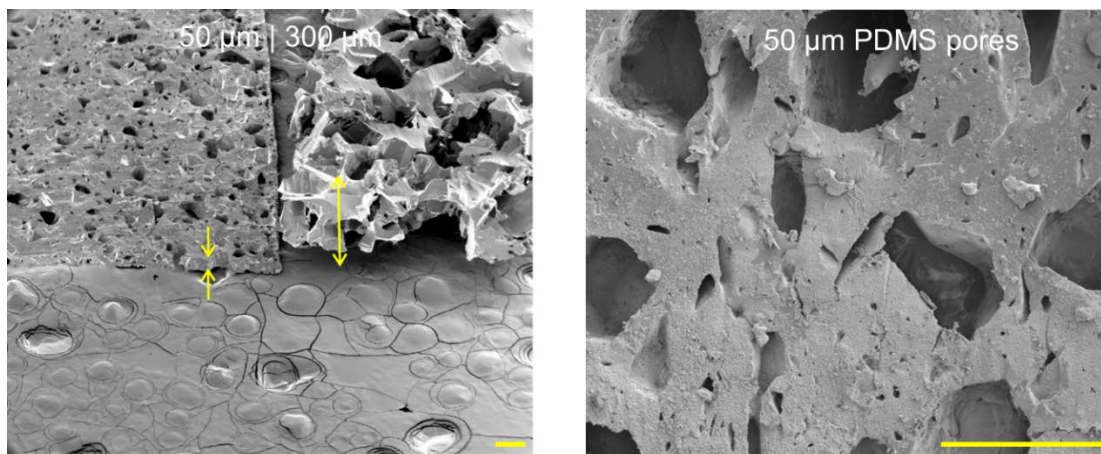


Fig. 3.11 SEM images of the two generation 3D Cu@PDMS substrates. (a) Comparison of porous PDMS substrates with a thickness of 300 μm (right) vs 50 μm (left). (b) Top view of a 50 μm -thick porous PDMS substrate shows the reduced pore size. All scale bars represent 100 μm .

The second-generation 3D porous PDMS was prepared by mixing the base (30g), curing agent (3g) and glucose (15g, Aladdin), stirring for 10 minutes, and then curing at 80 °C for 2 hours. After solidification, PDMS contained glucose was cut into slices with thickness of 50 μm by using Ultra-Thin Semiautomatic Microtome (Leica RM2245). After that, placing the slices into deionized water and ultrasonic treatment for 4 hours to completely remove the glucose. By using glucose which has much smaller grain size (tens of microns) than that of Sugar cube (hundreds of microns), combined with Ultra-Thin Semiautomatic Microtome, the 300 μm thick 3D porous PDMS has been greatly reduced to as thin as 50 μm and the pore size has also been reduced from the level of 200~300 μm to the level of 10~50 μm as from Fig. 3.11.

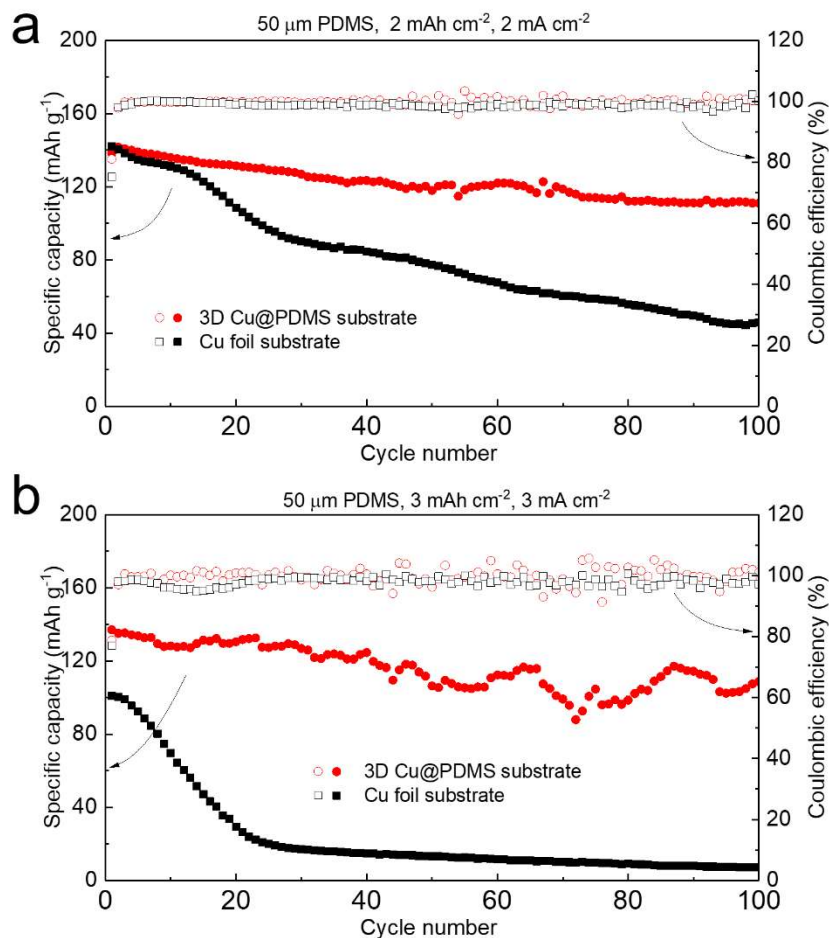
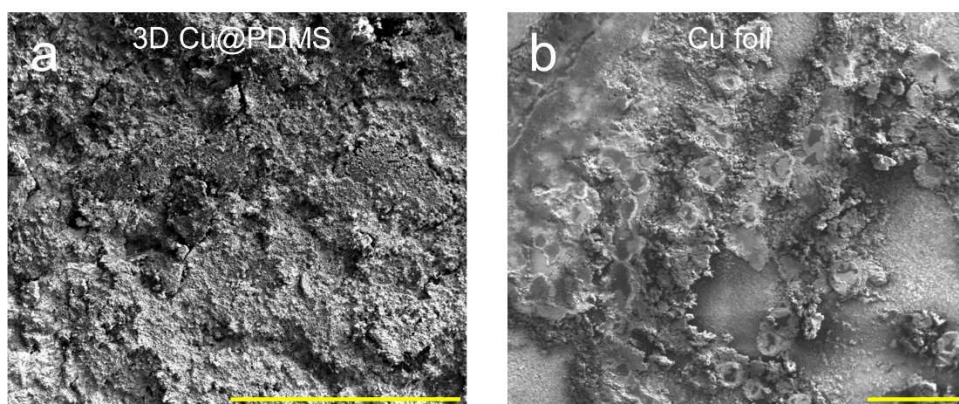


Fig. 3.12 Cycling test of the second-generation 3D Cu@PDMS substrate. (a) 2 mAh cm^{-2} capacity loading cell under a current density of 2 mA cm^{-2} . (b) 3 mAh cm^{-2} capacity loading cell under a current density of 3 mA cm^{-2} .

Full cell was tested with elevated capacity loading of 2 mAh cm^{-2} and 3 mAh cm^{-2} under current density of 2 mA cm^{-2} and 3 mA cm^{-2} for both new 3D Cu@PDMS electrode and Cu foil electrode. In fabricating full cell, 2 mAh cm^{-2} and 3 mAh cm^{-2} Li was predeposited on both electrodes. As seen from Fig. 3.11, the new electrodes still dramatically outperform Cu foil electrode for both mass loadings. For 2 mAh cm^{-2} batteries, the capacity of 3D Cu@PDMS retains over 80% by decreasing from 138 mAh g^{-1} to 111 mAh g^{-1} with an average coulombic efficiency greater than 99.5% for 100 cycles. The capacity in the case of Cu foil drops from 142 mAh g^{-1} to 46 mAh g^{-1} with a retention rate

of only 32%. For 3mAh cm⁻² batteries, the capacity of 3D Cu@PDMS retains over 78% by decreasing from 137 mAh g⁻¹ to 108 mAh g⁻¹ with an average coulombic efficiency greater than 99.5% for 100 cycles and the capacity for Cu foil drops from 101 mAh g⁻¹ to 7 mAh g⁻¹ with a retention rate of only 7%. The severe degradation for Cu foil is due to highly non-uniform deposition of Li under the high current density of 3 mA cm⁻². The SEM images from Fig. 3.13 show smooth deposition for 3D Cu@PDMS electrodes rather than the heavily disrupted surface for Cu foil electrode. It is noted that the tested Li electrode on the 3D Cu@PDMS soft substrate displays a relatively low Coulombic efficiency in the first cycle (Fig. 3.12), which is also observed for other types of 3D current collectors^{30,112} and likely contributed by severe SEI formation due to the large surface area of deposited Li in the 3D structures. This issue may be alleviated by the pre-deposition of excess Li or the use of synergistic electrolyte additives such as lithium polysulfide combined with lithium nitrate¹¹⁷, which has been shown to increase the initial Coulombic efficiency of Li anode in DOL:DME from 71% to 93%³⁰.

After 100 cycles, 2 mAh cm^{-2} , 2 mA cm^{-2}



After 100 cycles, 3 mAh cm^{-2} , 3 mA cm^{-2}

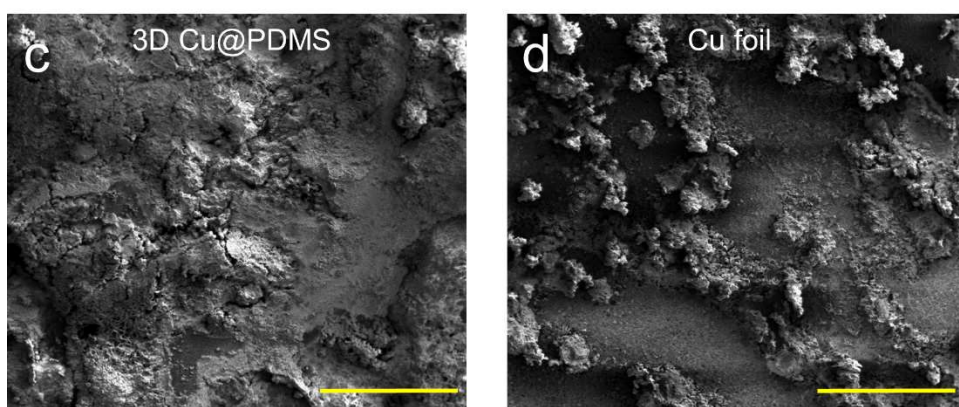


Fig. 3.13. Morphology of the thin 3D Cu@PDMS and Cu foil after 100 cycles. Relatively smooth morphology can be observed for the electrode using 3D Cu@PDMS substrate (a, c), as compared with disrupted shapes using Cu foil (b, d). All scale bars represent 500 μm .

It is also noted that the 3D Cu@PDMS electrode can maintain a stable thickness over repeated cycling as compared with planar Cu current collector. As shown by the cross-section SEM images in Fig. 3.14, the thickness of the Li layer plated on planar Cu current collector increases more than two-fold after 100 cycles (a-c). In contrast, the 3D Cu@PDMS electrode thickness displays little change after first lithiation, and increases by less than 15% after 100 cycles (d-f), which confirms that the majority of plated Li is accommodated inside the pores of the 3D structure. At last, the specific and volumetric

capacity of the Li metal anode based on the second-generation 3D/PDMS substrate are compared with those of graphite anode assuming a typical capacity loading level of 3 mAh cm⁻² for commercial batteries:

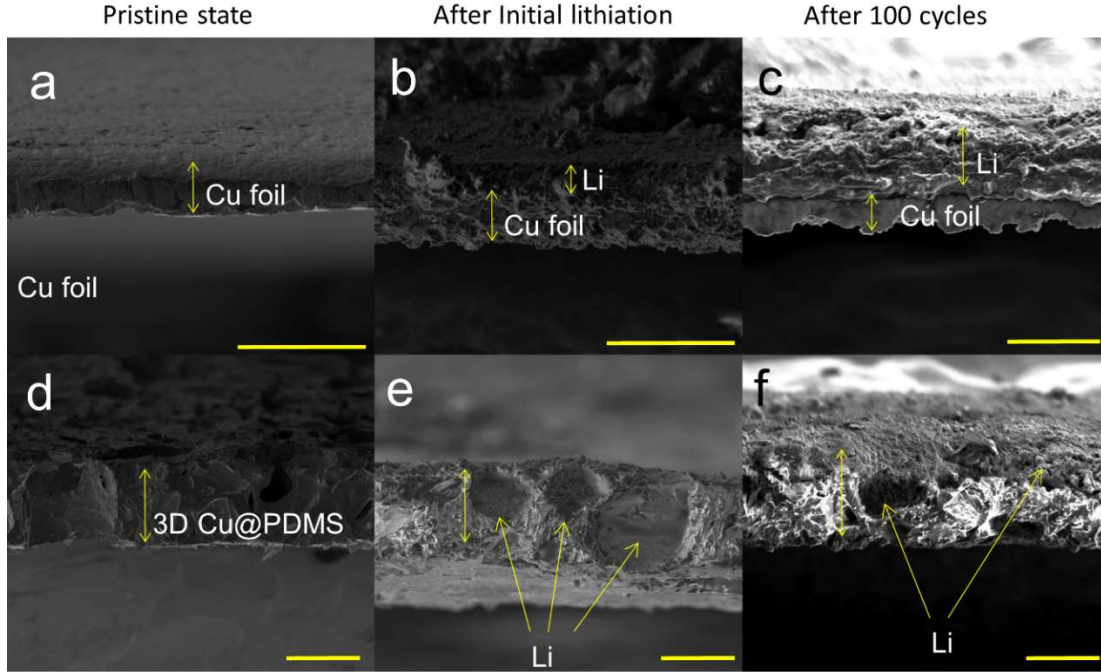


Fig. 3.14 Thickness change of the thin 3D Cu@PDMS electrode upon cycling. (a-c) Cross-section SEM images of a planar Cu current collector in its pristine state (a), after first lithiation (b) and after 100 cycles (c). (d-f) Cross-section view of a 3D Cu@PDMS substrate in its pristine state (d), after first lithiation (e) and after 100 cycles (f). The scale bar is 50 μ m.

The following material parameters are used in the calculation: Li density $\rho_{Li} = 0.543 \text{ g} \cdot \text{cm}^{-3}$, Cu density $\rho_{Cu} = 8.93 \text{ g} \cdot \text{cm}^{-3}$, PDMS density $\rho_{PDMS} = 0.965 \text{ g} \cdot \text{cm}^{-3}$, graphite specific capacity $C_{sp}^{Graphite} = 372 \text{ mAh} \cdot \text{g}^{-1}$, graphite density $\rho_{graphite} = 1.6 \text{ g} \cdot \text{cm}^{-3}$ (allowing pores), and Li specific capacity $C_{sp}^{Li} = 3840 \text{ mAh} \cdot \text{g}^{-1}$.

The specific and volumetric capacities of the graphite anode in commercial Li-ion batteries are calculated as

$$C_{sp}^{graphite} = 3\text{mAh}/(m_{graphite} + m_{CC}) \quad (3-1)$$

$$C_V^{graphite} = 3\text{mAh} \cdot \text{cm}^{-2} / (t_{graphite} + t_{CC}) \quad (3-2)$$

where $m_{graphite}$ (m_{CC}) and $t_{graphite}$ (t_{CC}) are the mass and thickness of graphite anode (or Cu current collector), respectively. Commercial graphite electrode typically consists of 95w% graphite, 5w% binder and conductive additive, and has a thickness of $t_{graphite} = 50\mu\text{m}$ for a battery cell with an areal capacity of 3mAh cm^{-2} . Cu foil used for current collector on the anode side has a typical thickness of $10\mu\text{m}$. Considering the double-sided coating configuration, the foil thickness associated with each anode is $t_{CC} = 5\mu\text{m}$. With these inputs, one obtains $C_{sp}^{graphite} = 230\text{mAh g}^{-1}$ and $C_V^{graphite} = 545\text{mAh cm}^{-3}$.

In the 3D Cu@PDMS electrode, the electrode consists of PDMS (thickness t_{PDMS} , porosity Φ , volume $V_{PDMS} = t_{PDMS} \times 1\text{cm}^2$), Cu thin film deposited inside porous PDMS (mass m_{Cu}), predeposited Li (mass m_{Li}). Some quantities are experimentally measured, such as $t_{PDMS} = 50\mu\text{m}$, $\Phi = 45\%$, $m_{Cu} = 0.00034\text{g}$, and the predeposited Li was calculated using the theoretical capacity of Li, . The specific capacity and volumetric capacity density are given by

$$C_{sp}^{3D} = 3\text{mAh} / (m_{PDMS} + m_{Cu} + m_{Li}) \quad (3-3)$$

$$C_V^{3D} = 3\text{mAh} / V_{PDMS} \cdot \quad (3-4)$$

For the present 3D Cu@PDMS electrode with a thickness of $50\mu\text{m}$, its specific energy is calculated to be $C_{sp}^{3D} = 793\text{mAh g}^{-1}$, which is more than 3 times as high as that

of the graphite anode, while offering a comparable volumetric energy density

$$C_V^{3D} = 600mAh\ cm^{-3}.$$

It is note that there is plenty of room for further increase in the capacity and energy density of the 3D electrode by optimizing its structure, e.g. increasing the porosity and/or reducing the PDMS thickness. To demonstrate its potential, the calculated specific capacity and volumetric capacity of the 3D Cu@PDMS electrode are plotted as functions of its porosity Φ and PDMS thickness t_{PDMS}^{3D} in Fig. 3.15, where the performance of the present 50 μ m-thick electrode is indicated by the “★” symbol.

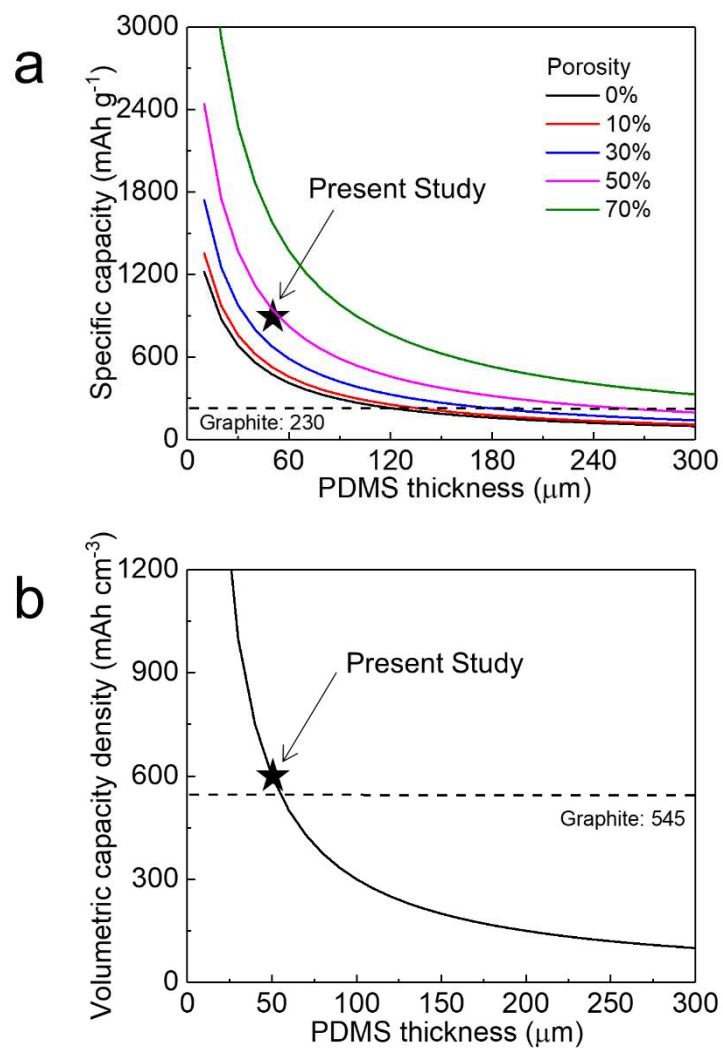


Fig. 3.15 Projected capacities of the 3D Cu@PDMS electrode. Specific capacity (a) and volumetric capacity (b) vs electrode porosity and PDMS thickness for a cell with an areal capacity of 3 mAh cm^{-2} , with “★” indicating their values for the $50\mu\text{m}$ -thick electrode fabricated in this work.

CHAPTER 4

CONCLUSIONS

In this dissertation, a rigorous and thorough study has been conducted to understand some essential problems in lithiated a-Si as anodes under conventional charging rates of C/3 and C/10. While in-situ TEM observation uncovers lithiation mechanism under high charging rate, the present study provides practically useful references for the conventional battery system under conventional current density. It is found that the lithiation process of a-Si in a conventional charging rate is a single-phase reaction. It's a critically important contribution to the understanding of lithiation mechanism under normal charging rate because one can expect much smaller stress in the more homogenous single-phase reaction. Also, volume expansion, Li-Si composition, and modulus/hardness were measured in parallel for the same sample and rigorously correlated. The findings in this dissertation establish a reference to quantify some key metrics of lithiated a-Si as anodes, and can be used to rationally design a-Si based high-performance LIBs guided by high-fidelity modeling and simulations.

On the other hand, the relationships between stress and dendrite growth during electrochemically plating of Li have also unveiled. The presence of compressive stress during plating and its role on Li dendrite growth has been confirmed. It is found out that, by releasing the compressive stress using soft substrates, Li dendrites can be effectively mitigated and hence electrochemical performance can be improved. The stress generation and relaxation mechanisms have been successfully explained by a theoretical model. Moreover, a synergetic combination using soft substrates, 3D architecture and novel electrolyte additives leads to a 3D soft scaffold to further harness this favorable stress

relaxation behavior. The significantly improved CE (even at very high current density) and capacity performance indicate a great potential toward the practical application of the Li metal anode. Finally, it is also believed that the findings in this dissertation will inspire many further studies on stress relaxation during electrochemical plating and initiate a not fully appreciated front in the extensive pursuit of Li dendrite suppression strategies with potential implications for other metallic electrode materials.

CHAPTER 5

FUTURE WORK

Beyond the work in this dissertation, the following two interesting questions which are closely related to the subject already discussed above remain very to be explored.

Based on the understanding of Si mechanical behaviors during lithiation, a Si-C composite electrode will be constructed and studied toward a more realistic application of Si in Li-ion batteries. Specifically, some key metrics such as stress, expansion, capacity of the composite electrode will be obtained. The problem can be modeled in two dimensions: particle and electrode dimension. In the particle level, Si and graphite will be treated as randomly distributed spheres with given mass ratio. The coupled mass diffusion and large deformation calculation will be performed in this level to solve the concentration and stress field in the particle. Globally, in the electrode level, usually along the thickness direction, solid potential, electrolyte potential and electrolyte concentration fields will be solved.

On the other hand, despite the demonstration of thinning down the 3D porous soft electrode, it is still not optimal geometrically. For example, a 30 μm thin electrode with pore size close to 10 μm is highly desired, which remains further investigation. Also, electrochemistry-wise, many other strategies such as high capacity cathode and solid electrolyte can be combined with our porous soft electrode to increase the cell level energy density.

REFERENCES

- 1 Nazri, G.-A. & Pistoia, G. *Lithium batteries: science and technology*. (Springer Science & Business Media, 2008).
- 2 Liu, X. H. *et al.* In situ TEM experiments of electrochemical lithiation and delithiation of individual nanostructures. *Advanced Energy Materials* **2**, 722-741 (2012).
- 3 Kim, H., Han, B., Choo, J. & Cho, J. Three-dimensional porous silicon particles for use in high-performance lithium secondary batteries. *Angewandte Chemie* **120**, 10305-10308 (2008).
- 4 Arie, A. A., Chang, W. & Lee, J. K. Effect of fullerene coating on silicon thin film anodes for lithium rechargeable batteries. *Journal of Solid State Electrochemistry* **14**, 51 (2010).
- 5 Kim, Y.-L., Sun, Y.-K. & Lee, S.-M. Enhanced electrochemical performance of silicon-based anode material by using current collector with modified surface morphology. *Electrochimica Acta* **53**, 4500-4504 (2008).
- 6 Liu, Y. *et al.* Improvement of cycling stability of Si anode by mechanochemical reduction and carbon coating. *Journal of Power Sources* **189**, 480-484 (2009).
- 7 Si, Q. *et al.* Highly reversible carbon–nano-silicon composite anodes for lithium rechargeable batteries. *Journal of Power Sources* **189**, 761-765 (2009).
- 8 Wang, X., Wen, Z., Liu, Y. & Wu, X. A novel composite containing nanosized silicon and tin as anode material for lithium ion batteries. *Electrochimica Acta* **54**, 4662-4667 (2009).
- 9 Ma, H. *et al.* Nest-like silicon nanospheres for high-capacity lithium storage. *Advanced Materials* **19**, 4067-4070 (2007).
- 10 Park, M.-H. *et al.* Silicon nanotube battery anodes. *Nano letters* **9**, 3844-3847 (2009).
- 11 Cui, L.-F., Ruffo, R., Chan, C. K., Peng, H. & Cui, Y. Crystalline-amorphous core– shell silicon nanowires for high capacity and high current battery electrodes. *Nano letters* **9**, 491-495 (2008).
- 12 Cui, L.-F., Yang, Y., Hsu, C.-M. & Cui, Y. Carbon– silicon core– shell nanowires as high capacity electrode for lithium ion batteries. *Nano letters* **9**, 3370-3374 (2009).

- 13 Kim, H. & Cho, J. Superior lithium electroactive mesoporous Si@ Carbon core-shell nanowires for lithium battery anode material. *Nano letters* **8**, 3688-3691 (2008).
- 14 Bourderau, S., Brousse, T. & Schleich, D. Amorphous silicon as a possible anode material for Li-ion batteries. *Journal of power sources* **81**, 233-236 (1999).
- 15 Chen, L., Xie, J., Yu, H. & Wang, T. An amorphous Si thin film anode with high capacity and long cycling life for lithium ion batteries. *Journal of Applied Electrochemistry* **39**, 1157-1162 (2009).
- 16 Jung, H., Park, M., Han, S. H., Lim, H. & Joo, S.-K. Amorphous silicon thin-film negative electrode prepared by low pressure chemical vapor deposition for lithium-ion batteries. *Solid State Communications* **125**, 387-390 (2003).
- 17 Lee, K.-L., Jung, J.-Y., Lee, S.-W., Moon, H.-S. & Park, J.-W. Electrochemical characteristics of a-Si thin film anode for Li-ion rechargeable batteries. *Journal of Power Sources* **129**, 270-274 (2004).
- 18 Maranchi, J., Hepp, A. & Kumta, P. High capacity, reversible silicon thin-film anodes for lithium-ion batteries. *Electrochemical and solid-state letters* **6**, A198-A201 (2003).
- 19 Zhang, T. *et al.* The structural evolution and lithiation behavior of vacuum-deposited Si film with high reversible capacity. *Electrochimica Acta* **53**, 5660-5664 (2008).
- 20 Takehara, Z. Future prospects of the lithium metal anode. *Journal of Power Sources* **68**, 82-86 (1997).
- 21 Kim, H. *et al.* Metallic anodes for next generation secondary batteries. *Chemical Society Reviews* **42**, 9011-9034 (2013).
- 22 Miao, R. R. *et al.* Novel dual-salts electrolyte solution for dendrite-free lithium-metal based rechargeable batteries with high cycle reversibility. *Journal of Power Sources* **271**, 291-297 (2014).
- 23 Lu, Y. Y., Tu, Z. Y. & Archer, L. A. Stable lithium electrodeposition in liquid and nanoporous solid electrolytes. *Nature Materials* **13**, 961-969 (2014).
- 24 Qian, J. F. *et al.* High rate and stable cycling of lithium metal anode. *Nature Communications* **6** (2015).

- 25 Ding, F. *et al.* Dendrite-Free Lithium Deposition via Self-Healing Electrostatic Shield Mechanism. *Journal of the American Chemical Society* **135**, 4450-4456 (2013).
- 26 Cheng, X. B. *et al.* A Review of Solid Electrolyte Interphases on Lithium Metal Anode. *Adv Sci* **3** (2016).
- 27 Thangadurai, V., Narayanan, S. & Pinzaru, D. Garnet-type solid-state fast Li ion conductors for Li batteries: critical review. *Chem Soc Rev* **43**, 4714-4727 (2014).
- 28 Ishiguro, K. *et al.* Stability of Nb-Doped Cubic $\text{Li}_7\text{La}_3\text{Zr}_2\text{O}_{12}$ with Lithium Metal. *Journal of the Electrochemical Society* **160**, A1690-A1693 (2013).
- 29 Zhamu, A. *et al.* Reviving rechargeable lithium metal batteries: enabling next-generation high-energy and high-power cells. *Energy & Environmental Science* **5**, 5701-5707 (2012).
- 30 Yang, C.-P., Yin, Y.-X., Zhang, S.-F., Li, N.-W. & Guo, Y.-G. Accommodating lithium into 3D current collectors with a submicron skeleton towards long-life lithium metal anodes. *Nature communications* **6** (2015).
- 31 Lin, D. *et al.* Layered reduced graphene oxide with nanoscale interlayer gaps as a stable host for lithium metal anodes. *Nature nanotechnology* (2016).
- 32 Liu, X. H. *et al.* Ultrafast electrochemical lithiation of individual Si nanowire anodes. *Nano letters* **11**, 2251-2258 (2011).
- 33 Liu, X. H. *et al.* Anisotropic swelling and fracture of silicon nanowires during lithiation. *Nano letters* **11**, 3312-3318 (2011).
- 34 Gu, M. *et al.* In situ TEM study of lithiation behavior of silicon nanoparticles attached to and embedded in a carbon matrix. *Acs Nano* **6**, 8439-8447 (2012).
- 35 Liu, X. H. *et al.* In situ atomic-scale imaging of electrochemical lithiation in silicon. *Nature nanotechnology* **7**, 749-756 (2012).
- 36 Liu, X. H. *et al.* Size-dependent fracture of silicon nanoparticles during lithiation. *Acs Nano* **6**, 1522-1531 (2012).
- 37 McDowell, M. T., Lee, S. W., Wang, C., Nix, W. D. & Cui, Y. Studying the kinetics of crystalline silicon nanoparticle lithiation with in situ transmission electron microscopy. *Advanced Materials* **24**, 6034-6041 (2012).
- 38 Gu, M. *et al.* Demonstration of an electrochemical liquid cell for operando transmission electron microscopy observation of the lithiation/delithiation behavior of Si nanowire battery anodes. *Nano letters* **13**, 6106-6112 (2013).

- 39 McDowell, M. T., Lee, S. W., Nix, W. D. & Cui, Y. 25th Anniversary Article: Understanding the Lithiation of Silicon and Other Alloying Anodes for Lithium-Ion Batteries. *Advanced Materials* **25**, 4966-4985 (2013).
- 40 Ogata, K. *et al.* Revealing lithium–silicide phase transformations in nano-structured silicon-based lithium ion batteries via in situ NMR spectroscopy. *Nature communications* **5** (2014).
- 41 Bordes, A. *et al.* Investigation of lithium insertion mechanisms of a thin-film Si electrode by coupling time-of-flight secondary-ion mass spectrometry, X-ray photoelectron spectroscopy, and focused-ion-beam/SEM. *ACS applied materials & interfaces* **7**, 27853-27862 (2015).
- 42 Yang, J., Kraytsberg, A. & Ein-Eli, Y. In-situ Raman spectroscopy mapping of Si based anode material lithiation. *Journal of Power Sources* **282**, 294-298 (2015).
- 43 Zeng, Z. *et al.* In situ measurement of lithiation-induced stress in silicon nanoparticles using micro-Raman spectroscopy. *Nano Energy* **22**, 105-110 (2016).
- 44 Bordes, A. *et al.* Multiscale investigation of silicon anode Li insertion mechanisms by time-of-flight secondary ion mass spectrometer imaging performed on an in situ focused ion beam cross section. *Chemistry of Materials* **28**, 1566-1573 (2016).
- 45 Radvanyi, E. *et al.* Study of lithiation mechanisms in silicon electrodes by Auger Electron Spectroscopy. *Journal of Materials Chemistry A* **1**, 4956-4965 (2013).
- 46 McDowell, M. T. *et al.* In situ TEM of two-phase lithiation of amorphous silicon nanospheres. *Nano letters* **13**, 758-764 (2013).
- 47 Wang, J. W. *et al.* Two-phase electrochemical lithiation in amorphous silicon. *Nano letters* **13**, 709-715 (2013).
- 48 Beaulieu, L., Hatchard, T., Bonakdarpour, A., Fleischauer, M. & Dahn, J. Reaction of Li with alloy thin films studied by in situ AFM. *Journal of The Electrochemical Society* **150**, A1457-A1464 (2003).
- 49 Ghassemi, H., Au, M., Chen, N., Heiden, P. A. & Yassar, R. S. In situ electrochemical lithiation/delithiation observation of individual amorphous Si nanorods. *ACS nano* **5**, 7805-7811 (2011).
- 50 Huang, S. & Zhu, T. Atomistic mechanisms of lithium insertion in amorphous silicon. *Journal of Power Sources* **196**, 3664-3668 (2011).

- 51 Jerliu, B. *et al.* Volume Expansion during Lithiation of Amorphous Silicon Thin Film Electrodes Studied by In-Operando Neutron Reflectometry. *The Journal of Physical Chemistry C* **118**, 9395-9399 (2014).
- 52 Cui, Z., Gao, F. & Qu, J. A finite deformation stress-dependent chemical potential and its applications to lithium ion batteries. *Journal of the Mechanics and Physics of Solids* **60**, 1280-1295 (2012).
- 53 An, Y. & Jiang, H. A finite element simulation on transient large deformation and mass diffusion in electrodes for lithium ion batteries. *Modelling and Simulation in Materials Science and Engineering* **21**, 074007 (2013).
- 54 Cui, Z., Gao, F. & Qu, J. Interface-reaction controlled diffusion in binary solids with applications to lithiation of silicon in lithium-ion batteries. *Journal of the Mechanics and Physics of Solids* **61**, 293-310 (2013).
- 55 Duan, Z., Zhang, J., An, Y. & Jiang, H. Simulation of the transient behavior of gels based on an analogy between diffusion and heat transfer. *Journal of Applied Mechanics* **80**, 041017 (2013).
- 56 Ye, J. *et al.* Enhanced lithiation and fracture behavior of silicon mesoscale pillars via atomic layer coatings and geometry design. *Journal of Power Sources* **248**, 447-456 (2014).
- 57 An, Y. *et al.* Mitigating mechanical failure of crystalline silicon electrodes for lithium batteries by morphological design. *Physical Chemistry Chemical Physics* **17**, 17718-17728 (2015).
- 58 Hertzberg, B., Benson, J. & Yushin, G. Ex-situ depth-sensing indentation measurements of electrochemically produced Si-Li alloy films. *Electrochemistry Communications* **13**, 818-821 (2011).
- 59 Berla, L. A., Lee, S. W., Cui, Y. & Nix, W. D. Mechanical behavior of electrochemically lithiated silicon. *Journal of Power Sources* **273**, 41-51 (2015).
- 60 Pharr, M., Zhao, K., Wang, X., Suo, Z. & Vlassak, J. J. Kinetics of initial lithiation of crystalline silicon electrodes of lithium-ion batteries. *Nano letters* **12**, 5039-5047 (2012).
- 61 Li, J. & Dahn, J. An in situ X-ray diffraction study of the reaction of Li with crystalline Si. *Journal of The Electrochemical Society* **154**, A156-A161 (2007).

- 62 Sethuraman, V. A., Chon, M. J., Shimshak, M., Van Winkle, N. & Guduru, P. R. In situ measurement of biaxial modulus of Si anode for Li-ion batteries. *Electrochemistry Communications* **12**, 1614-1617 (2010).
- 63 Ratchford, J. *et al.* Young's modulus of polycrystalline Li₂₂Si₅. *Journal of Power Sources* **196**, 7747-7749 (2011).
- 64 Ratchford, J., Crawford, B., Wolfenstine, J., Allen, J. & Lundgren, C. Young's modulus of polycrystalline Li₁₂Si₇ using nanoindentation testing. *Journal of Power Sources* **211**, 1-3 (2012).
- 65 Shenoy, V., Johari, P. & Qi, Y. Elastic softening of amorphous and crystalline Li-Si phases with increasing Li concentration: a first-principles study. *Journal of Power Sources* **195**, 6825-6830 (2010).
- 66 Johari, P., Qi, Y. & Shenoy, V. B. The mixing mechanism during lithiation of Si negative electrode in Li-ion batteries: an ab initio molecular dynamics study. *Nano letters* **11**, 5494-5500 (2011).
- 67 Kim, H., Chou, C.-Y., Ekerdt, J. G. & Hwang, G. S. Structure and properties of Li-Si alloys: a first-principles study. *The Journal of Physical Chemistry C* **115**, 2514-2521 (2011).
- 68 Tasaki, K. *et al.* Solubility of lithium salts formed on the lithium-ion battery negative electrode surface in organic solvents. *Journal of The Electrochemical Society* **156**, A1019-A1027 (2009).
- 69 Singh, S. S. *et al.* 3D microstructural characterization and mechanical properties of constituent particles in Al 7075 alloys using X-ray synchrotron tomography and nanoindentation. *Journal of Alloys and Compounds* **602**, 163-174 (2014).
- 70 Powell, C., Hercules, D. & Czanderna, A. in *Ion Spectroscopies for Surface Analysis* 417-437 (Springer, 1991).
- 71 Stournara, M. E. *et al.* Li segregation induces structure and strength changes at the amorphous Si/Cu interface. *Nano letters* **13**, 4759-4768 (2013).
- 72 Whittingham, M. S. History, evolution, and future status of energy storage. *Proceedings of the IEEE* **100**, 1518-1534 (2012).
- 73 Arora, P., Doyle, M. & White, R. E. Mathematical Modeling of the Lithium Deposition Overcharge Reaction in Lithium-Ion Batteries Using Carbon-Based Negative Electrodes. *Journal of The Electrochemical Society* **146**, 3543-3553 (1999).

- 74 Ohta, N. *et al.* Enhancement of the High-Rate Capability of Solid-State Lithium Batteries by Nanoscale Interfacial Modification. *Advanced Materials* **18**, 2226-2229 (2006).
- 75 Goodenough, J. B. & Kim, Y. Challenges for rechargeable Li batteries†. *Chemistry of Materials* **22**, 587-603 (2009).
- 76 Cui, Z., Gao, F. & Qu, J. Two-phase versus two-stage versus multi-phase lithiation kinetics in silicon. *Applied Physics Letters* **103**, 143901 (2013).
- 77 Fang, T.-H. & Chang, W.-J. Nanomechanical properties of copper thin films on different substrates using the nanoindentation technique. *Microelectronic engineering* **65**, 231-238 (2003).
- 78 Beegan, D., Chowdhury, S. & Laugier, M. A nanoindentation study of copper films on oxidised silicon substrates. *Surface and Coatings Technology* **176**, 124-130 (2003).
- 79 Fischer, A. C. (Springer-Verlag, New York, 2004).
- 80 Obrovac, M. & Christensen, L. Structural changes in silicon anodes during lithium insertion/extraction. *Electrochemical and Solid-State Letters* **7**, A93-A96 (2004).
- 81 Gu, M. *et al.* Electronic Origin for the Phase Transition from Amorphous Li_xSi to Crystalline Li₁₅Si₄. *ACS nano* **7**, 6303-6309 (2013).
- 82 Key, B., Morcrette, M., Tarascon, J.-M. & Grey, C. P. Pair distribution function analysis and solid state NMR studies of silicon electrodes for lithium ion batteries: understanding the (de) lithiation mechanisms. *Journal of the American Chemical Society* **133**, 503-512 (2010).
- 83 Zhamu, A. *et al.* Reviving rechargeable lithium metal batteries: enabling next-generation high-energy and high-power cells. *Energy & Environmental Science* **5**, 5701-5707 (2012).
- 84 Seh, Z. W., Sun, Y., Zhang, Q. & Cui, Y. Designing high-energy lithium–sulfur batteries. *Chemical Society Reviews* (2016).
- 85 Dong, S. *et al.* Insight into enhanced cycling performance of Li–O₂ batteries based on binary CoSe₂/CoO nanocomposite electrodes. *The journal of physical chemistry letters* **5**, 615-621 (2014).
- 86 Kim, S. *et al.* All-water-based electron-beam lithography using silk as a resist. *Nat Nano* **9**, 306-310 (2014).

- 87 Safari, M., Adams, B. & Nazar, L. Kinetics of oxygen reduction in aprotic Li–O₂ cells: a model-based study. *The journal of physical chemistry letters* **5**, 3486-3491 (2014).
- 88 Li, Z., Huang, J., Liaw, B. Y., Metzler, V. & Zhang, J. A review of lithium deposition in lithium-ion and lithium metal secondary batteries. *Journal of power sources* **254**, 168-182 (2014).
- 89 Yamaki, J.-i. *et al.* A consideration of the morphology of electrochemically deposited lithium in an organic electrolyte. *Journal of Power Sources* **74**, 219-227 (1998).
- 90 Aurbach, D. & Zaban, A. Impedance spectroscopy of lithium electrodes: Part 1. General behavior in propylene carbonate solutions and the correlation to surface chemistry and cycling efficiency. *Journal of Electroanalytical Chemistry* **348**, 155-179 (1993).
- 91 Hirai, T., Yoshimatsu, I. & Yamaki, J. i. Effect of additives on lithium cycling efficiency. *Journal of The Electrochemical Society* **141**, 2300-2305 (1994).
- 92 Ishikawa, M., Yoshitake, S., Morita, M. & Matsuda, Y. In situ scanning vibrating electrode technique for the characterization of interface between lithium electrode and electrolytes containing additives. *Journal of The Electrochemical Society* **141**, L159-L161 (1994).
- 93 Che, G., Lakshmi, B. B., Fisher, E. R. & Martin, C. R. Carbon nanotubule membranes for electrochemical energy storage and production. *Nature* **393**, 346-349 (1998).
- 94 Vaughey, J., Fransson, L., Swinger, H., Edström, K. & Thackeray, M. Alternative anode materials for lithium-ion batteries: a study of Ag₃Sb. *Journal of power sources* **119**, 64-68 (2003).
- 95 Dudley, J. *et al.* Conductivity of electrolytes for rechargeable lithium batteries. *Journal of power sources* **35**, 59-82 (1991).
- 96 Matsuda, Y. Stable electrolytes for lithium batteries. *Journal of Power Sources* **20**, 19-26 (1987).
- 97 Aurbach, D., Daroux, M., Faguy, P. & Yeager, E. Identification of surface films formed on lithium in propylene carbonate solutions. *Journal of The Electrochemical Society* **134**, 1611-1620 (1987).

- 98 Aurbach, D., Markovsky, B., Shechter, A., Ein-Eli, Y. & Cohen, H. A Comparative Study of Synthetic Graphite and Li Electrodes in Electrolyte Solutions Based on Ethylene Carbonate-Dimethyl Carbonate Mixtures. *Journal of The Electrochemical Society* **143**, 3809-3820 (1996).
- 99 Aurbach, D. *et al.* Recent studies of the lithium-liquid electrolyte interface Electrochemical, morphological and spectral studies of a few important systems. *Journal of Power Sources* **54**, 76-84 (1995).
- 100 Schechter, A., Aurbach, D. & Cohen, H. X-ray Photoelectron spectroscopy study of surface films formed on Li electrodes freshly prepared in Alkyl carbonate solutions. *Langmuir* **15**, 3334-3342 (1999).
- 101 Xu, W. *et al.* Lithium metal anodes for rechargeable batteries. *Energy & Environmental Science* **7**, 513-537 (2014).
- 102 Murugan, R., Thangadurai, V. & Weppner, W. Fast Lithium Ion Conduction in Garnet-Type $\text{Li}_7\text{La}_3\text{Zr}_2\text{O}_{12}$. *Angewandte Chemie International Edition* **46**, 7778-7781 (2007).
- 103 Kim, K. H. *et al.* Characterization of the interface between LiCoO_2 and $\text{Li}_7\text{La}_3\text{Zr}_2\text{O}_{12}$ in an all-solid-state rechargeable lithium battery. *Journal of Power Sources* **196**, 764-767 (2011).
- 104 Gireaud, L., Grugeon, S., Laruelle, S., Yrieix, B. & Tarascon, J.-M. Lithium metal stripping/plating mechanisms studies: A metallurgical approach. *Electrochemistry communications* **8**, 1639-1649 (2006).
- 105 Mayers, M. Z., Kaminski, J. W. & Miller III, T. F. Suppression of dendrite formation via pulse charging in rechargeable lithium metal batteries. *The Journal of Physical Chemistry C* **116**, 26214-26221 (2012).
- 106 Yan, K. *et al.* Ultrathin two-dimensional atomic crystals as stable interfacial layer for improvement of lithium metal anode. *Nano letters* **14**, 6016-6022 (2014).
- 107 Zheng, G. *et al.* Interconnected hollow carbon nanospheres for stable lithium metal anodes. *Nature nanotechnology* **9**, 618-623 (2014).
- 108 Lee, H., Lee, D. J., Kim, Y.-J., Park, J.-K. & Kim, H.-T. A simple composite protective layer coating that enhances the cycling stability of lithium metal batteries. *Journal of Power Sources* **284**, 103-108 (2015).
- 109 Chu, S. & Cui, Y. Selective deposition and stable encapsulation of lithium through heterogeneous seeded growth. (2016).

- 110 Liu, Y. *et al.* Lithium-coated polymeric matrix as a minimum volume-change and dendrite-free lithium metal anode. *Nature communications* **7** (2016).
- 111 Lu, L.-L. *et al.* Free-Standing Copper Nanowire Network Current Collector for Improving Lithium Anode Performance. *Nano letters* (2016).
- 112 Yun, Q. *et al.* Chemical Dealloying Derived 3D Porous Current Collector for Li Metal Anodes. *Advanced Materials* (2016).
- 113 Chason, E., Jadhav, N., Pei, F., Buchovecky, E. & Bower, A. Growth of whiskers from Sn surfaces: Driving forces and growth mechanisms. *Progress in Surface Science* **88**, 103-131, doi:10.1016/j.progsurf.2013.02.002 (2013).
- 114 Chason, E. *et al.* Understanding Residual Stress in Electrodeposited Cu Thin Films. *Journal of the Electrochemical Society* **160**, D3285-D3289 (2013).
- 115 Shin, J. W. & Chason, E. Compressive stress generation in sn thin films and the role of grain boundary diffusion. *Phys Rev Lett* **103**, 056102, doi:10.1103/PhysRevLett.103.056102 (2009).
- 116 Yamaki, J. *et al.* A consideration of the morphology of electrochemically deposited lithium in an organic electrolyte. *Journal of Power Sources* **74**, 219-227 (1998).
- 117 Li, W. Y. *et al.* The synergetic effect of lithium polysulfide and lithium nitrate to prevent lithium dendrite growth. *Nature Communications* **6** (2015).
- 118 Bai, P., Li, J., Brushett, F. R. & Bazant, M. Z. Transition of lithium growth mechanisms in liquid electrolytes. *Energy & Environmental Science* **9**, 3221-3229 (2016).
- 119 Bowden, N., Brittain, S., Evans, A. G., Hutchinson, J. W. & Whitesides, G. M. Spontaneous formation of ordered structures in thin films of metals supported on an elastomeric polymer. *Nature* **393**, 146-149 (1998).
- 120 Khang, D. Y., Jiang, H. Q., Huang, Y. & Rogers, J. A. A stretchable form of single-crystal silicon for high-performance electronics on rubber substrates. *Science* **311**, 208-212 (2006).
- 121 Huang, Z. Y., Hong, W. & Suo, Z. Nonlinear analyses of wrinkles in a film bonded to a compliant substrate. *J. Mech. Phys. Solids* **53**, 2101-2118 (2005).
- 122 Song, J. *et al.* An Analytical Study of Two-Dimensional Buckling of Thin Films on Compliant Substrates. *Journal of Applied Physics* **103**, 014303 (2008).

- 123 Wang, Z., Volinsky, A. A. & Gallant, N. D. Crosslinking effect on polydimethylsiloxane elastic modulus measured by custom-built compression instrument. *Journal of Applied Polymer Science* **131** (2014).
- 124 James, A. M. & Lord, M. P. *Macmillan's chemical and physical data*. (Macmillan London, 1992).
- 125 Xu, C., Ahmad, Z., Aryanfar, A., Viswanathan, V. & Greer, J. R. Enhanced strength and temperature dependence of mechanical properties of Li at small scales and its implications for Li metal anodes. *Proc Natl Acad Sci U S A* **114**, 57-61, doi:10.1073/pnas.1615733114 (2017).
- 126 Yu, C. *et al.* Silicon Thin Films as Anodes for High-Performance Lithium-Ion Batteries with Effective Stress Relaxation. *Advanced Energy Materials* **2**, 68-73 (2012).
- 127 Jiang, H. *et al.* Finite Deformation Mechanics in Buckled Thin Films on Compliant Supports. *Proceedings of the National Academy of Sciences of the United States of America* **104**, 15607-15612 (2007).
- 128 Steiger, J., Kramer, D. & Monig, R. Mechanisms of dendritic growth investigated by in situ light microscopy during electrodeposition and dissolution of lithium. *Journal of Power Sources* **261**, 112-119 (2014).
- 129 Sand, H. J. S. On the concentration at the electrodes in a solution, with special reference to the liberation of hydrogen by electrolysis of a mixture of copper sulphate and sulphuric acid. *Philos Mag* **1**, 45-79 (1901).
- 130 *Mitigating Tin Whisker Risks: Theory and Practice*. (Wiley, 2016).
- 131 Sarobol, P., Blendell, J. E. & Handwerker, C. A. Whisker and hillock growth via coupled localized Coble creep, grain boundary sliding, and shear induced grain boundary migration. *Acta Materialia* **61**, 1991-2003, doi:10.1016/j.actamat.2012.12.019 (2013).
- 132 Harry, K. J., Hallinan, D. T., Parkinson, D. Y., MacDowell, A. A. & Balsara, N. P. Detection of subsurface structures underneath dendrites formed on cycled lithium metal electrodes. *Nat Mater* **13**, 69-73, doi:10.1038/nmat3793 (2014).
- 133 Wieland, O. & Carstanjen, H. D. Measurement of the low-temperature self-diffusivity of lithium by elastic recoil detection analysis. *Defect Diffus Forum* **194-1**, 35-41 (2001).
- 134 Liu, W. *et al.* 3D Porous Sponge-Inspired Electrode for Stretchable Lithium-Ion Batteries. *Advanced Materials*, doi:10.1002/adma.201505299 (2016).

- 135 Yang, W. *et al.* Fabrication of a Hydrophilic Poly(dimethylsiloxane) Microporous Structure and Its Application to Portable Microfluidic Pump. *Japanese Journal of Applied Physics* **49**, doi:10.1143/jjap.49.06gm01 (2010).

APPENDIX A

ABAQUS SUBROUTINE FOR SI THIN FILM LITHIATION MODELING

```

SUBROUTINE UMAT(STRESS,STATEV,DDSDDE,SSE,SPD,SCD,
  1 RPL,DDSDDT,DRPLDE,DRPLDT,
  2
STRAN,DSTRAN,TIME,DTIME,TEMP,DTEMP,PRED,DPRED,CMNAME,
  3 NDI,NSHR,NTENS,NSTATV,PROPS,NPROPS,COORDS,DROT,PNEWDT,
  4 CELENT,DFGRD0,DFGRD1,NOEL,NPT,LAYER,KSPT,KSTEP,KINC)
C
C THIS SUBROUTINE IS MAINLY USED TO READ THE DEFORMATION
GRADIENT AT GAUSSIAN POINTS
C INITIALIZATION OF SOME DATA IS ALSO DONE IN THIS SUBROUTINE
C
  IMPLICIT DOUBLE PRECISION (A-H,O-Z)
  CHARACTER*80 CMNAME
  DIMENSION STRESS(NTENS),STATEV(NSTATV),
  1 DDSDDE(NTENS,NTENS),DDSDDT(NTENS),DRPLDE(NTENS),
  2 STRAN(NTENS),DSTRAN(NTENS),TIME(2),PRED(1),DPRED(1),
  3 PROPS(NPROPS),COORDS(3),DROT(3,3),DFGRD0(3,3),DFGRD1(3,3)
  PARAMETER (NELETOT=500)
  PARAMETER (NNODETOT=2736)
  COMMON /RRRR/
DGARRAY(NELETOT*27*9),DGARRAY1(NELETOT*27*9),
  &XYZGP(NELETOT*27*3),VECTORNORM(NELETOT*4*3),
  &SFSFI(20,20),SFSFI0(8,8)
  COMMON /NNNN/
NUMNODE(NELETOT*4*1),ICALLUMATHT,KINCOLD,ICALLUMAT
  DIMENSION NODE(20),DG(3,3)
  PARAMETER (POS=DSQRT(15.D0)/5.D0)

C !WE NEED TO SET THE PROPER TOTAL ELEMENT NUMBER N IN ARRAY
C  VECTORNORM(N*4*3),NUMNODE(N*4*1),XYZNODE(N*20*3),
C  ACCORDINGLY THROUGHOUT THIS CODE!

CCCCCCCCCCCCCCCCCCCCCCCCCCCCCCCCCCCC
C DGARRAY---DEFORMATION GRADIENT COMPONENTS AT GAUSSIAN
POINTS
C XYZGP---ORIGINAL POSITION OF ALL THE GAUSSIAN POINTS
C VECTORNORM---NORMAL VECTOR AT THE NODES OF THE SURFACE
WHERE LI DIFFUSESE IN
C XYZNODE---ORIGINAL POSITION OF ALL THE NODES
C XI1,XI2,XI3---NATURAL COORDINATES OF GAUSSIAN POINTS
C SF---SHAP FUNCTION AT ALL THE 27 GAUSSIAN POINTS
C SFSF---MATRIX FORMED BY 20 GAUSSIAN POINTS OUT OF THE 27 ONES
C SFSFI---INVERSE OF THE MATRIX SFSF, WHICH IS USED TO
EXTRAPOLATE VARIABLES FROM 27 GAUSSIAN POINTS TO 20 NODES
CCCCCCCCCCCCCCCCCCCCCCCCCCCCCCCCCCCC

```

```

NE=NOEL
NP=NPT

DGARRAY1((NE-1)*243+(NP-1)*9+1)=DFGRD0(1,1)
DGARRAY1((NE-1)*243+(NP-1)*9+2)=DFGRD0(1,2)
DGARRAY1((NE-1)*243+(NP-1)*9+3)=DFGRD0(1,3)
DGARRAY1((NE-1)*243+(NP-1)*9+4)=DFGRD0(2,1)
DGARRAY1((NE-1)*243+(NP-1)*9+5)=DFGRD0(2,2)
DGARRAY1((NE-1)*243+(NP-1)*9+6)=DFGRD0(2,3)
DGARRAY1((NE-1)*243+(NP-1)*9+7)=DFGRD0(3,1)
DGARRAY1((NE-1)*243+(NP-1)*9+8)=DFGRD0(3,2)
DGARRAY1((NE-1)*243+(NP-1)*9+9)=DFGRD0(3,3)
C READ DEFORMATION GRADIENT

IF(KINC.EQ.0) ICALLUMATHT=0
IF(KINC.EQ.0) KINCOLD=0
IF(KINC.EQ.1.AND.KSTEP.NE.1) KINCOLD=0
IF(KINC-KINCOLD.EQ.1) THEN
    ICALLUMATHT=0
    ICALLUMAT=0
    KINCOLD=KINC
ENDIF

IF(ICALLUMATHT.EQ.NELETOT*27.AND.ICALLUMAT.EQ.NELETOT*27)
THEN
    DGARRAY=DGARRAY1
ENDIF
ICALLUMAT=ICALLUMAT+1

C INITIALIZE SOME DATA
IF(KINC.EQ.0) THEN
    XYZGP((NOEL-1)*81+(NPT-1)*3+1)=COORDS(1)
    XYZGP((NOEL-1)*81+(NPT-1)*3+2)=COORDS(2)
    XYZGP((NOEL-1)*81+(NPT-1)*3+3)=COORDS(3)

    IF(ICALLUMAT.EQ.NELETOT*27) THEN
        DGARRAY=0.D0
        DO NE=1,NELETOT
            DO NP=1,27
                DGARRAY((NE-1)*243+(NP-1)*9+1)=1.D0
                DGARRAY((NE-1)*243+(NP-1)*9+5)=1.D0
                DGARRAY((NE-1)*243+(NP-1)*9+9)=1.D0
            ENDDO
        ENDDO
    ENDDO
ENDIF

```

C INITIALIZE DGARRAY

```

DO NE=1,NELETOT
  DO NP=1,4
    VECTORNORM((NE-1)*12+(NP-1)*3+1)=0.D0
    VECTORNORM((NE-1)*12+(NP-1)*3+2)=0.D0
    VECTORNORM((NE-1)*12+(NP-1)*3+3)=1.D0
  ENDDO
ENDDO

```

C SET VECTORNORM ACCORDING TO THE SPECIFIC B.C.

```

C1=-(2.D0*POS**4.D0+3.D0*POS**3.D0-3.D0*POS**2.D0-
7.D0*POS-3.D0)
&      /(8.D0*POS**4.D0)
C2= (POS**4.D0+2.D0*POS**3.D0-2.D0*POS-1.D0)
&      /(4.D0*POS**4.D0)
C3=-(2.D0*POS**4.D0+POS**3.D0-3.D0*POS**2.D0-POS+1.D0)
&      /(8.D0*POS**4.D0)
C4= (POS**4.D0-2.D0*POS**2.D0+1.D0)
&      /(4.D0*POS**4.D0)
C5=-(2.D0*POS**4.D0-POS**3.D0-3.D0*POS**2.D0+POS+1.D0)
&      /(8.D0*POS**4.D0)
C6= (POS**4.D0-2.D0*POS**3.D0+2.D0*POS-1.D0)
&      /(4.D0*POS**4.D0)
C7=-(2.D0*POS**4.D0-3.D0*POS**3.D0-
3.D0*POS**2.D0+7.D0*POS-3.D0)
&      /(8.D0*POS**4.D0)

C8=-(POS**3.D0+POS**2.D0-POS-1.D0)
&      /(4.D0*POS**3.D0)
C9= (POS**2.D0+2.D0*POS+1.D0)
&      /(4.D0*POS**2.D0)
C10= (POS**3.D0+POS**2.D0-POS-1.D0)
&      /(4.D0*POS**3.D0)
C11=-(POS**2.D0-1.D0)
&      /(4.D0*POS**2.D0)
C12= (POS**2.D0-1.D0)
&      /(4.D0*POS**2.D0)
C13= (POS**3.D0-POS**2.D0-POS+1.D0)
&      /(4.D0*POS**3.D0)
C14=-(POS**3.D0-POS**2.D0-POS+1.D0)
&      /(4.D0*POS**3.D0)
C15= (POS**2.D0-2.D0*POS+1.D0)
&      /(4.D0*POS**2.D0)

```

SFSFI(1,1)= C1
 SFSFI(1,2)= C2
 SFSFI(1,3)= C3
 SFSFI(1,4)= C2
 SFSFI(1,5)= C4
 SFSFI(1,6)= C3
 SFSFI(1,7)= C4
 SFSFI(1,8)= C5
 SFSFI(1,9)= C2
 SFSFI(1,10)= C4
 SFSFI(1,11)= C4
 SFSFI(1,12)= C6
 SFSFI(1,13)= C3
 SFSFI(1,14)= C4
 SFSFI(1,15)= C5
 SFSFI(1,16)= C4
 SFSFI(1,17)= C6
 SFSFI(1,18)= C5
 SFSFI(1,19)= C6
 SFSFI(1,20)= C7

SFSFI(2,1)= C3
 SFSFI(2,2)= C2
 SFSFI(2,3)= C1
 SFSFI(2,4)= C4
 SFSFI(2,5)= C2
 SFSFI(2,6)= C5
 SFSFI(2,7)= C4
 SFSFI(2,8)= C3
 SFSFI(2,9)= C4
 SFSFI(2,10)= C2
 SFSFI(2,11)= C6
 SFSFI(2,12)= C4
 SFSFI(2,13)= C5
 SFSFI(2,14)= C4
 SFSFI(2,15)= C3
 SFSFI(2,16)= C6
 SFSFI(2,17)= C4
 SFSFI(2,18)= C7
 SFSFI(2,19)= C6
 SFSFI(2,20)= C5

SFSFI(3,1)= C5
 SFSFI(3,2)= C4

$SFSFI(3,3) = C3$
 $SFSFI(3,4) = C4$
 $SFSFI(3,5) = C2$
 $SFSFI(3,6) = C3$
 $SFSFI(3,7) = C2$
 $SFSFI(3,8) = C1$
 $SFSFI(3,9) = C6$
 $SFSFI(3,10) = C4$
 $SFSFI(3,11) = C4$
 $SFSFI(3,12) = C2$
 $SFSFI(3,13) = C7$
 $SFSFI(3,14) = C6$
 $SFSFI(3,15) = C5$
 $SFSFI(3,16) = C6$
 $SFSFI(3,17) = C4$
 $SFSFI(3,18) = C5$
 $SFSFI(3,19) = C4$
 $SFSFI(3,20) = C3$

$SFSFI(4,1) = C3$
 $SFSFI(4,2) = C4$
 $SFSFI(4,3) = C5$
 $SFSFI(4,4) = C2$
 $SFSFI(4,5) = C4$
 $SFSFI(4,6) = C1$
 $SFSFI(4,7) = C2$
 $SFSFI(4,8) = C3$
 $SFSFI(4,9) = C4$
 $SFSFI(4,10) = C6$
 $SFSFI(4,11) = C2$
 $SFSFI(4,12) = C4$
 $SFSFI(4,13) = C5$
 $SFSFI(4,14) = C6$
 $SFSFI(4,15) = C7$
 $SFSFI(4,16) = C4$
 $SFSFI(4,17) = C6$
 $SFSFI(4,18) = C3$
 $SFSFI(4,19) = C4$
 $SFSFI(4,20) = C5$

$SFSFI(5,1) = C3$
 $SFSFI(5,2) = C4$
 $SFSFI(5,3) = C5$
 $SFSFI(5,4) = C4$
 $SFSFI(5,5) = C6$

SFSFI(5,6)= C5
SFSFI(5,7)= C6
SFSFI(5,8)= C7
SFSFI(5,9)= C2
SFSFI(5,10)= C4
SFSFI(5,11)= C4
SFSFI(5,12)= C6
SFSFI(5,13)= C1
SFSFI(5,14)= C2
SFSFI(5,15)= C3
SFSFI(5,16)= C2
SFSFI(5,17)= C4
SFSFI(5,18)= C3
SFSFI(5,19)= C4
SFSFI(5,20)= C5

SFSFI(6,1)= C5
SFSFI(6,2)= C4
SFSFI(6,3)= C3
SFSFI(6,4)= C6
SFSFI(6,5)= C4
SFSFI(6,6)= C7
SFSFI(6,7)= C6
SFSFI(6,8)= C5
SFSFI(6,9)= C4
SFSFI(6,10)= C2
SFSFI(6,11)= C6
SFSFI(6,12)= C4
SFSFI(6,13)= C3
SFSFI(6,14)= C2
SFSFI(6,15)= C1
SFSFI(6,16)= C4
SFSFI(6,17)= C2
SFSFI(6,18)= C5
SFSFI(6,19)= C4
SFSFI(6,20)= C3

SFSFI(7,1)= C7
SFSFI(7,2)= C6
SFSFI(7,3)= C5
SFSFI(7,4)= C6
SFSFI(7,5)= C4
SFSFI(7,6)= C5
SFSFI(7,7)= C4
SFSFI(7,8)= C3

SFSFI(7,9)= C6
 SFSFI(7,10)= C4
 SFSFI(7,11)= C4
 SFSFI(7,12)= C2
 SFSFI(7,13)= C5
 SFSFI(7,14)= C4
 SFSFI(7,15)= C3
 SFSFI(7,16)= C4
 SFSFI(7,17)= C2
 SFSFI(7,18)= C3
 SFSFI(7,19)= C2
 SFSFI(7,20)= C1

SFSFI(8,1)= C5
 SFSFI(8,2)= C6
 SFSFI(8,3)= C7
 SFSFI(8,4)= C4
 SFSFI(8,5)= C6
 SFSFI(8,6)= C3
 SFSFI(8,7)= C4
 SFSFI(8,8)= C5
 SFSFI(8,9)= C4
 SFSFI(8,10)= C6
 SFSFI(8,11)= C2
 SFSFI(8,12)= C4
 SFSFI(8,13)= C3
 SFSFI(8,14)= C4
 SFSFI(8,15)= C5
 SFSFI(8,16)= C2
 SFSFI(8,17)= C4
 SFSFI(8,18)= C1
 SFSFI(8,19)= C2
 SFSFI(8,20)= C3

SFSFI(9,1)= C8
 SFSFI(9,2)= C9
 SFSFI(9,3)= C8
 SFSFI(9,4)= C10
 SFSFI(9,5)= C10
 SFSFI(9,6)= C11
 SFSFI(9,7)= C12
 SFSFI(9,8)= C11
 SFSFI(9,9)= C10
 SFSFI(9,10)= C10
 SFSFI(9,11)= C13

SFSFI(9,12)= C13
SFSFI(9,13)= C11
SFSFI(9,14)= C12
SFSFI(9,15)= C11
SFSFI(9,16)= C13
SFSFI(9,17)= C13
SFSFI(9,18)= C14
SFSFI(9,19)= C15
SFSFI(9,20)= C14

SFSFI(10,1)= C11
SFSFI(10,2)= C10
SFSFI(10,3)= C8
SFSFI(10,4)= C12
SFSFI(10,5)= C9
SFSFI(10,6)= C11
SFSFI(10,7)= C10
SFSFI(10,8)= C8
SFSFI(10,9)= C13
SFSFI(10,10)= C10
SFSFI(10,11)= C13
SFSFI(10,12)= C10
SFSFI(10,13)= C14
SFSFI(10,14)= C13
SFSFI(10,15)= C11
SFSFI(10,16)= C15
SFSFI(10,17)= C12
SFSFI(10,18)= C14
SFSFI(10,19)= C13
SFSFI(10,20)= C11

SFSFI(11,1)= C11
SFSFI(11,2)= C12
SFSFI(11,3)= C11
SFSFI(11,4)= C10
SFSFI(11,5)= C10
SFSFI(11,6)= C8
SFSFI(11,7)= C9
SFSFI(11,8)= C8
SFSFI(11,9)= C13
SFSFI(11,10)= C13
SFSFI(11,11)= C10
SFSFI(11,12)= C10
SFSFI(11,13)= C14
SFSFI(11,14)= C15

SFSFI(11,15)= C14
SFSFI(11,16)= C13
SFSFI(11,17)= C13
SFSFI(11,18)= C11
SFSFI(11,19)= C12
SFSFI(11,20)= C11

SFSFI(12,1)= C8
SFSFI(12,2)= C10
SFSFI(12,3)= C11
SFSFI(12,4)= C9
SFSFI(12,5)= C12
SFSFI(12,6)= C8
SFSFI(12,7)= C10
SFSFI(12,8)= C11
SFSFI(12,9)= C10
SFSFI(12,10)= C13
SFSFI(12,11)= C10
SFSFI(12,12)= C13
SFSFI(12,13)= C11
SFSFI(12,14)= C13
SFSFI(12,15)= C14
SFSFI(12,16)= C12
SFSFI(12,17)= C15
SFSFI(12,18)= C11
SFSFI(12,19)= C13
SFSFI(12,20)= C14

SFSFI(13,1)= C11
SFSFI(13,2)= C12
SFSFI(13,3)= C11
SFSFI(13,4)= C13
SFSFI(13,5)= C13
SFSFI(13,6)= C14
SFSFI(13,7)= C15
SFSFI(13,8)= C14
SFSFI(13,9)= C10
SFSFI(13,10)= C10
SFSFI(13,11)= C13
SFSFI(13,12)= C13
SFSFI(13,13)= C8
SFSFI(13,14)= C9
SFSFI(13,15)= C8
SFSFI(13,16)= C10
SFSFI(13,17)= C10

SFSFI(13,18)= C11
SFSFI(13,19)= C12
SFSFI(13,20)= C11

SFSFI(14,1)= C14
SFSFI(14,2)= C13
SFSFI(14,3)= C11
SFSFI(14,4)= C15
SFSFI(14,5)= C12
SFSFI(14,6)= C14
SFSFI(14,7)= C13
SFSFI(14,8)= C11
SFSFI(14,9)= C13
SFSFI(14,10)= C10
SFSFI(14,11)= C13
SFSFI(14,12)= C10
SFSFI(14,13)= C11
SFSFI(14,14)= C10
SFSFI(14,15)= C8
SFSFI(14,16)= C12
SFSFI(14,17)= C9
SFSFI(14,18)= C11
SFSFI(14,19)= C10
SFSFI(14,20)= C8

SFSFI(15,1)= C14
SFSFI(15,2)= C15
SFSFI(15,3)= C14
SFSFI(15,4)= C13
SFSFI(15,5)= C13
SFSFI(15,6)= C11
SFSFI(15,7)= C12
SFSFI(15,8)= C11
SFSFI(15,9)= C13
SFSFI(15,10)= C13
SFSFI(15,11)= C10
SFSFI(15,12)= C10
SFSFI(15,13)= C11
SFSFI(15,14)= C12
SFSFI(15,15)= C11
SFSFI(15,16)= C10
SFSFI(15,17)= C10
SFSFI(15,18)= C8
SFSFI(15,19)= C9
SFSFI(15,20)= C8

SFSFI(16,1)= C11
 SFSFI(16,2)= C13
 SFSFI(16,3)= C14
 SFSFI(16,4)= C12
 SFSFI(16,5)= C15
 SFSFI(16,6)= C11
 SFSFI(16,7)= C13
 SFSFI(16,8)= C14
 SFSFI(16,9)= C10
 SFSFI(16,10)= C13
 SFSFI(16,11)= C10
 SFSFI(16,12)= C13
 SFSFI(16,13)= C8
 SFSFI(16,14)= C10
 SFSFI(16,15)= C11
 SFSFI(16,16)= C9
 SFSFI(16,17)= C12
 SFSFI(16,18)= C8
 SFSFI(16,19)= C10
 SFSFI(16,20)= C11

SFSFI(17,1)= C8
 SFSFI(17,2)= C10
 SFSFI(17,3)= C11
 SFSFI(17,4)= C10
 SFSFI(17,5)= C13
 SFSFI(17,6)= C11
 SFSFI(17,7)= C13
 SFSFI(17,8)= C14
 SFSFI(17,9)= C9
 SFSFI(17,10)= C12
 SFSFI(17,11)= C12
 SFSFI(17,12)= C15
 SFSFI(17,13)= C8
 SFSFI(17,14)= C10
 SFSFI(17,15)= C11
 SFSFI(17,16)= C10
 SFSFI(17,17)= C13
 SFSFI(17,18)= C11
 SFSFI(17,19)= C13
 SFSFI(17,20)= C14

SFSFI(18,1)= C11
 SFSFI(18,2)= C10

SFSFI(18,3)= C8
 SFSFI(18,4)= C13
 SFSFI(18,5)= C10
 SFSFI(18,6)= C14
 SFSFI(18,7)= C13
 SFSFI(18,8)= C11
 SFSFI(18,9)= C12
 SFSFI(18,10)= C9
 SFSFI(18,11)= C15
 SFSFI(18,12)= C12
 SFSFI(18,13)= C11
 SFSFI(18,14)= C10
 SFSFI(18,15)= C8
 SFSFI(18,16)= C13
 SFSFI(18,17)= C10
 SFSFI(18,18)= C14
 SFSFI(18,19)= C13
 SFSFI(18,20)= C11

SFSFI(19,1)= C14
 SFSFI(19,2)= C13
 SFSFI(19,3)= C11
 SFSFI(19,4)= C13
 SFSFI(19,5)= C10
 SFSFI(19,6)= C11
 SFSFI(19,7)= C10
 SFSFI(19,8)= C8
 SFSFI(19,9)= C15
 SFSFI(19,10)= C12
 SFSFI(19,11)= C12
 SFSFI(19,12)= C9
 SFSFI(19,13)= C14
 SFSFI(19,14)= C13
 SFSFI(19,15)= C11
 SFSFI(19,16)= C13
 SFSFI(19,17)= C10
 SFSFI(19,18)= C11
 SFSFI(19,19)= C10
 SFSFI(19,20)= C8

SFSFI(20,1)= C11
 SFSFI(20,2)= C13
 SFSFI(20,3)= C14
 SFSFI(20,4)= C10
 SFSFI(20,5)= C13

$SFSFI(20,6) = C8$
 $SFSFI(20,7) = C10$
 $SFSFI(20,8) = C11$
 $SFSFI(20,9) = C12$
 $SFSFI(20,10) = C15$
 $SFSFI(20,11) = C9$
 $SFSFI(20,12) = C12$
 $SFSFI(20,13) = C11$
 $SFSFI(20,14) = C13$
 $SFSFI(20,15) = C14$
 $SFSFI(20,16) = C10$
 $SFSFI(20,17) = C13$
 $SFSFI(20,18) = C8$
 $SFSFI(20,19) = C10$
 $SFSFI(20,20) = C11$

$A = (POS - 1.D0)^{**2.D0} * (POS + 1.D0) / POS^{**3.D0} / 8.D0$
 $B = (POS + 1.D0)^{**2.D0} * (POS - 1.D0) / POS^{**3.D0} / 8.D0$
 $C = (POS - 1.D0)^{**3.D0} / POS^{**3.D0} / 8.D0$
 $D = (POS + 1.D0)^{**3.D0} / POS^{**3.D0} / 8.D0$

$SFSFI0(1,1) = A$
 $SFSFI0(1,2) = B$
 $SFSFI0(1,3) = C$
 $SFSFI0(1,4) = A$
 $SFSFI0(1,5) = B$
 $SFSFI0(1,6) = D$
 $SFSFI0(1,7) = A$
 $SFSFI0(1,8) = B$

$SFSFI0(2,1) = B$
 $SFSFI0(2,2) = D$
 $SFSFI0(2,3) = A$
 $SFSFI0(2,4) = B$
 $SFSFI0(2,5) = A$
 $SFSFI0(2,6) = B$
 $SFSFI0(2,7) = C$
 $SFSFI0(2,8) = A$

$SFSFI0(3,1) = D$
 $SFSFI0(3,2) = B$
 $SFSFI0(3,3) = B$
 $SFSFI0(3,4) = A$
 $SFSFI0(3,5) = B$
 $SFSFI0(3,6) = A$

SFSFI0(3,7)=A
SFSFI0(3,8)=C

SFSFI0(4,1)=B
SFSFI0(4,2)=A
SFSFI0(4,3)=A
SFSFI0(4,4)=C
SFSFI0(4,5)=D
SFSFI0(4,6)=B
SFSFI0(4,7)=B
SFSFI0(4,8)=A

SFSFI0(5,1)=C
SFSFI0(5,2)=A
SFSFI0(5,3)=A
SFSFI0(5,4)=B
SFSFI0(5,5)=A
SFSFI0(5,6)=B
SFSFI0(5,7)=B
SFSFI0(5,8)=D

SFSFI0(6,1)=A
SFSFI0(6,2)=B
SFSFI0(6,3)=B
SFSFI0(6,4)=D
SFSFI0(6,5)=C
SFSFI0(6,6)=A
SFSFI0(6,7)=A
SFSFI0(6,8)=B

SFSFI0(7,1)=B
SFSFI0(7,2)=A
SFSFI0(7,3)=D
SFSFI0(7,4)=B
SFSFI0(7,5)=A
SFSFI0(7,6)=C
SFSFI0(7,7)=B
SFSFI0(7,8)=A

SFSFI0(8,1)=A
SFSFI0(8,2)=C
SFSFI0(8,3)=B
SFSFI0(8,4)=A
SFSFI0(8,5)=B
SFSFI0(8,6)=A

```

        SFSFI0(8,7)=D
        SFSFI0(8,8)=B
    ENDIF
ENDIF

RETURN
END
*****
*****

SUBROUTINE
UMATHT(U,DUDT,DUDG,FLUX,DFDT,DFDG,STATEV,TEMP,

&DTEMP,DTEMDX,TIME,DTIME,PRED,DPRED,CMNAME,NTGRD,NSTATV,
    &PROPS,NPROPS,COORDS,PNEWDT,NOEL,NPT,LAYER,KSPT,KSTEP,KINC)
C
C THIS SUBROUTINE IS USED TO DEFINE THE EXPRESSION FOR MASS FLUX
C

    INCLUDE 'ABA_PARAM.INC'

    CHARACTER*80 CMNAME
    DIMENSION DUDG(NTGRD),FLUX(NTGRD),DFDT(NTGRD),
    &DFDG(NTGRD,NTGRD),STATEV(NSTATV),DTEMDX(NTGRD),TIME(2),
    &PRED(1),DPRED(1),PROPS(NPROPS),COORDS(3)
    PARAMETER (NELETOT=500)
    PARAMETER (NNODETOT=2736)
    COMMON /RRRR/ DGARRAY(NELETOT*27*9),
    DGARRAY1(NELETOT*27*9),
    &XYZGP(NELETOT*27*3),VECTORNORM(NELETOT*4*3),
    &SFSFI(20,20),SFSFI0(8,8)
    COMMON /NNNN/
    NUMNODE(NELETOT*4*1),ICALLUMATHT,KINCOLD,ICALLUMAT
    DIMENSION DG(3,3), DCDX0(3),CDMUDX0(3)
    DOUBLE PRECISION MOBILITY,J0(3)

CCCCCCCCCCCCCCCCCCCCCCCCCCCCCCCC
C DGP---DEFORMATION GRADIENT OF 20 GAUSSIAN POINTS IN THIS
ELEMENT
C XI---NATURAL COORDINATES OF THIS GAUSSIAN POINT
C DSFDXI---PARTIAL SF PARTIAL XI AT THIS GAUSSIAN POINTS
C DSFDX0---PARTIAL SF PARTIAL ORIGINAL COORDINATES AT THIS
GAUSSIAN POINTS
C DG---DEFORMATION GRADIENT TENSOR AT THIS GP
C DGI---INVERSE OF DG AT THIS GP

```

```

C FJAC---JACOBIAN AT THIS GP
C FJACI---INVERSE OF FJAC
C XNODE0---ORIGINAL COORDINATES OF THIS GP
C DGDG---DG TIMES DG AT THIS GP
C DCDX0---GRADIENT OF CONCENTRATION WITH RESPECT TO ORIGINAL
COORDINATES AT THIS GP
C CDMUDX0---CONCENTRATION TIMES GRADIENT OF CHEMICAL
POTENTIAL WITH RESPECT TO ORIGINAL COORDINATES AT THIS GP
C MOBILITY---MOBILITY TENSOR AT THIS GP
C J0---FLUX AT THIS GP IN ORIGINAL CONFIGURATION
CCCCCCCCCCCCCCCCCCCCCCCCCCCCCCCCCCCC
C      OPEN(10,FILE='D:\SIMULIA\TEMP\DEBUG.TXT',ACCESS='APPEND')
C      WRITE(10,*) 'RUN UMATHT', KSTEP, KINC, NOEL, NPT
C      CLOSE(10)
      ICALLUMATHT=ICALLUMATHT+1
      NOEL=NOEL-100000

      DG(1,1)=DGARRAY((NOEL-1)*243+(NPT-1)*9+1)
      DG(1,2)=DGARRAY((NOEL-1)*243+(NPT-1)*9+2)
      DG(1,3)=DGARRAY((NOEL-1)*243+(NPT-1)*9+3)
      DG(2,1)=DGARRAY((NOEL-1)*243+(NPT-1)*9+4)
      DG(2,2)=DGARRAY((NOEL-1)*243+(NPT-1)*9+5)
      DG(2,3)=DGARRAY((NOEL-1)*243+(NPT-1)*9+6)
      DG(3,1)=DGARRAY((NOEL-1)*243+(NPT-1)*9+7)
      DG(3,2)=DGARRAY((NOEL-1)*243+(NPT-1)*9+8)
      DG(3,3)=DGARRAY((NOEL-1)*243+(NPT-1)*9+9)

      DETDG=DG(1,1)*DG(2,2)*DG(3,3)-DG(1,1)*DG(2,3)*DG(3,2)
&      -DG(2,1)*DG(1,2)*DG(3,3)+DG(2,1)*DG(1,3)*DG(3,2)
&      +DG(3,1)*DG(1,2)*DG(2,3)-DG(3,1)*DG(2,2)*DG(1,3)

C !WE NEED TO SET THE VALUE OF ALPHA, BETA, A0, B0 ACCORDINGLY
HERE!
      C=TEMP
      MOBILITY=1
      DCDX0=0.D0
      DO I=1,3
          DCDX0(1)=DCDX0(1)+DG(I,1)*DTEMDCX(I)
          DCDX0(2)=DCDX0(2)+DG(I,2)*DTEMDCX(I)
          DCDX0(3)=DCDX0(3)+DG(I,3)*DTEMDCX(I)
      ENDDO
      IF(C.LE.0.99D0) THEN
          CDMUDC=1.D0/(1.D0-C)
      ENDIF
      IF(C.GT.0.99D0) THEN

```

```

CDMUDC=1.D2+1.D4*(C-0.99D0)
ENDIF
IF(KSTEP.EQ.2.AND.C.LT.0.D0) THEN
CDMUDC=1.D1
ENDIF
CDMUDX0(1)=CDMUDC*DCDX0(1)
CDMUDX0(2)=CDMUDC*DCDX0(2)
CDMUDX0(3)=CDMUDC*DCDX0(3)
J0(1)=-MOBILITY*CDMUDX0(1)
J0(2)=-MOBILITY*CDMUDX0(2)
J0(3)=-MOBILITY*CDMUDX0(3)

DUDT = 1.D0/DETDG
DUDG = 0.D0
DU = DUDT*DTEMP
U = U+DU

FLUX=0.D0
FLUX(1)=1.D0/DETDG*(DG(1,1)*J0(1)+DG(1,2)*J0(2)+DG(1,3)*J0(3))
FLUX(2)=1.D0/DETDG*(DG(2,1)*J0(1)+DG(2,2)*J0(2)+DG(2,3)*J0(3))
FLUX(3)=1.D0/DETDG*(DG(3,1)*J0(1)+DG(3,2)*J0(2)+DG(3,3)*J0(3))

DFDT=0.D0
IF(C.LE.0.99D0) THEN
DCDMUDCDC=1.D0/(1.D0-C)**2.D0
ENDIF
IF(C.GT.0.99D0) THEN
DCDMUDCDC=1.D4
ENDIF
DO I=1,3
    DFDT(1)=DFDT(1)-
DG(1,I)/DETDG*MOBILITY*DCDMUDCDC*DCDX0(I)
    DFDT(2)=DFDT(2)-DG(2,I)/DETDG*MOBILITY*DCDMUDCDC*DCDX0(I)
    DFDT(3)=DFDT(3)-DG(3,I)/DETDG*MOBILITY*DCDMUDCDC*DCDX0(I)
ENDDO

DFDG=0.D0
DO I=1,3
    DFDG(1,1)=DFDG(1,1)-
DG(1,I)*DG(1,I)/DETDG*MOBILITY*CDMUDC
    DFDG(1,2)=DFDG(1,2)-
DG(1,I)*DG(2,I)/DETDG*MOBILITY*CDMUDC
    DFDG(1,3)=DFDG(1,3)-
DG(1,I)*DG(3,I)/DETDG*MOBILITY*CDMUDC

```

```

      DFDG(2,1)=DFDG(2,1)-
      DG(2,I)*DG(1,I)/DETDG*MOBILITY*CDMUDC
      DFDG(2,2)=DFDG(2,2)-
      DG(2,I)*DG(2,I)/DETDG*MOBILITY*CDMUDC
      DFDG(2,3)=DFDG(2,3)-
      DG(2,I)*DG(3,I)/DETDG*MOBILITY*CDMUDC
      DFDG(3,1)=DFDG(3,1)-
      DG(3,I)*DG(1,I)/DETDG*MOBILITY*CDMUDC
      DFDG(3,2)=DFDG(3,2)-
      DG(3,I)*DG(2,I)/DETDG*MOBILITY*CDMUDC
      DFDG(3,3)=DFDG(3,3)-
      DG(3,I)*DG(3,I)/DETDG*MOBILITY*CDMUDC
      ENDDO
C      DFDG=0.D0

```

```

      NOEL=NOEL+100000

```

```

      RETURN
      END

```

```

*****

```

```

      SUBROUTINE
      UEXPAN(EXPAN,DEXPANDT,TEMP,TIME,DTIME,PRED,DPRED,
      $ STATEV,CMNAME,NSTATV,NOEL)
C
C THIS SUBROUTINE IS USED TO REALIZE THE EIGEN EXPANSION
      INCLUDE 'ABA_PARAM.INC'
C
      CHARACTER*80 CMNAME
C
      DIMENSION EXPAN(*),DEXPANDT(*),TEMP(2),TIME(2),PRED(*),
      $ DPRED(*),STATEV(NSTATV)
C
      BETA=2.82
      EXPAN(1)=0
      DEXPANDT(1)=0
      EXPAN(2)=0
      DEXPANDT(2)=0
      EXPAN(3)=(1+BETA*TEMP(1))/(1+BETA*(TEMP(1)-TEMP(2)))-1
      DEXPANDT(3)=-BETA**2*TEMP(2)/(1+BETA*(TEMP(1)-TEMP(2)))**2
C
      RETURN
      END

```

```

      SUBROUTINE
      DFLUX(FLUX,SOL,KSTEP,KINC,TIME,NOEL,NPT,COORDS,CLTYP,
      &TEMP,PRESS,SNAME)
      C
      C THIS SUBROUTINE IS USED TO REALIZE THE CONSTANT FLUX B.C.
      C
      INCLUDE 'ABA_PARAM.INC'
      C
      DIMENSION COORDS(3),FLUX(2),TIME(2)
      CHARACTER*80 SNAME
      PARAMETER (NELETOT=500)
      PARAMETER (NNODETOT=2736)
      COMMON /RRRR/
      DGARRAY(NELETOT*27*9),DGARRAY1(NELETOT*27*9),
      &XYZGP(NELETOT*27*3),VECTORNORM(NELETOT*4*3),
      &SFSFI(20,20),SFSFI0(8,8)
      COMMON /NNNN/
      NUMNODE(NELETOT*4*1),ICALLUMATHT,KINCOLD,ICALLUMAT
      DIMENSION VN(3),VNDGI(3),DGP(8,9),DG(3,3),DGI(3,3),XYZNODE(20*3)
      PARAMETER (POS=DSQRT(15.D0)/5.D0)

      CCCCCCCCCCCCCCCCCCCCCC
      C VN---NOMAL VECTOR AT THIS NODE
      C VNDGI---VN TIMES DGI AT THIS NODE
      C DGP---DEFORMATION GRADIENT AT 20 GAUSSIAN POINTS
      C DG---DEFORMATION GRADIENT TENSOR AT THIS NODE
      C DGI---INVERSE OF DG
      CCCCCCCCCCCCCCCCCCCCCC
      NOEL=NOEL-100000

      IF (KINC.EQ.0) THEN
        NE=NOEL
        DO NP=1,20
          XYZNODE((NP-1)*3+1)=
&          SFSFI(NP,1)*XYZGP((NE-1)*81+(1-1)*3+1)+
&          SFSFI(NP,2)*XYZGP((NE-1)*81+(2-1)*3+1)+
&          SFSFI(NP,3)*XYZGP((NE-1)*81+(3-1)*3+1)+
&          SFSFI(NP,4)*XYZGP((NE-1)*81+(4-1)*3+1)+
&          SFSFI(NP,5)*XYZGP((NE-1)*81+(6-1)*3+1)+
&          SFSFI(NP,6)*XYZGP((NE-1)*81+(7-1)*3+1)+
&          SFSFI(NP,7)*XYZGP((NE-1)*81+(8-1)*3+1)+
&          SFSFI(NP,8)*XYZGP((NE-1)*81+(9-1)*3+1)+
&          SFSFI(NP,9)*XYZGP((NE-1)*81+(10-1)*3+1)+

```

& SFSFI(NP,10)*XYZGP((NE-1)*81+(12-1)*3+1)+
 & SFSFI(NP,11)*XYZGP((NE-1)*81+(16-1)*3+1)+
 & SFSFI(NP,12)*XYZGP((NE-1)*81+(18-1)*3+1)+
 & SFSFI(NP,13)*XYZGP((NE-1)*81+(19-1)*3+1)+
 & SFSFI(NP,14)*XYZGP((NE-1)*81+(20-1)*3+1)+
 & SFSFI(NP,15)*XYZGP((NE-1)*81+(21-1)*3+1)+
 & SFSFI(NP,16)*XYZGP((NE-1)*81+(22-1)*3+1)+
 & SFSFI(NP,17)*XYZGP((NE-1)*81+(24-1)*3+1)+
 & SFSFI(NP,18)*XYZGP((NE-1)*81+(25-1)*3+1)+
 & SFSFI(NP,19)*XYZGP((NE-1)*81+(26-1)*3+1)+
 & SFSFI(NP,20)*XYZGP((NE-1)*81+(27-1)*3+1)

XYZNODE((NP-1)*3+2)=
 & SFSFI(NP,1)*XYZGP((NE-1)*81+(1-1)*3+2)+
 & SFSFI(NP,2)*XYZGP((NE-1)*81+(2-1)*3+2)+
 & SFSFI(NP,3)*XYZGP((NE-1)*81+(3-1)*3+2)+
 & SFSFI(NP,4)*XYZGP((NE-1)*81+(4-1)*3+2)+
 & SFSFI(NP,5)*XYZGP((NE-1)*81+(6-1)*3+2)+
 & SFSFI(NP,6)*XYZGP((NE-1)*81+(7-1)*3+2)+
 & SFSFI(NP,7)*XYZGP((NE-1)*81+(8-1)*3+2)+
 & SFSFI(NP,8)*XYZGP((NE-1)*81+(9-1)*3+2)+
 & SFSFI(NP,9)*XYZGP((NE-1)*81+(10-1)*3+2)+
 & SFSFI(NP,10)*XYZGP((NE-1)*81+(12-1)*3+2)+
 & SFSFI(NP,11)*XYZGP((NE-1)*81+(16-1)*3+2)+
 & SFSFI(NP,12)*XYZGP((NE-1)*81+(18-1)*3+2)+
 & SFSFI(NP,13)*XYZGP((NE-1)*81+(19-1)*3+2)+
 & SFSFI(NP,14)*XYZGP((NE-1)*81+(20-1)*3+2)+
 & SFSFI(NP,15)*XYZGP((NE-1)*81+(21-1)*3+2)+
 & SFSFI(NP,16)*XYZGP((NE-1)*81+(22-1)*3+2)+
 & SFSFI(NP,17)*XYZGP((NE-1)*81+(24-1)*3+2)+
 & SFSFI(NP,18)*XYZGP((NE-1)*81+(25-1)*3+2)+
 & SFSFI(NP,19)*XYZGP((NE-1)*81+(26-1)*3+2)+
 & SFSFI(NP,20)*XYZGP((NE-1)*81+(27-1)*3+2)

XYZNODE((NP-1)*3+3)=
 & SFSFI(NP,1)*XYZGP((NE-1)*81+(1-1)*3+3)+
 & SFSFI(NP,2)*XYZGP((NE-1)*81+(2-1)*3+3)+
 & SFSFI(NP,3)*XYZGP((NE-1)*81+(3-1)*3+3)+
 & SFSFI(NP,4)*XYZGP((NE-1)*81+(4-1)*3+3)+
 & SFSFI(NP,5)*XYZGP((NE-1)*81+(6-1)*3+3)+
 & SFSFI(NP,6)*XYZGP((NE-1)*81+(7-1)*3+3)+
 & SFSFI(NP,7)*XYZGP((NE-1)*81+(8-1)*3+3)+
 & SFSFI(NP,8)*XYZGP((NE-1)*81+(9-1)*3+3)+
 & SFSFI(NP,9)*XYZGP((NE-1)*81+(10-1)*3+3)+
 & SFSFI(NP,10)*XYZGP((NE-1)*81+(12-1)*3+3)+

```

&          SFSFI(NP,11)*XYZGP((NE-1)*81+(16-1)*3+3)+
&          SFSFI(NP,12)*XYZGP((NE-1)*81+(18-1)*3+3)+
&          SFSFI(NP,13)*XYZGP((NE-1)*81+(19-1)*3+3)+
&          SFSFI(NP,14)*XYZGP((NE-1)*81+(20-1)*3+3)+
&          SFSFI(NP,15)*XYZGP((NE-1)*81+(21-1)*3+3)+
&          SFSFI(NP,16)*XYZGP((NE-1)*81+(22-1)*3+3)+
&          SFSFI(NP,17)*XYZGP((NE-1)*81+(24-1)*3+3)+
&          SFSFI(NP,18)*XYZGP((NE-1)*81+(25-1)*3+3)+
&          SFSFI(NP,19)*XYZGP((NE-1)*81+(26-1)*3+3)+
&          SFSFI(NP,20)*XYZGP((NE-1)*81+(27-1)*3+3)

          DISTANCE=(COORDS(1)-XYZNODE((NP-1)*3+1))**2.D0
&          +(COORDS(2)-XYZNODE((NP-1)*3+2))**2.D0
&          +(COORDS(3)-XYZNODE((NP-1)*3+3))**2.D0
          IF (DISTANCE.LE.1.D-12) THEN
              NUMNODE((NOEL-1)*4+NPT)=NP
          ENDIF
      ENDDO
  ENDIF

  DGP=0.D0
  DO I=1,9
      DGP(1,I)=DGARRAY((NOEL-1)*243+(1-1)*9+I)
      DGP(2,I)=DGARRAY((NOEL-1)*243+(3-1)*9+I)
      DGP(3,I)=DGARRAY((NOEL-1)*243+(7-1)*9+I)
      DGP(4,I)=DGARRAY((NOEL-1)*243+(9-1)*9+I)
      DGP(5,I)=DGARRAY((NOEL-1)*243+(19-1)*9+I)
      DGP(6,I)=DGARRAY((NOEL-1)*243+(21-1)*9+I)
      DGP(7,I)=DGARRAY((NOEL-1)*243+(25-1)*9+I)
      DGP(8,I)=DGARRAY((NOEL-1)*243+(27-1)*9+I)
  ENDDO

  DG=0.D0
  NNODE=NUMNODE((NOEL-1)*4+NPT)
  DO I=1,8
      DG(1,1)=DG(1,1)+SFSFI0(NNODE,I)*DGP(I,1)
      DG(1,2)=DG(1,2)+SFSFI0(NNODE,I)*DGP(I,2)
      DG(1,3)=DG(1,3)+SFSFI0(NNODE,I)*DGP(I,3)
      DG(2,1)=DG(2,1)+SFSFI0(NNODE,I)*DGP(I,4)
      DG(2,2)=DG(2,2)+SFSFI0(NNODE,I)*DGP(I,5)
      DG(2,3)=DG(2,3)+SFSFI0(NNODE,I)*DGP(I,6)
      DG(3,1)=DG(3,1)+SFSFI0(NNODE,I)*DGP(I,7)
      DG(3,2)=DG(3,2)+SFSFI0(NNODE,I)*DGP(I,8)
      DG(3,3)=DG(3,3)+SFSFI0(NNODE,I)*DGP(I,9)
  ENDDO

```



```

DETGDG=DG(1,1)*DG(2,2)*DG(3,3)-DG(1,1)*DG(2,3)*DG(3,2)
& -DG(2,1)*DG(1,2)*DG(3,3)+DG(2,1)*DG(1,3)*DG(3,2)
& +DG(3,1)*DG(1,2)*DG(2,3)-DG(3,1)*DG(2,2)*DG(1,3)

DGI(1,1)=(DG(2,2)*DG(3,3)-DG(2,3)*DG(3,2))/DETGDG
DGI(1,2)=-(DG(1,2)*DG(3,3)-DG(1,3)*DG(3,2))/DETGDG
DGI(1,3)=-(DG(1,3)*DG(2,2)-DG(1,2)*DG(2,3))/DETGDG
DGI(2,1)=-(DG(2,1)*DG(3,3)-DG(2,3)*DG(3,1))/DETGDG
DGI(2,2)=(DG(1,1)*DG(3,3)-DG(1,3)*DG(3,1))/DETGDG
DGI(2,3)=-(DG(1,1)*DG(2,3)-DG(1,3)*DG(2,1))/DETGDG
DGI(3,1)=-(DG(2,2)*DG(3,1)-DG(2,1)*DG(3,2))/DETGDG
DGI(3,2)=-(DG(1,1)*DG(3,2)-DG(1,2)*DG(3,1))/DETGDG
DGI(3,3)=(DG(1,1)*DG(2,2)-DG(1,2)*DG(2,1))/DETGDG

VN(1)=VECTORNORM((NOEL-1)*12+(NPT-1)*3+1)
VN(2)=VECTORNORM((NOEL-1)*12+(NPT-1)*3+2)
VN(3)=VECTORNORM((NOEL-1)*12+(NPT-1)*3+3)

VNDGI(1)=VN(1)*DGI(1,1)+VN(2)*DGI(2,1)+VN(3)*DGI(3,1)
VNDGI(2)=VN(1)*DGI(1,2)+VN(2)*DGI(2,2)+VN(3)*DGI(3,2)
VNDGI(3)=VN(1)*DGI(1,3)+VN(2)*DGI(2,3)+VN(3)*DGI(3,3)

AREARATIO=DETGDG*DSQRT(VNDGI(1)**2.D0+VNDGI(2)**2.D0+VNDGI
(3)**2.D0)
C AREARATIO--- THE RATIO OF CURRENT SURFACE AREA TO ORIGINAL
AREA

C IF(KSTEP.EQ.1) FLUXNOMINAL=1.66666666666667
IF(KSTEP.EQ.1) FLUXNOMINAL=0.0185185185185

FLUX(1)=FLUXNOMINAL/AREARATIO
FLUX(2)=0.D0

NOEL=NOEL+100000

RETURN
END

```

```

*****

```

APPENDIX B

COPYRIGHT AND CO-AUTHOR APPROVAL

This dissertation includes some of my own published and publishable work. The detailed copyright permission is shown as below.

Chapter 2 is a published work reproduced with permission from Xu Wang, Sudhanshu S. Singh, Teng Ma, Cheng Lv, Nikhilesh Chawla, Hanqing Jiang.

"Quantifying Electrochemical Reactions and Properties of Amorphous Silicon in a Realistic Lithium-Ion Battery Configuration" *Chem. Mater.*, 2017, 29 (14), pp 5831–5840, DOI: 10.1021/acs.chemmater.7b00701, Publication Date (Web): June 30, 2017, Copyright © 2017 American Chemical Society Society.

Chapter 3 is publishable work reproduced with permission from Xu Wang, Wei Zeng, Liang Hong, Wenwen Xu, Haokai Yang, Fan Wang, Huigao Duan, Ming Tang, and Hanqing Jiang. "Stress-Driven Lithium Dendrite Growth Mechanism and Dendrite Mitigation by Electroplating on Soft Substrates". *Nature Energy* volume 3, pages227–235 (2018) DOI:10.1038/s41560-018-0104-5, Publication Date (Web): Mar 6, 2018, Copyright © 2018 Macmillan Publishers Limited, part of Springer Nature.

I verify that the following co-authors have approved the usage of our publication materials in the dissertation: Sudhanshu S. Singh (Indian Institute of Technology Kanpur), Teng Ma (Arizona State University), Cheng Lv (Arizona State University), Nikhilesh Chawla (Arizona State University), Hanqing Jiang (Arizona State University), Wei Zeng (Hunan University), Liang Hong (Rice University), Wenwen Xu (Arizona State University), Haokai Yang (Arizona State University), Fan Wang (Rice University), Huigao Duan (Hunan University) and Ming Tang (Rice University).